Interplay between optical vortices and condensed matter

Guillermo F. Quinteiro Rosen*

IMIT-CONICET and Departamento de Física, FACENA, Universidad Nacional del Nordeste, 3400 Ciudad de Corrientes, Argentina

Pablo I. Tamborenea

Departamento de Física and IFIBA, FCEN, Universidad de Buenos Aires, Ciudad Universitaria, Pabellón I, 1428 Ciudad de Buenos Aires, Argentina

Tilmann Kuhn

Institut für Festkörpertheorie, Westfälische Wilhelms-Universität Münster, Wilhelm-Klemm-Straße 10, 48149 Münster, Germany

(published 25 August 2022)

Interest in the multiple facets of optical vortices has flourished in the last three decades. This review examines the basic research and applications of the interplay between optical vortices and condensed-matter systems. This subfield of optical-vortex physics has rapidly developed in recent years thanks to a vigorous synergy between theory and experiment. After presenting self-contained and focused introductions to optical vortices and condensed-matter optics, theory and current progress in the research on the interaction of condensed-matter systems and optical vortices are examined. When one considers the interaction of optical vortices with condensed-matter systems, many aspects of the standard theory of the interaction of matter with plane-wave light need to be reformulated. In bulk, light-matter Hamiltonian matrix elements have to be recalculated and novel selection rules are obtained, reflecting the conservation of total angular momentum. Orbital angular momentum is transferred from the light beam to the photoexcited electrons, thereby generating macroscopic currents. Semiconductor nanostructures add the complexity of their own spatial inhomogeneity, which is handled adequately by the envelope-function approximation. Here again modified matrix elements for light-matter interactions dictate the allowed and forbidden optical transitions, which are distinct from those obtained in traditional optical excitation with smooth fields. Quantum rings play a central role due to their specially adapted geometry to the cylindrical nature of the optical-vortex beams. When the electron-electron interaction is taken into account, the rich physics of excitons and exciton polaritons comes into play and is modified by the finite orbital angular momentum of the structured light. Furthermore, the new features brought about by optical vortices in plasmonics and in the optical excitation of two-dimensional materials are reviewed. For all these systems theory and recent experiments are discussed. Finally, an overview of current and prospective applications of the interaction of optical vortices with condensed-matter systems in the fields of quantum technologies, communications, sensing, etc., is presented. Throughout this review an attempt has been made to present not only a survey of the relevant literature but also a perspective on the interesting and rapidly evolving field of optical-vortex–condensed-matter interactions.

DOI: 10.1103/RevModPhys.94.035003

CONTENTS

*gfquinteiro@exa.unne.edu.ar

I. INTRODUCTION

From early times we have sought to understand the interplay between light and matter (Cajori, 1899; Weiner and Nunes, 2017). Clear evidence points to serious attempts to learn about reflection, refraction, and vision before the scientific revolution (16th and 17th centuries), a notable example being the work by Ibn al-Haytham in the early 11th century, who is considered by some to be the father of optics. Brilliant discoveries, most of which are familiar to us, took place around the 17th century and helped to shape the revolution. The law of refraction was enunciated in 1621 by Snellius. Newton (1672) used refraction by a prism to show the decomposition of white light into colors. Light projecting out of the direct line of sight beyond objects was first described by Grimaldi, who named the phenomenon diffraction. Huygens (1690) contributed the picture of secondary waves in wave fronts, which together with Young's interference investigations around 1800 set the basis for Fresnel's work that explained diffraction and wrapped up optical phenomena under a coherent wave interpretation of light. Among several corroborations of Fresnel's theory, the prediction by Hamilton (1831) of conical refraction in anisotropic biaxial crystals, experimentally verified soon thereafter using aragonite mineral (Lloyd, 1833), stands out as a most notable one. On the one hand, it is an early example of a theoretical prediction guiding successful experiments and, on the other hand, it is the earliest known report of a phenomenon involving optical vortices, as we see in Sec. II.A. In parallel, the study of electricity and magnetism matured to the point at which Maxwell (1865) unified these phenomena with those of light. Progress in pure optics continued, as attested by the (here most relevant) work of Abbe (1874), who established the resolution limit of optical systems; see Sec. VI. Though diffraction, refraction, and reflection are indeed the result of the interaction of light with objects, our modern splitting of physics sets them under the umbrella of optics.

However, only a few years later it turned out that the nature of light as an electromagnetic wave was not the entire truth. Phenomena like the blackbody radiation or the photoelectric effect could not be explained at this level. To overcome this difficulty, Planck (1900) postulated the quantization of energy and Einstein (1905) introduced the concept of light quanta, now generally called photons. A quantum theory of electrodynamics was formulated by Dirac (1927), and in the 1950s and early 1960s seminal papers by Mandel (1958), Sudarshan (1963), and Glauber (1963) created the field of quantum optics. A milestone with enormous impact in the field of optics was the invention of the laser by Maiman (1960), which, along with its many applications in everyday life, is now the light source for the vast majority of optical experiments.

From a current perspective, the study of light-matter interactions relies strongly on advances in chemistry, quantum mechanics, atomic physics, and solid-state physics. Back to our timeline, modern chemistry (as opposed to alchemy) developed in parallel to optics, from work by researchers such as Boyle (1661), Lavoisier (De Morveau *et al.*, 1787; Lavoisier, 1793), Dalton (1808), and Mendeleev (1869), who gave modern form to the notions of gases, atoms, and chemical elements.

Milestones in atomic physics that provided greater insight on light-matter interactions are well known to us, and we recall only a few that are the most connected to the following sections: in 1900, before quantum mechanics, Drude proposed a model of free-electron motion in metals subjected to electric and magnetic fields using the Lorentz force in a Newtonian mechanics framework (Drude, 1900); later the model was extended to bound electrons by Lorentz himself. The Drude-Lorentz model has been amply used to explain plasmon polaritons, which is the subject of Sec. IV.C. A more sophisticated and modern way to deal with light-matter interactions in classical terms is by employing Lagrangian mechanics together with the Lorentz force. This leads to a generalized potential in the Lagrangian that depends on the scalar and vector potentials (and the velocity of the particle). By shifting to Hamiltonian mechanics, one defines the well-known minimal-coupling Hamiltonian. This can be quantized for charged particles and/or fields. Historically, other crucial developments have been the reformulation in terms of the dipole approximation in the case of atoms by Göppert-Mayer (1931) and the generalization in terms of the multipolar expansion by Power and Zienau (1959) and Woolley (1971) to describe the interaction of light with nonrelativistic particles, which delineate the work regarding problems related to gauge; see Sec. III.C.1.

Condensed-matter physics is currently a collage of various subject matter. Originally, topics in condensed matter came from its predecessor, solid-state physics, which dealt with metals, semiconductors, and their applications. As told by Martin (2019), "Even in the early days of solid-state physics, the name was maligned because the field's topics and techniques were often equally relevant to liquids, molecules, plasmas, and other nonsolids…. Critical phenomena such as phase transitions, nonlinear dynamics of fluid systems, and liquid helium research that had little or nothing to do with

solids took center stage." Condensed-matter physics now encompasses the study of a variety of quantum states such as exciton polaritons, two-dimensional electron gas, spin lattices, superconductors, Bose-Einstein condensates, etc., most of which are supported in solid-state media and some of which are also in other condensed phases.

The seminal paper by Bloch (1929) constitutes an early milestone in the formulation of a quantum theory of crystalline solids. According to what is now called *Bloch's theorem*, the wave function of an electron in a crystal satisfying the time-independent Schrödinger equation can be written as a plane wave with a lattice-periodic modulation. The corresponding energies $\epsilon_{n\mathbf{k}}$ can be classified by the wave vector $\mathbf{k}$ restricted to the first Brillouin zone and an additional integer number n. They form the band structure in $\mathbf{k}$ space, with n labeling the bands. Combining this band structure with the Fermi statistics of electrons, one could distinguish between metals, on the one hand, and semiconductors and insulators, on the other hand. The wave vector of the electron provides a natural interface for the coupling to light, which is typically also expressed in terms of plane waves. In semiconductors and insulators the coupling to light leads to the excitation of electrons from an occupied band to an empty one or, in the often convenient electron-hole picture, to the creation of electron-hole pairs. However, it was soon realized that the Coulomb interaction between the electrons may qualitatively change this picture. Instead of a continuous absorption spectrum in the region close to the band gap, discrete absorption lines appeared. The electron and hole form a new quasiparticle, the *exciton*, which was introduced by Frenkel (1931) in the limit of strongly bound electron-hole pairs and by Wannier (1937) for weakly bound pairs, the latter realized in typical semiconductor materials. In metals the Coulomb interaction leads to new quasiparticles called *plasmons*, which were introduced by Bohm and Pines (1953). In the following years many other types of quasiparticles have been introduced, such as *polarons*, *polaritons*, *magnons*, and *Cooper pairs* (Haken, 1976; Kittel, 1987).

We have built up much of our theoretical knowledge in optics from the concept of plane waves. Plane waves are a perfect building block to represent more complex light beams through Fourier analysis; however, they are often not well suited to describing strongly inhomogeneous waves, which in terms of plane waves correspond to a superposition involving an extremely large number of wave vectors. Optical vortices (OVs) are an example of such strongly space-varying light fields (Allen, Padgett, and Babiker, 1999; Allen, Barnett, and Padgett, 2003; Padgett, Courtial, and Allen, 2004; Torres and Torner, 2011; Andrews and Babiker, 2012), as we see in Sec. II.

Since the 1990s a variety of experimental techniques have revealed new effects caused by OVs acting on matter (atoms, molecules, and nanoparticles), which exceed our expectations based on their interaction with plane waves. The most prominent ones come from the fact that OVs may carry orbital angular momentum (OAM) (Allen *et al.*, 1992). More recently researchers have started to predict and measure effects coming from the interaction of OVs with condensed-matter systems, and possible applications to quantum technology and materials science have been proposed.

This review outlines the physics of the interaction of OVs and condensed-matter systems, providing both a cohesive formulation of the theoretical basis and a comprehensive review of current progress in the field. We start with a description of fundamental elements of the theory of OVs (Sec. II) and the theory of condensed-matter systems (Sec. III), which are necessary to the development in Sec. IV of the theory of the interaction of condensed matter and OVs. Section IV also reviews the progress achieved in several subfields, namely, in semiconductor and conductor bulk and nanostructure physics, exciton-polariton physics, and plasmonics, and in the physics of two-dimensional materials. Progress toward applications, which is discussed in Sec. V, has also been significant. Finally, after concluding remarks we present our view on possible future directions for the research of OV–condensed-matter interactions in Sec. VI.

II. OPTICAL VORTICES

Vortices are part of our daily lives. Some are evident, like whirlpools, tornadoes, and hurricanes, through the quiet eye of the storm; see Fig. 1. Other vortices pass unnoticed, such as amphidromic points of tidal waves in the ocean, where the height of the water remains the same, while it changes in their surroundings (Whewell, 1836), or sound waves scattered out of rough surfaces, whose wave fronts exhibit "dislocations" similar to those found in crystals, in which the intensity becomes zero (Nye and Berry, 1974). What do all these phenomena have in common? A vector field such as the wind velocity has null intensity at the vortex center and revolves around it.

When it comes to optics, however, many may be reluctant to accept that vortices happen naturally. After all, as young students we were first taught that light is a bundle of rays following broken paths of straight trajectories, only later to be told that light is an undulatory phenomenon representable by plane waves. After such insistent teachings, it is no surprise that many extrapolate ideas and ended up believing that light around us consists of waves with little spatial structure, although we know about the principle of superposition. But as happens with whirls in wind and water, optical vortices are indeed ubiquitous phenomena in nature. They appear as a

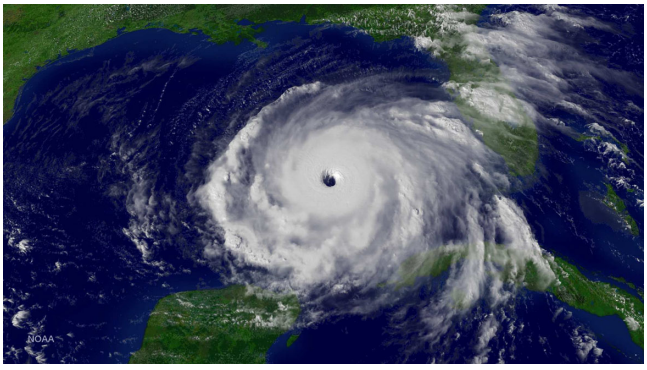

FIG. 1. Satellite photograph of Hurricane Katrina on August 28, 2005, with a clear view of its eye. From National Oceanic and Atmospheric Administration National Environmental Satellite, Data, and Information Service.

result of light scattering on rough surfaces (speckles) (Baranova *et al.*, 1981) and even from the simple superposition of a few plane waves (Masajada and Dubik, 2001; O'Holleran, Padgett, and Dennis, 2006). Optical vortices are worth studying to free ourselves from previous prejudices, to expand our understanding of electrodynamics, and for the possible advances that they can introduce in current technologies.

A. History

A light phenomenon with vortex character was first considered by Hamilton (1831) in his work on conical refraction, and soon thereafter was experimentally verified by Lloyd (1833). In conical refraction a Gaussian light beam entering a biaxial crystal along the optical axis is refracted inside it into a cone, emerging as a cylinder (Berry, 2004; Born and Wolf, 2013; Turpin *et al.*, 2016). The outgoing cylindrical beam is a superposition of simpler fields, some of which have vortex features. In fact, conical refraction is now used for the generation of OVs from Gaussian beams (Berry, Jeffrey, and Mansuripur, 2005; Phelan *et al.*, 2009). Hamilton's prediction and its experimental corroboration by Lloyd were at the time a major achievement; however, it is curious that it was only much later that conical refraction was recognized as a manifestation of vortical optics.

In modern research, examples of OVs appeared in a handful of publications around 1950 (Dennis, O'Holleran, and Padgett, 2009). Nevertheless, the first systematic study was carried out by Nye and Berry (1974) on what they called dislocations in sound (and applicable to general) waves scattered from rough surfaces. For the scattered wave, they found that screw dislocations can be expressed as an extra complex phase in the field; as we see in Sec. II.B, this is the signature of an optical vortex. The concept of OV was formulated by Coullet, Gil, and Rocca (1989); see also Shen *et al.* (2019).

A few years later Allen *et al.* (1992) published what is the most influential article in the field. They showed that a Laguerre-Gaussian (LG) beam of light (a particular OV) carries a well-defined amount of OAM, as opposed to the spin or intrinsic angular momentum (SAM) associated with the polarization. Research in OVs accelerated and in a few years many physics branches and other sciences picked up the idea and applied it to their respective fields.

The concept of quantized vortices in condensed phases has a long history. They have been studied in different systems, such as superfluids (Feynman, 1955), type-II superconductors (Abrikosov, 1957), and Bose-Einstein condensates (Matthews *et al.*, 1999). The spontaneous formation of optical vortices has been observed in semiconductor microcavities forming a surface-emitting vertical cavity laser (Scheuer and Orenstein, 1999) or hosting an exciton-polariton condensate (Lagoudakis *et al.*, 2008). The investigation of phenomena associated with the excitation of a semiconductor by an OV started about a decade ago. Two independent works provided theoretical predictions (Quinteiro and Tamborenea, 2009c) and experimental results (Ueno *et al.*, 2009).

Optical vortices are famous for their OAM, which at first sight is a surprising feature. However, Beth (1936) demonstrated that circularly polarized light carries angular momentum (AM) in units of $\hbar$, which can be transferred to matter. In a quantum theory of light this AM corresponds to the spin of the photon. Moreover, nuclear physics tells about multipole transitions in spontaneous emission: One starts with the classical electrodynamics theory in terms of a single-frequency electric-current source and derives the average energy flux (Poynting vector) of the radiation. Next one quantizes the electric current to a linear-momentum operator (gradient) and restates the classical single-frequency oscillating state to a transition between the initial and final quantum states. All along the calculation there is a phase factor $\exp(i\mathbf{k}\cdot\mathbf{r})$ that, upon expansion and truncation ($kr \ll 1$), yields the well-known electric dipole radiation $\exp(i\mathbf{k}\cdot\mathbf{r}) \simeq 1$, electric quadrupole radiation $i\mathbf{k}\cdot\mathbf{r}$, etc., as well as the magnetic 2^n poles (Fermi, 1950; Schiff, 1955; Basdevant and Rich, 2005). Photons from the 2^n-pole radiation carry angular momentum equal to $n\hbar$ or are superpositions of states with this angular momentum. Finally, quoting Fermi (1950), "[I]t may frequently be necessary to go several terms down the expansion before finding a nonzero term. The reason is that more than half of all conceivable radiation processes are forbidden because of conservation of angular momentum or because of parity considerations."

B. Basic theory

Light fields can be represented using different basis functions. Simplicity usually dictates the choice of one or another. Thus, for light coming from a distant source such as a star, the most appropriate representation is by plane waves. If instead we analyze the field close to a point source, we would likely decide in favor of spherical waves. In the case of a cylindrical geometry, Bessel beams provide a basis exhibiting a complete factorization in cylindrical coordinates that, however, decay rather slowly in the radial direction. Collimated laser beams are often better described by Gaussian beam profiles. To obtain a basis the Gaussian profile has to be supplemented by a set of transverse mode functions. Depending on the geometry, suitable bases are Hermite-Gaussian functions (in Cartesian coordinates) or Laguerre-Gaussian functions (in cylindrical coordinates).

Optical vortices, also referred to as "twisted light" and "light carrying OAM," are electromagnetic fields[1] with single or multiple points or lines in which the phase[2] cannot be defined, and therefore the amplitude vanishes. Figure 2 shows exemplary electric-field profiles in planes perpendicular to the propagation direction (z direction) at different z positions at a fixed time or at different times at a given z position. The Poynting vector swirls around these so-called singularitites,[3] much like the wind does around the eye of a tropical hurricane; see Fig. 1. The electric and magnetic fields may also circulate the singularity,[4] but then in general they alternate

[1]The phenomenon happens in the entire spectrum; thus, a more appropriate name would possibly be "electromagnetic vortex" or "twisted electromagnetic field."

[2]Singularities can also exist in the polarization.

[3]Note that the term singularity does not refer here to mathematical infinities.

[4]If not otherwise stated, singularity refers here to a phase singularity.

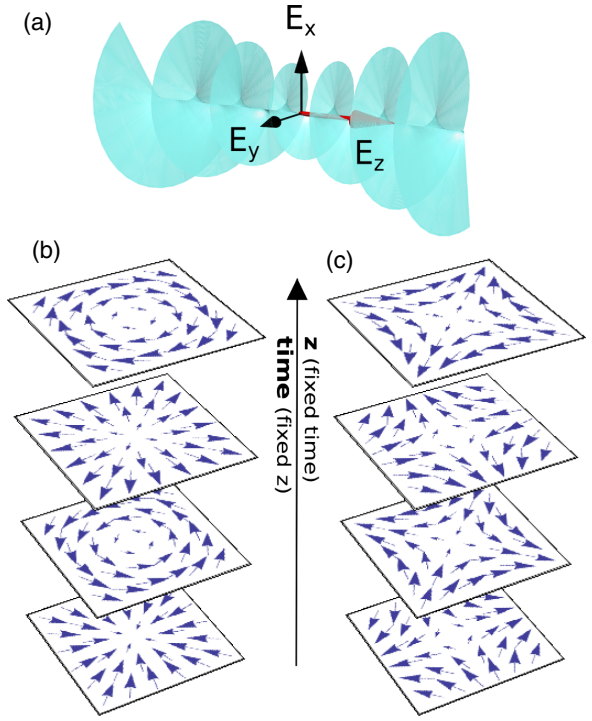

FIG. 2. Optical vortex, a highly inhomogeneous light field. (a) Helical or skrewlike wave front for a circularly polarized OV with topological charge $\ell = 1$ propagating along z. Electric-field components are shown, and the atypically strong longitudinal component is indicated in red. Lower panel: snapshot succession in time or z coordinate of electric-field maps (E_x and E_y) normal to the propagation direction for (b) antiparallel-AM and (c) parallel-AM beams. Antiparallel-AM fields cycle in time or z through sink, center, and source to finally reverse sense; what flows in a definite direction around the vortex is in fact the energy (Poynting vector) (Dennis, O'Holleran, and Padgett, 2009). On the other hand, parallel-AM fields remain saddle critical points.

in time the sense of rotation, as seen in Fig. 2. The singularity may exist in one or several components of the field and is mathematically represented by a phase $\exp(i\ell\varphi)$ in cylindrical coordinates $\{r, \varphi, z\}$, with $r = 0$ denoting the position of the singularity and the integer ℓ the so-called topological charge. If not otherwise stated, in the following we consider beams propagating in the z direction.

An OV is a curious object with features quite unlike plane waves, as seen in Fig. 2. We first concentrate on the transverse components of the field, i.e., the components of $\mathbf{E}$ and $\mathbf{B}$ lying in the x-y plane. Beams with a phase dependence $\sim\exp(i\ell\varphi)$ in these components carry well-defined OAM in the propagation direction related to the spatial (orbital) structure of the beam through the topological charge ℓ. Furthermore, they may carry intrinsic AM related to the handedness of circular polarization characterized by the parameter $\sigma = \pm 1$ referring to the polarization vector $\mathbf{e}_\sigma = (\hat{\mathbf{x}} + i\sigma\hat{\mathbf{y}})/\sqrt{2}$, with $\hat{\mathbf{x}}$ and $\hat{\mathbf{y}}$ denoting Cartesian unit vectors.

OVs are in fact a large family of fields, all exhibiting singularities, that can be classified according to different criteria. They naturally split into two topologically distinct classes, according to whether the orbital and intrinsic AMs are parallel or antiparallel to each other, i.e., when $\mathrm{sgn}(\sigma) = \mathrm{sgn}(\ell)$ or $\mathrm{sgn}(\sigma) \neq \mathrm{sgn}(\ell)$, respectively. In terms of critical points, the electric or magnetic vector field of antiparallel beams at fixed z cycles in time (or along z for fixed time) through sink, source, and center have a winding number 1, while the vector field of parallel beams remains a saddle point with a winding number -1, as seen in Figs. 2(b) and 2(c), respectively. Out of these two classes, OVs of the antiparallel set differ the most from plane waves, for they may exhibit a magnetic field that dominates over the electric field and strong longitudinal field components (Sec. II.C.2).

Another surprising feature is that an OV has a field component along the propagation direction z. The truth is that all real propagating beams (with finite lateral size) possess such a component; otherwise, Maxwell's equation $\boldsymbol{\nabla}\cdot\mathbf{E} = 0$ could not be satisfied; see Chap. 3 of Novotny and Hecht (2006). But in OVs the longitudinal component can be significant, with an intensity overcoming that of the transverse component. Moreover, an $E_z(\mathbf{r})/B_z(\mathbf{r})$ component is required if the light beam has OAM in z, as can easily be deduced from the double vector product in the following formula for the angular momentum $\mathbf{L}$ of the electromagnetic fields (Cohen-Tannoudji, Dupont-Roc, and Grynberg, 1989; Jackson, 1999):

$$\mathbf{L} = \frac{1}{\mu_0 c^2}\int \mathbf{r}\times[\mathbf{E}(\mathbf{r},t)\times\mathbf{B}(\mathbf{r},t)]d\mathbf{r}, \tag{1}$$

using Système International units, with μ_0 denoting the vacuum permeability and c representing the vacuum speed of light. After the work of Allen *et al.* (1992), OVs received another distinctive name, twisted light, which makes reference to the skrewlike form of the OV wave front. Note that this surface of a constant phase helps us to visualize the unusual space dependence of the Poynting vector $\mathbf{S} = \mathbf{E}\times\mathbf{H}$, which seems to twist around the propagation axis. However, do not relate the circulation of the transverse components of the antiparallel field to the OAM associated with the beam, since this circulation reverses sense for evolving time or z progression, as seen in Fig. 2(b). An alternative formulation for the angular momenta of fields is possible if the Poynting vector in Eq. (1) is replaced by the canonical momentum; this change unveils interesting phenomena related to the transverse component of the OAM and SAM, as described by Bliokh and Nori (2015).

To formalize the previously mentioned ideas and arrive at full expressions for the OV fields, we consider in cylindrical (Sec. II.C) and other non-Cartesian coordinate systems (Sec. II.D) Maxwell's equations, their potentials, or the corresponding wave equations in free space.

For electromagnetic fields in vacuum the wave equation is easily derived from Maxwell's equations. Take the curl of Faraday's law ($\boldsymbol{\nabla}\times\mathbf{E} = -\partial_t\mathbf{B}$), use Ampère's law ($\boldsymbol{\nabla}\times\mathbf{B} = \mu_0\epsilon_0\partial_t\mathbf{E}$) to eliminate the magnetic field $\mathbf{B}$, and simplify the expression using the absence of sources ($\boldsymbol{\nabla}\cdot\mathbf{E} = 0$ and $\boldsymbol{\nabla}\cdot\mathbf{B} = 0$) together with the identity $\boldsymbol{\nabla}\times(\boldsymbol{\nabla}\times\mathbf{E}) = \boldsymbol{\nabla}(\boldsymbol{\nabla}\cdot\mathbf{E}) - \boldsymbol{\nabla}^2\mathbf{E}$. This leads to

$$\boldsymbol{\nabla}^2\mathbf{E}(\mathbf{r},t) - \frac{1}{c^2}\frac{\partial^2}{\partial t^2}\mathbf{E}(\mathbf{r},t) = 0, \tag{2}$$

with $c^2 = (\mu_0\epsilon_0)^{-1}$, ϵ_0 the vacuum permittivity, and the same equation for the magnetic field $\mathbf{B}$. Because the equations are linear (and thus the superposition of fields is possible), one can look for harmonic solutions proportional to $\exp(-i\omega t)$; alternatively, one can assume the separability of the space and time dependence of the electric field and split Eq. (2). We then arrive at the Helmholtz equation

$$\nabla^2\mathbf{E}(\mathbf{r},t) + k^2\mathbf{E}(\mathbf{r},t) = 0, \tag{3}$$

with $k = \omega/c$ the absolute value of the wave vector. Like all partial differential equations, the Helmholtz equation has a variety of different solutions, reflecting different geometries and boundary conditions.

We first concentrate on exact solutions of the Helmholtz equation. We are interested in light fields propagating in the z direction. Propagation-invariant fields (also called nondiffracting beams) are then characterized using an electric field of the form

$$\mathbf{E}(\mathbf{r},t) = \tilde{\mathbf{E}}(\mathbf{r}_\perp)e^{i(q_z z-\omega t)} + \text{c.c.}, \tag{4}$$

with $\mathbf{r}_\perp$ a position vector orthogonal to the propagation direction, c.c. denoting the complex conjugate, and $\tilde{\mathbf{E}}(\mathbf{r}_\perp)$ satisfying a two-dimensional Helmholtz equation

$$\nabla_\perp^2\tilde{\mathbf{E}}(\mathbf{r}_\perp) + (k^2 - q_z^2)\tilde{\mathbf{E}}(\mathbf{r}_\perp) = 0, \tag{5}$$

where $\nabla_\perp^2$ is the transverse Laplacian operator. It is known that this equation can be further separated in four different types of coordinates: Cartesian, polar, parabolic, and elliptic ones, leading to plane waves, Bessel beams, Weber beams, and Mathieu beams, respectively. We later discuss, in particular, polar coordinates (Bessel and LG beams) in more detail and also comment on elliptical coordinates (Mathieu beams) in Sec. II.D.

In addition to the Helmholtz equation, the electric field has to satisfy the Maxwell equation $\nabla\cdot\mathbf{E} = 0$. As a consequence, the transverse components $\tilde{\mathbf{E}}_\perp(\mathbf{r}_\perp)$ can be independently chosen among the solutions of the Helmholtz equation. The longitudinal component is then determined as

$$\tilde{E}_z(\mathbf{r}_\perp) = \frac{i}{q_z}\nabla_\perp\cdot\tilde{\mathbf{E}}_\perp(\mathbf{r}_\perp), \tag{6}$$

which again shows that a space dependence of the transverse components in general is associated with a longitudinal component.

Propagation-invariant beams have the advantage of being exact solutions of the Helmholtz equation. However, they have the practical drawback of exhibiting only a weak (as in the case of Bessel beams) or even no (as in the case of plane waves) lateral decay. Therefore, they are not normalized and carry infinite energy. Consequently, they can only be approximations to real light beams. Any light beam created in an experiment has a finite lateral extent. Most prominent examples are Gaussian beams, which, however, are not propagation invariant but experience diffraction. From Fraunhofer diffraction theory for a slit with width w_0, it is known that the width w of the central maximum (i.e., the distance between the first diffraction minima) in the far field grows with distance z according to $w/w_0 = 2\lambda z/w_0^2 = 4\pi z/kw_0^2$, with $\lambda = 2\pi/k$ the wavelength. Thus, there is a characteristic length, the diffraction length $l = kw_0^2$ (Lax, Louisell, and McKnight, 1975) or the Rayleigh range $z_R = (1/2)l$ (Loudon, 2003), which describes the length scale on which a Gaussian beam with minimal radius w_0, called the beam waist, widens. The beam is therefore characterized by three different length scales, the wavelength λ, the beam waist w_0, and the diffraction length l. If a beam satisfies the condition $w_0 \ll l$, it is weakly divergent or, in other words, it consists only of plane-wave components with wave vectors close to the beam axis. Such beams are called paraxial beams. Note that, according to the definition of the diffraction length, the condition $w_0 \ll l$ also implies $\lambda \ll w_0$. To quantify the divergence of the beam, a paraxial parameter f can be defined according to

$$f = \frac{w_0}{l} = \frac{1}{w_0 k}. \tag{7}$$

Following Lax, Louisell, and McKnight (1975), one can use this parameter as an expansion parameter for beams not deviating too much from the paraxial limit. The electric field is then written as

$$\mathbf{E}(\mathbf{r},t) = \tilde{\mathbf{E}}(\mathbf{r})e^{i(kz-\omega t)} + \text{c.c.} \tag{8}$$

Note the difference compared to the ansatz in Eq. (4) referring to nondiffracting beams. Here $\tilde{\mathbf{E}}(\mathbf{r})$ depends on all three coordinates and the propagation term has the full wave vector $k = \omega/c$. Using the fact that in the transverse direction $\tilde{\mathbf{E}}(\mathbf{r})$ varies on a length scale w_0, while in the longitudinal direction the respective length scale is l, the field can be expanded in a power series in f. Separating the field envelope into transverse ($\tilde{\mathbf{E}}_\perp$) and longitudinal ($\tilde{E}_z\hat{\mathbf{z}}$) parts, it can be shown that the transverse (longitudinal) components of the field come only in even (odd) powers of f (Lax, Louisell, and McKnight, 1975). The zeroth-order term then corresponds to the extreme paraxial approximation of a completely transverse beam satisfying the paraxial wave equation

$$\nabla_\perp^2\tilde{\mathbf{E}}_\perp(\mathbf{r}) + 2ik\partial_z\tilde{\mathbf{E}}_\perp(\mathbf{r}) = 0. \tag{9}$$

Typical solutions of the paraxial wave equation are Hermite-Gaussian beams, which factorize in Cartesian coordinates (x,y), and Laguerre-Gaussian beams, which factorize in cylindrical coordinates (r,φ). We later return, in particular, to Laguerre-Gaussian modes.

The longitudinal component at first order of the paraxial parameter is again obtained from the divergence equation for the electric field, leading to

$$\tilde{E}_z(\mathbf{r}) = if w_0\nabla_\perp\cdot\tilde{\mathbf{E}}_\perp(\mathbf{r}). \tag{10}$$

For the construction of higher-order terms, see Lax, Louisell, and McKnight (1975).

In electrodynamics and optics it is often convenient to introduce potentials because in this way the homogeneous

Maxwell equations are automatically fulfilled. Electromagnetic potentials *per se* are ambiguous due to gauge invariance (Jackson, 1999): a particular pair of electric field $\mathbf{E}$ and magnetic field $\mathbf{B}$ relates to a family of pairs of vector potential $\mathbf{A}$ and scalar potential Φ through

$$\mathbf{E}(\mathbf{r},t) = -\partial_t \mathbf{A}(\mathbf{r},t) - \boldsymbol{\nabla}\Phi(\mathbf{r},t), \tag{11a}$$

$$\mathbf{B}(\mathbf{r},t) = \boldsymbol{\nabla} \times \mathbf{A}(\mathbf{r},t). \tag{11b}$$

In addition to the standard scalar and vector potentials Hertz vector potentials can also be used (Wang *et al.*, 2016), but they are less common and we do not discuss them further in the review. Members of the family of potentials differ from each other by scalar functions χ and, starting with an initial pair $(\mathbf{A}^{(1)}, \Phi^{(1)})$, another pair $(\mathbf{A}^{(2)}, \Phi^{(2)})$ within the family is obtained using the gauge transformation

$$\mathbf{A}^{(2)}(\mathbf{r},t) = \mathbf{A}^{(1)}(\mathbf{r},t) + \boldsymbol{\nabla}\chi(\mathbf{r},t), \tag{12a}$$

$$\Phi^{(2)}(\mathbf{r},t) = \Phi^{(1)}(\mathbf{r},t) - \partial_t \chi(\mathbf{r},t) \tag{12b}$$

(the superscripts are omitted when the gauge is understood). To work with potentials, one chooses a suitable gauge. The two most commonly used ones, both of which fix the divergence of the vector potential,[5] are the Coulomb gauge

$$\boldsymbol{\nabla} \cdot \mathbf{A}(\mathbf{r},t) = 0 \tag{13}$$

and the Lorenz gauge

$$\boldsymbol{\nabla} \cdot \mathbf{A}(\mathbf{r},t) + \frac{1}{c^2}\frac{\partial \Phi(\mathbf{r},t)}{\partial t} = 0. \tag{14}$$

Far from sources, i.e., in the regime mostly studied here, in the Coulomb gauge the scalar potential vanishes; the gauge is then also called the radiation gauge. This is usually the starting point for the quantization of electromagnetic fields in quantum optics. In both gauges the potentials are still not completely determined by the gauge conditions; see Chap. 6 of Jackson (1999). In the Coulomb gauge any time-independent gauge field $\chi(\mathbf{r})$ satisfying the Laplace equation $\boldsymbol{\nabla}^2\chi(\mathbf{r}) = 0$ again leads to potentials satisfying the Coulomb gauge. In the Lorenz gauge any gauge function $\chi(\mathbf{r},t)$ satisfying the homogeneous wave equation $(\boldsymbol{\nabla}^2 - c^{-2}\partial_{tt})\chi(\mathbf{r},t) = 0$ leads again to potentials satisfying the Lorenz gauge. In particular, choosing a gauge function according to $\partial_t\chi(\mathbf{r},t) = \Phi^{(1)}(\mathbf{r},t)$ also leads in the Lorenz gauge to potentials satisfying $\Phi^{(2)} = 0$ and $\boldsymbol{\nabla} \cdot \mathbf{A}^{(2)} = 0$, which agrees with the Coulomb gauge condition. On the other hand, choosing a gauge function with $\partial_z\chi(\mathbf{r},t) = -A_z^{(1)}(\mathbf{r},t)$ results in potentials with a vanishing longitudinal component of the vector potential, i.e., $A_z^{(2)} = 0$.

The vector potential in the Coulomb and Lorenz gauges and the scalar potential in the Lorenz gauge satisfy in free space the same homogeneous wave equation (2) as the electric and magnetic fields. Therefore, everything that was previously stated about the electric field concerning exact and propagation-invariant solutions, as well as comments regarding the paraxial approximation, also remains valid for the potentials. In particular, for monochromatic potentials with time dependence $\sim\exp(-i\omega t)$ in the zeroth order of the paraxial approximation, the transverse components of the vector potential, in both Coulomb and Lorenz gauges, satisfy the paraxial wave equation

$$\boldsymbol{\nabla}_\perp^2 \tilde{\mathbf{A}}_\perp(\mathbf{r}) + 2ik\partial_z \tilde{\mathbf{A}}_\perp(\mathbf{r}) = 0. \tag{15}$$

The longitudinal component A_z (in the case of $\Phi = 0$) and the scalar potential Φ (in the case of $A_z = 0$) are of first order in the paraxial parameter and satisfy

$$\tilde{A}_z(\mathbf{r}) = ifw_0 \boldsymbol{\nabla}_\perp \cdot \tilde{\mathbf{A}}_\perp(\mathbf{r}) \quad \text{if } \Phi = 0, \tag{16a}$$

$$\tilde{\Phi}(\mathbf{r}) = -ifcw_0 \boldsymbol{\nabla}_\perp \cdot \tilde{\mathbf{A}}_\perp(\mathbf{r}) \quad \text{if } A_z = 0. \tag{16b}$$

Owing to gauge invariance, there is no unique way to derive OVs through the vector potential. When looking through the literature, in paraxial optics one is more likely to find derivations in terms of the Lorenz gauge with vanishing A_z (Allen *et al.*, 1992; Dávila Romero, Andrews, and Babiker, 2002; Loudon, 2003), while in nonparaxial optics it is more common to find work using the Coulomb gauge with $\Phi = 0$ (Volke-Sepulveda *et al.*, 2002; Jáuregui, 2004; Matula *et al.*, 2013).

Typically, the derivation starts with a guess about the form of the transverse component $\mathbf{A}_\perp$ of the vector potential. The remaining components (Φ in the case of $A_z = 0$ and A_z in the case of $\Phi = 0$) are then fixed either using the exact gauge condition (in nonparaxial optics) or using Eq. (16) when working in the paraxial approximation. A generalization scheme inspired by the two aforementioned procedures was developed by Quinteiro *et al.* (2019), and we discuss it further in Sec. II.C.2 to derive general Bessel beams; a discussion on Laguerre-Gaussian beams was given by Quinteiro *et al.* (2019). Once scalar and vector potentials are obtained, electric and magnetic fields result from Eqs. (11a) and (11b).

Thus far we have treated the electromagnetic field as a classical quantity. A quantum point of view is indeed necessary in specific problems with OV–condensed-matter interactions, such as in polariton physics (Sec. IV.B) or if the photon statistics comes into play. Quantization of the fields is usually performed in the Coulomb gauge. Without going into detail at this point of our discussion, it is worth recalling some correspondence between the viewpoint of light waves and photons that helps one navigate through the literature. A circularly polarized field with handedness $\sigma = \pm 1$ is formed out of photons with definite helicity $\sigma = \pm 1$ and SAM $\hbar\sigma$ (sometimes called intrinsic AM). And a paraxial classical OV with topological charge ℓ is formed out of photons with OAM $\hbar\ell$, a fact that was verified in a number of experiments (Courtial *et al.*, 1997; Arnaut and Barbosa, 2000; Mair *et al.*, 2001) and is of most relevance in studies on single-photon OV-matter interactions (Sec. IV).

Finally, OVs are not restricted to the visible region of the electromagnetic spectrum, and interesting research and

[5]The curl of the vector potential is already fixed by definition (11).

applications have been done in other spectral regions; see Secs. II.H and V.C.

C. Single-singularity fields

The family of OVs embraces all sorts of fields with single and multiple phase singularities. Single-singularity fields have been by far the most studied ones, and they also are the easiest to analyze. In the following we describe the two most important cases in cylindrical coordinates: (i) Laguerre-Gaussian beams as solutions of the paraxial wave equation and (ii) Bessel beams as solutions of the full wave equation, but also solutions of the paraxial wave equation. Because of its relevance in past and current research in general and singular optics, we start with case (i), even though it describes an approximate situation.

1. Laguerre-Gaussian beams

Beams with finite lateral extension are obtained as solutions of the paraxial wave equation. In the lowest, i.e., zeroth, order of the paraxial parameter f, electric and magnetic fields as well as the vector potential are purely transverse and they are described by the paraxial wave equation (9) or (15). Introducing a scalar mode function $u(\mathbf{r})$, we can write

$$\mathbf{A}(\mathbf{r},t)=\mathbf{A}_0u(\mathbf{r})e^{i(kz-\omega t)}+\text{c.c.} \tag{17}$$

with a two-dimensional constant vector $\mathbf{A}_0$. The important case of a well-defined intrinsic (or spin) AM is realized for circularly polarized beams with $\mathbf{A}_0=A_0\mathbf{e}_\sigma$. The electric and magnetic fields have the same structure, only with $\mathbf{A}_0$ replaced by $\mathbf{E}_0=i\omega\mathbf{A}_0$ and $\mathbf{B}_0=ik\hat{\mathbf{z}}\times\mathbf{A}_0$ [note that the terms resulting from $\partial_z u(\mathbf{r})$ are of higher order in the paraxial parameter]. The mode function satisfies the paraxial wave equation. A factorization in Cartesian coordinates (x,y) leads to the Hermite-Gaussian modes, while the factorization in polar coordinates (r,φ) leads to the following Laguerre-Gaussian modes (Barnett, Babiker, and Padgett, 2017):

$$u(\mathbf{r})=\sqrt{\frac{2p!}{\pi(p+|\ell|)!}}\frac{1}{w(z)}\left(\frac{r\sqrt{2}}{w(z)}\right)^{|\ell|}e^{i\ell\varphi}e^{i\psi(z)}\times L_p^{|\ell|}\left(\frac{2r^2}{w^2(z)}\right)\exp\left[-\frac{r^2}{w^2(z)}\right]\exp\left[-ik\frac{r^2}{2R(z)}\right], \tag{18}$$

where $w(z)=w_0\sqrt{1+(z/z_R)^2}$ is the beam radius, $R(z)=z[1+(z_R/z)^2]$ is the radius of curvature of the wave front, $\psi(z)=-(|\ell|+2p+1)\arctan(z/z_R)$ is the Gouy phase, and $L_p^{|\ell|}$ is a generalized Laguerre polynomial. The parameters w_0 and $z_R=(1/2)kw_0^2$ are the previously mentioned beam waist and the Rayleigh range, respectively. This expression for the mode function shows that LG beams are fields with a single singularity located at $r=0$ and with topological charge ℓ.

In the lowest order of the paraxial approximation, the fields are completely transverse. This is nevertheless inconsistent with real beams with finite width, whose rays travel (at least slightly) at an angle. When a beam diverges or converges, a longitudinal component of the field necessarily exists. This component is restored in the first-order correction to the paraxial beam according to Eqs. (16a) and (16b). Using the Lorenz gauge with $A_z=0$ (Loudon, 2003), one obtains a scalar potential according to

$$\Phi(\mathbf{r},t)=-ifcw_0e^{i(kz-\omega t)}\mathbf{A}_0\cdot\boldsymbol{\nabla}_\perp u(\mathbf{r}), \tag{19}$$

leading to a longitudinal component of the electric field

$$\begin{aligned}E_z(\mathbf{r},t)&=-\partial_z\Phi(\mathbf{r},t)\\&=-ce^{i(kz-\omega t)}\mathbf{A}_0\cdot\boldsymbol{\nabla}_\perp u(\mathbf{r}),\end{aligned} \tag{20}$$

where we use $f=(w_0k)^{-1}$; see Eq. (7).

A calculation based on the angular momentum density (Cohen-Tannoudji, Dupont-Roc, and Grynberg, 1989; Jackson, 1999) of the field $u_0(r,z)e^{i\ell\varphi}$ reveals that the ratio of AM in the z direction to the energy is $J_z/W=\ell/\omega+\sigma/\omega$. The separation between spin and orbital AM and what it suggests about the quantization of the OAM (take the energy W as that of a photon $\hbar\omega$) are delicate matters; see Sec. 2 of Allen, Padgett, and Babiker (1999).

2. Bessel beams

The Helmholtz equation (3) written in cylindrical coordinates is separable. The equations in the angle φ and longitudinal z coordinates are simply solvable using complex exponential functions; the equation for the radial r coordinate is Bessel's differential equation (Arfken and Weber, 2005), for which the solutions and their properties have been extensively studied (Korenev, 2002). Bessel beams (Durnin, Miceli, and Eberly, 1987) have their own benefits. They (i) retain their spatial profile on propagation and are therefore also called nondiffracting beams, (ii) describe nonparaxial fields and are therefore valid for any values of the beam parameters, (iii) are mathematically simpler than LG beams, and (iv) have the simplest modal decomposition (Sec. II.F). However, as happens with plane waves, they are not realizable in the real world, since they decay slowly in the radial direction and therefore carry infinite energy.

We now derive Bessel beams using a scheme mentioned in Sec. II.B that uses potentials (Quinteiro *et al.*, 2019). We now look for the solution of the Helmholtz equation for the transverse component of the vector potential. If one assumes a monochromatic field and circular polarization of the transverse part, the solution reads

$$\mathbf{A}_\perp(\mathbf{r},t)=A_0J_\ell(q_rr)e^{i\ell\varphi}e^{i(q_zz-\omega t)}\mathbf{e}_\sigma+\text{c.c.}, \tag{21}$$

in which $J_\ell(q_rr)$ is a Bessel function of the first kind of order ℓ, with the latter denoting the topological charge, $q_r=\sqrt{k^2-q_z^2}$, with the inverse q_r^{-1} related to the beam waist, and where $\mathbf{e}_\sigma$ is the circular polarization vector. As previously discussed, this transverse part has to be complemented by a longitudinal component and/or a scalar potential to satisfy the gauge condition. Using the Lorenz condition, we get

$$\boldsymbol{\nabla}_\perp\cdot\mathbf{A}_\perp(\mathbf{r},t)+\partial_zA_z(\mathbf{r},t)+\frac{1}{c^2}\partial_t\Phi(\mathbf{r},t)=0. \tag{22}$$

While in the previous discussions we have taken either A_z or Φ to be zero, a more general choice is

$$\partial_z A_z^{(\gamma)}(\mathbf{r},t) = -\gamma \boldsymbol{\nabla}_\perp \cdot \mathbf{A}_\perp(\mathbf{r},t), \tag{23a}$$

$$\Phi^{(\gamma)}(\mathbf{r},t) = -i(1-\gamma)\frac{c^2}{\omega}\boldsymbol{\nabla}_\perp \cdot \mathbf{A}_\perp(\mathbf{r},t), \tag{23b}$$

with a real parameter $0 \le \gamma \le 1$. $\gamma = 1$ and $\gamma = 0$ restore the aforementioned limiting cases of only A_z or only Φ. $\boldsymbol{\nabla}_\perp \cdot \mathbf{A}_\perp$ is determined using Eq. (21). Finally, using Eqs. (11a) and (11b) as well as the separation of the propagating part according to Eq. (4), the electromagnetic fields are obtained as

$$\tilde{\mathbf{E}}^{(\gamma)}(\mathbf{r}) = iE_0\left\{J_\ell(q_r r)e^{i\ell\varphi}\mathbf{e}_\sigma - \frac{1-\gamma}{2}\left(\frac{q_r}{k}\right)^2[J_\ell(q_r r)e^{i\ell\varphi}\mathbf{e}_\sigma - J_{\ell+2\sigma}(q_r r)e^{i(\ell+2\sigma)\varphi}\mathbf{e}_{-\sigma}] - i\sigma\frac{q_r(q_z^2+\gamma q_r^2)}{\sqrt{2}q_z k^2}J_{\ell+\sigma}(q_r r)e^{i(\ell+\sigma)\varphi}\hat{\mathbf{z}}\right\}, \tag{24a}$$

$$\tilde{\mathbf{B}}^{(\gamma)}(\mathbf{r}) = \sigma B_0\left\{J_\ell(q_r r)e^{i\ell\varphi}\mathbf{e}_\sigma + \frac{\gamma}{2}\left(\frac{q_r}{q_z}\right)^2[J_\ell(q_r r)e^{i\ell\varphi}\mathbf{e}_\sigma + J_{\ell+2\sigma}(q_r r)e^{i(\ell+2\sigma)\varphi}\mathbf{e}_{-\sigma}] - i\sigma\frac{q_r}{\sqrt{2}q_z}J_{\ell+\sigma}(q_r r)e^{i(\ell+\sigma)\varphi}\hat{\mathbf{z}}\right\}, \tag{24b}$$

with $E_0 = \omega A_0$ and $B_0 = q_z A_0$. This is actually a family of beams. Some interesting choices are (i) $\gamma = 1$: Close to $r = 0$ for $q_r/q_z \simeq 1$ (i.e., in the strongly nonparaxial regime), the magnetic field may surpass the electric field (Sec. IV.A), while the transverse part of the electric field has a well-defined circular polarization. (ii) $\gamma = 0$: Now the electric field dominates close to the beam center, while the transverse part of the magnetic field has a well-defined circular polarization. (iii) $\gamma = \gamma_s = (1 + k/q_z)^{-1}$: The ratio between the magnitudes of the electric and magnetic fields resembles that of plane waves (Li, 2009; Bliokh *et al.*, 2010). Another family of beams related to Eqs. (24a) and (24b) can be easily obtained from duality, i.e., the replacements $E \to -cB$ and $B \to E/c$ (Anderson and Arthurs, 1990; Mignaco, 2001).

Note that the potentials of Eq. (23) for different values of γ are not related by a gauge transformation, as indicated by the fact that the electric and magnetic fields depend on γ. For each value of γ, gauge functions χ can be found that remove either Φ or A_z. This gauge transformation will then modify the transverse components $\mathbf{A}_\perp$ of the vector potential [Eq. (21)] in such a way that they also contain contributions of opposite circular polarization $\sim\mathbf{e}_{-\sigma}$ with different topological charges.

The fields of Eqs. (24a) and (24b) display a single singularity at $r = 0$ but have varying topological charges for different parts and components. Several interesting features of such fields, like the mixing of orbital and spin AM or the appearance of longitudinal components, are discussed in Sec. IV when needed; see Quinteiro, Reiter, and Kuhn (2015, 2017b) and Quinteiro *et al.* (2019) and references therein for more details.

D. Multiple-singularity fields

Simple solutions to the paraxial or full wave equation are LG and Bessel beams that present a single singularity at the beam axis located at $r = 0$. More complex fields can be built using the superposition principle: for example, adding two LG beams whose optical axes are parallel but displaced by a distance such that there is essentially no overlap would result in a two-singularity field. However, a different approach based on the fact that, as previously mentioned, the wave equation is also separable in coordinates other than Cartesian and cylindrical ones can be applied. In particular, the solution of the wave equation, of both the exact and the paraxial one, in elliptical coordinates (ξ, η, z) leads to yet another class of elementary beams, among which there are beams that exhibit multiple phase singularities (Mathieu, 1868; Gutiérrez-Vega, Iturbe-Castillo, and Chávez-Cerda, 2000; Gutiérrez-Vega *et al.*, 2001; Alpmann *et al.*, 2010; Hernández-Hernández *et al.*, 2010; Pabon *et al.*, 2017; Shen *et al.*, 2019).

Elliptical and Cartesian coordinates are related using the transformation $x = h\cosh(\xi)\cos(\eta)$, $y = h\sinh(\xi)\sin(\eta)$, with $0 \le \xi < \infty$, and $0 \le \eta < 2\pi$, with the curves of constant ξ ellipses. Owing to the separability of the Helmholtz equation (5), solutions are given in the form of products of radial and angular parts, i.e., $\tilde{\mathbf{E}}(\xi,\eta) = \mathbf{E}_0 R(\xi)\Theta(\eta)$, with R and Θ satisfying Mathieu differential equations

$$\frac{d^2R(\xi)}{d\xi^2} - [a - 2b\cosh(2\xi)]R(\xi) = 0, \tag{25a}$$

$$\frac{d^2\Theta(\eta)}{d\eta^2} + [a - 2b\cos(2\eta)]\Theta(\eta) = 0. \tag{25b}$$

In Eqs. 25(a) and (25b), a is the separation constant and b is proportional to the ellipticity. These solutions are called Mathieu beams. They present a greater variety of situations, from solutions with single singularities to solutions with multiple singularities. Figure 3 compares a LG beam (single singularity) with a particular Mathieu beam with two singularities on the horizontal axis.

E. Paraxial versus nonparaxial beams

Propagation-invariant beams like plane waves, Bessel beams, or Mathieu beams are solutions to both the exact

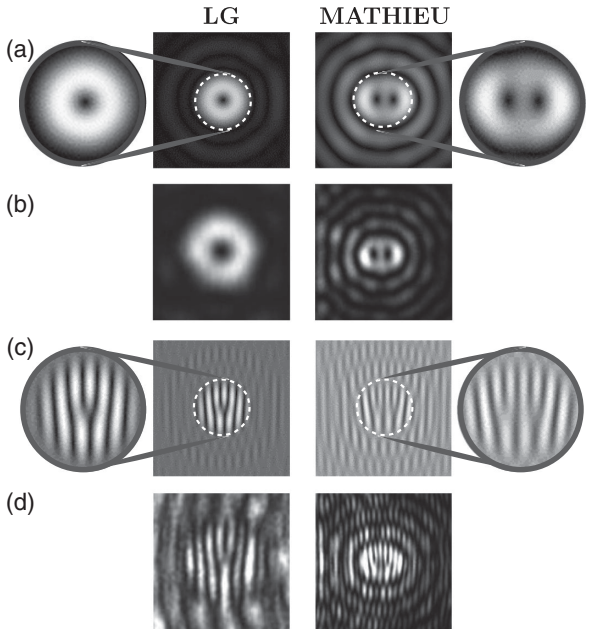

FIG. 3. LG and Mathieu beams. (a),(c) Numerical simulations of (left image) LG and (right image) Mathieu beams. (a) Single beam intensity and (c) interference pattern with a reference Gaussian beam. (b),(d) Experimental results corresponding to single beam intensity and interference with a Gaussian beam, respectively. The single beam images show a single (LG) or double (Mathieu) zero-intensity point, while the interference images present the characteristic single (LG) or double (Mathieu) forklike pattern. The first and fourth columns are enlargements of (a) and (c). Adapted from Pabon *et al.*, 2017.

and the paraxial wave equation. In contrast, LG beams as an example of beams with a finite width have been obtained only from the paraxial wave equation. In this section we take a closer look at the relation between beams described by the full Helmholtz equation and the paraxial wave equation. We consider a generic transverse component of the electromagnetic field or the vector potential with a harmonic time dependence according to $\psi(\mathbf{r})\exp(-i\omega t)$, where $\psi(\mathbf{r})$ describes the spatial profile of the wave.

Normalized transverse eigenmodes $v_n(\mathbf{r}_\perp)$ of both the Helmholtz and the paraxial wave equation are given by solutions of the eigenvalue equation

$$-\boldsymbol{\nabla}_\perp^2 v_n(\mathbf{r}_\perp) = q_n^2 v_n(\mathbf{r}_\perp) \tag{26}$$

with eigenvalues q_n^2, where q_n corresponds to a characteristic transverse wave vector of the mode n. Depending on the symmetry, the eigenfunctions can be plane waves in the transverse directions, Bessel functions times $\exp(i\ell\varphi)$, products of Mathieu functions, or other functions that do not factorize in the two transverse coordinates. Propagation-invariant beams are characterized using a single transverse eigenmode (or a superposition of degenerate eigenmodes), which explains why they are solutions to both the Helmholtz and the paraxial wave equation. The Bessel beam of Eq. (21), for example, is a solution with $q_n = q_r$.

The transverse modes have to be complemented by longitudinal modes. Here the difference between the two types of wave equations comes into play. Since the paraxial wave equation is of first order in z, there is one longitudinal mode $\sim\exp(iq_z z)$ for a given transverse mode. In contrast, the Helmholtz equation is of second order in z, leading to two modes $\sim\exp(\pm iq_z z)$.

Because of the orthogonality and completeness of the mode functions, any solution can be expanded into a sum of these modes. For waves satisfying the paraxial wave equation, this leads to

$$\psi(\mathbf{r}_\perp, z) = \sum_n C_n v_n(\mathbf{r}_\perp) e^{i(k - q_n^2/2k)z}. \tag{27}$$

[Note that when Eq. (27) is inserted into the paraxial wave equation the factor $\exp(ikz)$ has to be omitted.] The expansion coefficients C_n are obtained in the standard way from the profile at a given z, e.g., $z = 0$, according to

$$C_n = \int v_n^*(\mathbf{r}_\perp)\psi(\mathbf{r}_\perp, 0)d\mathbf{r}_\perp. \tag{28}$$

This analysis demonstrates that if the transverse profile at $z = 0$ is given by a transverse eigenmode, the shape remains fixed and the beam is nondiffracting. On the other hand, we can introduce a propagator $G(\mathbf{r}_\perp, z; \mathbf{r}'_\perp, z')$ according to

$$\psi(\mathbf{r}_\perp, z) = \int G(\mathbf{r}_\perp, z; \mathbf{r}'_\perp, z')\psi(\mathbf{r}'_\perp, z')d\mathbf{r}'_\perp, \tag{29}$$

with

$$\begin{aligned} G(\mathbf{r}_\perp, z; \mathbf{r}'_\perp, z') &= \sum_n v_n^*(\mathbf{r}'_\perp) v_n(\mathbf{r}_\perp) e^{i(k - q_n^2/2k)(z - z')} \\ &= \frac{k}{2\pi i(z - z')} e^{ik[(z - z') + |\mathbf{r}_\perp - \mathbf{r}'_\perp|^2/2(z - z')]}, \end{aligned} \tag{30}$$

where Eq. (30) is most easily obtained using plane waves as transverse eigenmodes. Replacing the longitudinal coordinate z with time, this is exactly the propagator for the time-dependent Schrödinger equation for a free particle, which reflects the equivalence of the paraxial wave equation with the time-dependent Schrödinger equation. The widening of a Gaussian beam along z is thus completely equivalent to the broadening of a Gaussian wave packet with increasing time in quantum mechanics.

We now turn to the full Helmholtz equation. Here the expansion of a wave in the eigenmodes reads

$$\psi(\mathbf{r}_\perp, z) = \sum_n v_n(\mathbf{r}_\perp)\left[A_n e^{i\sqrt{k^2 - q_n^2}\, z} + B_n e^{-i\sqrt{k^2 - q_n^2}\, z}\right].$$

It is now no longer sufficient to know the wave at a given longitudinal position z; instead, its derivative with respect to z is also needed. The expansion coefficients are obtained from

$$A_n = \frac{1}{2}\int v_n^*(\mathbf{r}_\perp)\left[\psi(\mathbf{r}_\perp, 0) + \frac{\partial_z\psi(\mathbf{r}_\perp, 0)}{i\sqrt{k^2 - q_n^2}}\right]d\mathbf{r}_\perp, \tag{31a}$$

$$B_n = \frac{1}{2}\int v_n^*(\mathbf{r}_\perp)\left[\psi(\mathbf{r}_\perp,0) - \frac{\partial_z\psi(\mathbf{r}_\perp,0)}{i\sqrt{k^2-q_n^2}}\right]d\mathbf{r}_\perp. \tag{31b}$$

The decomposition with these coefficients is valid for arbitrary beam profiles $\psi(\mathbf{r}_\perp,0)$ and $\partial_z\psi(\mathbf{r}_\perp,0)$ at a fixed longitudinal position, here taken to be $z=0$. In particular, we find that as soon as there is more than one transverse mode contributing, the beam necessarily also has a counterpropagating ($\sim B_n$) part. We can now ask when this profile corresponds to a paraxial beam. First, the z dependence of a paraxial beam is dominated by e^{ikz}, leading to $\partial_z\psi(\mathbf{r}_\perp,0) \approx ik\psi(\mathbf{r}_\perp,0)$. Second, the transverse wave vector is much smaller than the longitudinal one, i.e., $q_n \ll k$ for all modes appearing in the expansion. Under these conditions $B_n \ll A_n$ and $A_n \approx C_n$; i.e., the counterpropagating part becomes negligible and the coefficient of the term propagating in the positive z direction is essentially the same as in the case of the paraxial wave equation. Furthermore, if we expand in the exponent $\sqrt{k^2-q_n^2} \approx k - q_n^2/2k$, we recover the solution, and thus also the propagator, of the paraxial wave equation.

We summarize our understanding of paraxial and nonparaxial solutions. A simplified picture relying solely on the paraxial wave equation leads us to interpret paraxiality as a binary property: either a field satisfies the equation or not; in addition, the paraxial solution is disconnected from the exact solution to the Helmholtz equation. Lax, Louisell, and McKnight (1975) have already shown that paraxiality is instead a feature that comes in degrees. In this section, we have further demonstrated that simple approximations on a nonparaxial solution smoothly reduce it to a paraxial solution, thus completing the link between the two fields.

F. Representing optical vortices by plane waves

Bessel and Laguerre-Gaussian functions each form sets of solutions that can be used to define more complicated fields through superpositions. This is also the case for plane waves, which are routinely used as a basis set to build up other functions using Fourier analysis. For problems involving simple OVs with approximately cylindrical symmetry, such as single-singularity beams generated in the lab, a mathematical representation is easiest in terms of Bessel, LG, or other cylindrical basis functions. However, there are important situations in which a decomposition of the OV into a plane-wave basis becomes necessary, such as in the study of reflection and refraction. Fresnel coefficients relate the amplitudes of incident, reflected, and refracted plane waves, and thus are unsuitable for direct use with OVs. Furthermore, this decomposition provides additional insight into the properties of OVs. The representation in terms of plane waves is referred to as a modal decomposition or an angular spectrum representation (Siegman, 1990; Novotny and Hecht, 2006; Kaiser *et al.*, 2009; Schmidt *et al.*, 2011). Such a decomposition is possible for all relevant fields, $\mathbf{E}$, $\mathbf{B}$, $\mathbf{A}$, and Φ; here we concentrate on the decomposition of the $\mathbf{E}$ field.

The starting point is the general representation of the spatial part of a vector field as its plane-wave (or spatial Fourier) components

$$\mathbf{E}(\mathbf{r}) = \int \mathcal{E}(\mathbf{q})\mathbf{e}_{\mathbf{q}\sigma}e^{i\mathbf{q}\cdot\mathbf{r}}d\mathbf{q}, \tag{32}$$

where $\mathcal{E}(\mathbf{q})$ denotes the Fourier component of the field and $\mathbf{e}_{\mathbf{q}\sigma}$ represents its polarization vector. Since we consider only monochromatic waves, all plane waves must have the same frequency. Therefore, the absolute value of $\mathbf{q}$ is fixed to $q = k = \omega/c$. Using spherical coordinates (q,θ_q,φ_q), only the integrals over the angles θ_q and φ_q remain.

To be specific, we now concentrate in the following on propagation-invariant beams traveling in the z direction. These beams have a well-defined longitudinal wave vector q_z and thus, since $\cos\theta_q = q_z/k$, a well-defined θ_q, such that only the integral over φ_q remains. Fixing θ_q also fixes the perpendicular wave vector $q_r = k\sin\theta_q$. Using the cylindrical coordinates (q_r,φ_q,q_z) and (r,φ,z), we have

$$\begin{aligned}\mathbf{q}\cdot\mathbf{r} &= q_r r(\cos\varphi_q\cos\varphi + \sin\varphi_q\sin\varphi) + q_z z\\ &= q_r r\cos(\varphi_q-\varphi) + q_z z,\end{aligned} \tag{33}$$

leading to the decomposition of a propagation-invariant beam according to

$$\mathbf{E}(\mathbf{r}) = e^{iq_z z}\int_0^{2\pi}\tilde{\mathcal{E}}(\varphi_q)\mathbf{e}_{\mathbf{q}\sigma}e^{iq_r r\cos(\varphi_q-\varphi)}d\varphi_q. \tag{34}$$

The beam therefore represents a superposition of plane waves with wave vectors $\mathbf{q}$ lying on the surface of a cone around the propagation direction $\hat{\mathbf{z}}$. To specify the beam, we have to fix the angle dependence $\tilde{\mathcal{E}}(\varphi_q)$ and the polarization vectors $\mathbf{e}_{\mathbf{q}\sigma}$ of the plane-wave components.

As an example, we decompose the electric field of Eq. (24a) into plane waves. The electric field has the general form

$$\begin{aligned}\mathbf{E}^{(\gamma)}(\mathbf{r}) = iE_0 e^{iq_z z}[&c_\sigma^{(\gamma)}J_\ell(q_r r)e^{i\ell\varphi}\mathbf{e}_\sigma\\ &+ c_{-\sigma}^{(\gamma)}J_{\ell+2\sigma}(q_r r)e^{i(\ell+2\sigma)\varphi}\mathbf{e}_{-\sigma}\\ &- i\sigma c_z^{(\gamma)}J_{\ell+\sigma}(q_r r)e^{i(\ell+\sigma)\varphi}\hat{\mathbf{z}}],\end{aligned} \tag{35}$$

with coefficients $c_\sigma^{(\gamma)}$, $c_{-\sigma}^{(\gamma)}$, and $c_z^{(\gamma)}$, as can be deduced from Eq. (24a). Using the Jacobi-Anger identity or the corresponding integral representations of the Bessel functions (see also their multiple uses in Sec. IV),

$$J_m(q_r r) = \frac{1}{2\pi i^m}\int_0^{2\pi} e^{iq_r r\cos\eta}e^{-im\eta}d\eta, \tag{36}$$

with $\eta = \varphi_q - \varphi$, we can identify the integrand in Eq. (34) as

$$\begin{aligned}\tilde{\mathcal{E}}(\varphi_q)\mathbf{e}_{\mathbf{q}\sigma} = \frac{iE_0}{2\pi i^\ell}e^{i(\ell+\sigma)\varphi_q}[&c_\sigma^{(\gamma)}e^{-i\sigma\varphi_q}\mathbf{e}_\sigma\\ &+ i^{-2\sigma}c_{-\sigma}^{(\gamma)}e^{i\sigma\varphi_q}\mathbf{e}_{-\sigma} - i\sigma i^{-\sigma}c_z^{(\gamma)}\hat{\mathbf{z}}].\end{aligned} \tag{37}$$

Using the identities $i^{-2\sigma} = -1$ and $i^{-\sigma} = -i\sigma$, we thus obtain the angle-dependent weight

$$\tilde{\mathcal{E}}(\varphi_q) = (-1)^{\ell} i^{\ell+1} \frac{\sqrt{N} E_0}{2\pi} e^{i(\ell+\sigma)\varphi_q} \tag{38}$$

and the polarization vector

$$\begin{aligned}\mathbf{e}_{\mathbf{q}\sigma} &= \frac{1}{\sqrt{N}} [c_{\sigma}^{(\gamma)} e^{-i\sigma\varphi_q} \mathbf{e}_{\sigma} - c_{-\sigma}^{(\gamma)} e^{i\sigma\varphi_q} \mathbf{e}_{-\sigma} - c_z^{(\gamma)} \hat{\mathbf{z}}] \\ &= \frac{1}{\sqrt{N}} \left\{ \left[1 - \frac{1-\gamma}{2} \left(\frac{q_r}{k} \right)^2 \right] e^{-i\sigma\varphi_q} \mathbf{e}_{\sigma} \right. \\ &\quad \left. - \frac{1-\gamma}{2} \left(\frac{q_r}{k} \right)^2 e^{i\sigma\varphi_q} \mathbf{e}_{-\sigma} - \frac{q_r (q_z^2 + \gamma q_r^2)}{\sqrt{2} q_z k^2} \hat{\mathbf{z}} \right\}, \end{aligned} \tag{39}$$

with N a normalization constant for the polarization vector. In the latter form the explicit expressions for the coefficients from Eq. (24a) have been inserted. According to Eq. (38), plane waves with different angles in the x-y plane indeed contribute with a weight given by a phase factor $\exp(im\varphi_q)$, as might be expected for an OV. The polarization vector $\mathbf{e}_{\mathbf{q}\sigma}$ of Eq. (39) of the plane-wave component traveling in the direction $\mathbf{q}$ becomes more transparent when expressed in terms of unit vectors in spherical coordinates (q, θ_q, φ_q), which are given by

$$\begin{aligned}\mathbf{e}_q &= \hat{\mathbf{x}} \sin\theta_q \cos\varphi_q + \hat{\mathbf{y}} \sin\theta_q \sin\varphi_q + \hat{\mathbf{z}} \cos\theta_q, \\ \mathbf{e}_{\theta_q} &= \hat{\mathbf{x}} \cos\theta_q \cos\varphi_q + \hat{\mathbf{y}} \cos\theta_q \sin\varphi_q - \hat{\mathbf{z}} \sin\theta_q, \\ \mathbf{e}_{\varphi_q} &= -\hat{\mathbf{x}} \sin\varphi_q + \hat{\mathbf{y}} \cos\varphi_q. \end{aligned}$$

When one uses $\cos\theta_q = q_z/k$, $\sin\theta_q = q_r/k$, and $\mathbf{e}_{\sigma} = (\hat{\mathbf{x}} + i\sigma\hat{\mathbf{y}})/\sqrt{2}$, the polarization vector (39) can be rewritten as

$$\mathbf{e}_{\mathbf{q}\sigma} = \frac{1}{\sqrt{2N}} \left(\frac{\cos^2\theta_q + \gamma \sin^2\theta_q}{\cos\theta_q} \mathbf{e}_{\theta_q} + i\sigma \mathbf{e}_{\varphi_q} \right). \tag{40}$$

We notice that, as it should be, all plane-wave components are indeed transverse, i.e., they have no component along $\mathbf{e}_q$. Furthermore, all components are in general elliptically polarized. Looking at different values of γ, we find that (i) $\gamma = 1$: the major axis of the ellipse is along $\mathbf{e}_{\theta_q}$; (ii) $\gamma = 0$: the major axis of the ellipse is along $\mathbf{e}_{\varphi_q}$; and (iii) $\gamma = \gamma_s = \cos\theta_q/(1 + \cos\theta_q)$: the beam is a superposition of circularly polarized plane waves, as discussed by Jentschura and Serbo (2011) and Matula *et al.* (2013). Figure 4 shows the modal recomposition in action producing an OV that captures the qualitative features seen in Fig. 2, with a superposition of only four plane waves (Dennis, O'Holleran, and Padgett, 2009).

Laguerre-Gauss modes are not propagation invariant and thus not characterized by a well-defined q_z. Therefore, their decomposition requires the inclusion of varying q_z (and also q_r), which corresponds to an angular weight function $\mathcal{E}(\theta_q, \varphi_q)$ depending on both the polar and the azimuthal angle (Barnett and Allen, 1994).

The modal decomposition offers an alternative way to study the OV-matter interaction, based on the action of a multitude of plane wave. An example is the treatment of the reflection and refraction of a LG beam impinging at an angle on a dielectric interface to understand the Goos-Hänchen and Imbert-Fedorov effects of OVs (Lusk, Siemens, and Quinteiro, 2019). Here a LG beam is numerically decomposed into plane waves. The Fresnel coefficients then determine the reflection and transmission of each plane wave, which are finally summed up to yield the complete fields. Another interesting example is that of the electronic excitation in bulk semiconductors, in which one may choose to decompose the OV into plane waves to match Bloch electron states, or conversely to retain the simplest representation of an OV in terms of Bessel functions and transform the electronic states to cylindrical coordinates (Sec. IV.A.2).

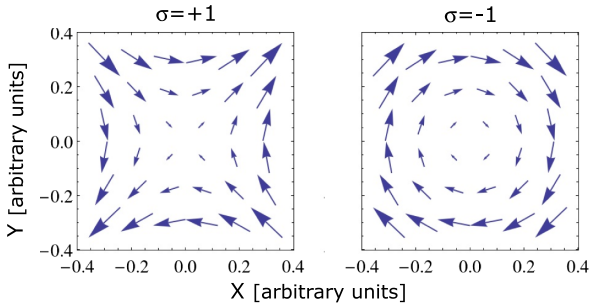

FIG. 4. Vector fields resulting from the sum of four plane waves, each traveling in a direction $\mathbf{q}$ lying on the surface of the same cone but differing in its relative phase. All four plane waves share the same phase $\ell = 1$, but the polarization is $\sigma = +1$ on the left and $\sigma = -1$ on the right. The composite fields are in perfect qualitative agreement with those calculated from Eq. (21) and shown in Fig. 2.

G. Generation and measurement

Optical vortices are now routinely created in many labs. Various techniques to produce such beams are available. They work mostly by converting a laser output beam into an OV, but there are also ways to directly generate a coherent OV beam (Yin, Gao, and Zhu, 2003; Seghilani *et al.*, 2016; Forbes, 2017; Pan *et al.*, 2020).

A spiral phase plate is the most intuitive converter (Kotlyar *et al.*, 2005). It is a transparent cylinder with one of its bases carved into a spiral. A conventional (Gaussian or the like) light beam incident on a base emerges as an OV: geometrically, a ray impinging at a particular position along the surface arc traverses a different optical path than other rays and thus picks a relative phase.

The use of diffraction gratings with dislocations, typically having the shape of a fork, is widely spread (Carpentier *et al.*, 2008). In simple terms, the fringes' design is the pattern resulting from the interference between a plane wave and an OV and printed on a transparent glass; upon illumination by a plane wave (Gaussian beam), different OV beams (orders) are transmitted, with varying topological charge. Fork gratings can also be made to work in reflection. Moreover, a spatial light modulator based on high-resolution liquid crystal displays can be used to modulate the beam in real time.

Other alternative techniques are available. A Q plate is a birefringent liquid crystal that converts SAM into OAM. Some of its advantages are the high conversion efficiency,

the easy alignment, and the Q plate's possible use in a wide range of frequencies (Rubano *et al.*, 2019). As anticipated in Sec. II.A, conical diffraction can be used to generate OV beams (Berry, Jeffrey, and Mansuripur, 2005; Phelan *et al.*, 2009; Turpin *et al.*, 2016); here the cylindrical beam coming out of the biaxial crystal is a superposition of fields with and without OAM that can be separated. Another way is to convert Hermite-Gaussian beams into LG beams with cylindrical lenses (Padgett and Allen, 2002). Metamaterials are also employed to shape beams (Chen *et al.*, 2020; Zhang, Wang *et al.*, 2020). Well suited for photonic applications are microring resonators (Cai *et al.*, 2012; Zhu *et al.*, 2013) and micrometer-size lasers that can emit OVs with controllable topological charge and polarization (Miao *et al.*, 2016; Zhang *et al.*, 2020).

Lastly, we mention that the aforementioned methods focus on creating phase singularities on input beams. The radial profile (LG, Bessel, Mathieu, etc.) has to be further considered and introduced. For example, Bessel beams can be generated using axicons, conical optical elements that transform the beam into a ring by mapping each source point onto the optical axis (Kazak, Khilo, and Ryzhevich, 1999; Arlt and Dholakia, 2000; Jaroszewicz, Burvall, and Friberg, 2005; Bock, Jahns, and Grunwald, 2012).

The same ideas and methods as just described can be used to measure the topological charge of an unknown field (Chen *et al.*, 2020). The most basic fact to learn is whether or not the unknown beam is an OV. This one is determined by making the beam interfere with another one, either a plane wave (Gaussian) or a spherical wave. With the former (latter) the interference pattern of an OV is that of a fork (spiral) (Carpentier *et al.*, 2008). If the beam is indeed an OV, one can infer the topological charge from the number of bifurcations (arms). As expected, this rudimentary method has been by now much improved by more delicate techniques using a single cylindrical lens to measure fractional OAM (Alperin *et al.*, 2016) and spectra of OAM (Volyar *et al.*, 2019), sets of spatial light modulators for real-time measurements (Berkhout *et al.*, 2010), etc.

H. Optical vortices in physics, chemistry, and biology

After the work of Allen *et al.* (1992), the subject of OVs blossomed, especially in optics with research on basic theory, generation, and measurement (Allen, Barnett, and Padgett, 2003; Andrews, 2008). In only a few years it had expanded into other areas of physics.

The interaction of OVs with atoms started with theoretical studies on their motion under the torque exerted by LG beams and the transfer of OAM (Van Enk, 1994; Allen *et al.*, 1996; Andrews, 2008), and experimental work on the interaction of an OV with an ensemble of cold cesium atoms (Tabosa and Petrov, 1999). Several other studies followed, deepening the understanding on the basics of absorption of OVs and exploring other properties, such as the exchange of OAM in the interaction with molecules and the role of the dipole-moment approximation (Babiker *et al.*, 2002), the generation of currents (Köksal and Berakdar, 2012), interaction in an atomic Bose-Einstein condensate (Mondal, Deb, and Majumder, 2014; Bhowmik *et al.*, 2016), the photoexcitation of many-electron atoms (Scholz-Marggraf *et al.*, 2014; Surzhykov *et al.*, 2015), and the photoionization of H_2^+ (Peshkov, Fritzsche, and Surzhykov, 2015). These and other works pointed to the expected transfer of OAM to atoms (internal and center-of-mass degrees of freedom) and to the existence of higher than dipolar electronic transitions (Sec. II.A). Schmiegelow *et al.* (2016) provided a direct experimental demonstration of the transfer of OAM to a single trapped ion, with implications for the importance of the longitudinal component of the field (Quinteiro, Schmidt-Kaler, and Schmiegelow, 2017) (Sec. II.C), the alignment of the beam axis with the atom (Quinteiro, Lucero, and Tamborenea, 2010; Peshkov *et al.*, 2017; Afanasev *et al.*, 2018) (Sec. IV.A.3.b), and the characteristic length scale associated with the singularity (Sec. VI.B.1). Theoretical work continues describing subwavelength trapping (Schulze *et al.*, 2017), interaction with Rydberg atoms (Mukherjee *et al.*, 2018), the scattering by hydrogenic ions (Peshkov *et al.*, 2018), resonant scattering by fast ions (Serbo, Surzhykov, and Volotka, 2022), multipolar transitions (Solyanik-Gorgone *et al.*, 2019), Bose-Einstein condensates (Das *et al.*, 2020; Ghosh Dastidar *et al.*, 2022), trapping by counterpropagating beams (Koksal *et al.*, 2019, 2020), etc. (Franke-Arnold, 2017; Babiker, Andrews, and Lembessis, 2019).

Studies of atom-OV interactions have been accompanied by studies of molecules. A primary concern has been to establish whether the OAM of light plays a role in chiral molecule-light interactions, as is well known with spin AM. Studies pointing in the positive direction (OAM does affect chiral matter) (Rosales Guzmán, 2015; Brullot *et al.*, 2016; Forbes and Andrews, 2018b; Woźniak *et al.*, 2019; Ye *et al.*, 2019) and negative direction (Babiker *et al.*, 2002; Andrews, Dávila Romero, and Babiker, 2004; Araoka *et al.*, 2005; Löffler, Broer, and Woerdman, 2011; Mathevet *et al.*, 2013; Giammanco *et al.*, 2017) exist, and the accumulated evidence thus far indicates that the effect does take place at the quadrupole electronic transition level (Sec. III.C.1) and can be induced using Bessel beams or tight focusing mixing orbital and spin AMs (Zhao *et al.*, 2007; Monteiro, Neto, and Nussenzveig, 2009) (Sec. II.C.2). Other research into more general properties of OV-molecule interactions were conducted on the photoinduced currents and magnetic fields in ring-shaped molecules (Köksal and Koç, 2017a) and nanocages (Köksal and Koç, 2017b), and twisted excitons in molecules (Zang and Lusk, 2017).

Other fields also profit from OVs. The propagation properties of OVs in a plasma were investigated by Nobahar, Hajisharifi, and Mehdian (2019), and Zhang *et al.* (2021) proposed the generation of high-order OV harmonics by irradiating a plasma with a circularly polarized Gaussian beam. Optical vortices out of the visible spectrum have also been investigated. In the ultraviolet regime, they can improve lithography and ablation techniques (Hernández-García *et al.*, 2017; Pabon *et al.*, 2017). Metalenses can generate OVs in microwaves (Zhang *et al.*, 2018) and V-shaped antennas can generate OVs in the terahertz range (He *et al.*, 2013). In the radio frequency regime corresponding studies were conducted (Thidé *et al.*, 2007, 2014; Mohammadi *et al.*, 2010). In astronomy, the so-called vortex coronograph technique can be used to improve the imaging of exoplanets (Foo, Palacios, and

Swartzlander, 2005; Serabyn, Mawet, and Burruss, 2010), and there are methods to determine the OAM of light from astronomical sources (Berkhout and Beijersbergen, 2008) or the rotation of these sources (Tamburini *et al.*, 2011; Lavery *et al.*, 2013). In biology, Shi *et al.* (2017) studied the transmission of LG beams through mouse brain tissue to explore possible uses of OVs for imaging purposes. Optical tweezers with OVs can help manipulate biological molecules and structures (Grier, 2003; Otte and Denz, 2020). In addition, single-cell nanosurgery using OVs is reported to produce less damage in organelles than conventional optical tweezers (Jeffries *et al.*, 2007). Finally, OVs can significantly improve microscopy, such as in biology and nanotechnology, by stimulated emission depletion (STED) (Keller, Schönle, and Hell, 2007) and other techniques (Ritsch-Marte, 2017).

III. CONDENSED-MATTER BASICS

Condensed-matter physics encompasses a vast collection of phenomena in different materials, from liquids to crystalline solids. This review focuses on the interaction of OVs with bulk solids and structured systems like quantum rings, a two-dimensional electron gas either in a quantum well or in modern two-dimensional (2D) materials, quantum dots, semiconductor microcavities, dielectric-metal interfaces, and topological insulators. In this section, we discuss the basic physics behind crystals in the bulk and nanostructure forms, their excitations, such as single-particle excitations, excitons, exciton polaritons, and plasmon polaritons, and condensed-matter optics including the topics of gauge invariance, the vertical-transition approximation, and the dynamics of the material excitations.

A. Crystalline solids

A crystal is a solid with well-ordered elementary units, either atoms or collections of atoms, forming a lattice. This periodicity determines much of the electronic structure and single-particle excitations, as well as the dynamics of their collective excitations (excitons, plasmons, phonons, and magnons) (Ashcroft and Mermin, 1976; Kittel, 1987; Ibach and Lüth, 2013).

A classification criterion advantageous to discuss optical processes is to separate the set of crystalline solids into insulators, semiconductors, and metals, i.e., by their electrical conductivity. The description of electron dynamics in solids was continuously improved in successive steps. Drude (1900) postulated his model for conduction in metals, in which electrons move according to Newton's laws including the Lorentz force, bounce on fixed and randomly located ions, and thermalize to a classical Maxwell-Boltzmann velocity distribution. The Drude model explained the Hall effect, and combined with experiments it predicted electron relaxation times and mean free paths in metals. It is still a ubiquitous tool in research and plays an important role in the theory of surface plasmon polaritons (Sec. IV.C). Sommerfeld (1928) introduced the Fermi-Dirac distribution and the wave nature of electrons through the free-electron wave functions $\exp(i\mathbf{k}\cdot\mathbf{r})$ with the quasimomentum $\mathbf{k}$. A significant improvement comes from incorporating the periodicity of the ionic

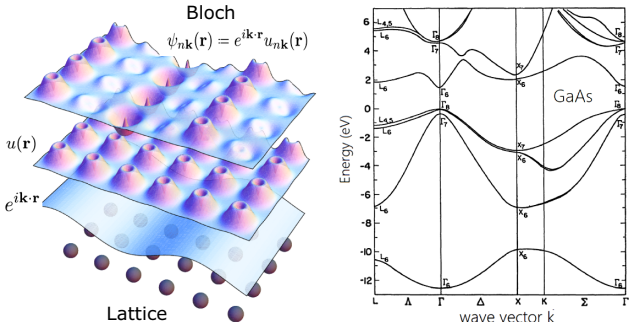

FIG. 5. In the independent-electron approximation, the single electron states are grouped into energy bands due to their interaction with the lattice. Left panel: schematic plot of the Bloch wave functions. Right panel: band structure of GaAs. Adapted from Cohen and Chelikowsky, 2012.

arrangement (Bragg and Bragg, 1913). The general form of the electron wave function in a periodic potential is given by the Bloch theorem (Bloch, 1929), which states that the single-particle wave function $\psi_{b\mathbf{k}}(\mathbf{r})$ can be written as

$$\psi_{b\mathbf{k}}(\mathbf{r}) = \frac{1}{\sqrt{V}} e^{i\mathbf{k}\cdot\mathbf{r}} u_{b\mathbf{k}}(\mathbf{r}), \tag{41}$$

with the quasimomentum $\mathbf{k}$,[6] the band index b, and a normalization volume V. The microscopic function $u_{b\mathbf{k}}(\mathbf{r})$ has the periodicity of the lattice and satisfies the following orthogonality relation:

$$\frac{1}{v}\int_v d\mathbf{r}\, u^*_{b'\mathbf{k}}(\mathbf{r}) u_{b\mathbf{k}}(\mathbf{r}) = \delta_{bb'}, \tag{42}$$

where the integral runs over a single unit cell with volume v. The electron states are grouped in energy bands with the energy $\varepsilon_{b\mathbf{k}}$ (Ashcroft and Mermin, 1976). The Bloch description together with the Fermi-Dirac statistics of the electrons finally achieves a microscopic description of metals, semiconductors, and insulators. In conductors, the electronic ground state is characterized by partially filled energy bands. In contrast, semiconductors and insulators have at zero temperature fully occupied energy bands separated by a band gap from empty energy bands; see Fig. 5.

In contrast to the fairly simple solution for energy bands and wave function found in the Bloch model, the many-body problem of electron-electron interactions is of such complexity that no single solution is known. Instead, approximations to specific situations are applied. *Ab initio* calculations of the electronic structure of solids are most often based on the density-functional theory and its variants (Hohenberg and Kohn, 1964; Kohn and Sham, 1965). In the optical excitation of a direct band-gap semiconductor (such as GaAs; see Fig. 5), the absorption of light induces the transition of electrons between the valence and conduction bands. The mutual interaction between electrons and holes gives rise to quasiparticles called excitons (Frenkel, 1931; Wannier, 1937). Here the essential physics is captured by the dynamical

[6]Rigorously speaking, the quasimomentum of the electron is $\hbar\mathbf{k}$.

Hartree-Fock approximation, a mean-field approach leading to the semiconductor Bloch equations (Lindberg and Koch, 1988; Rossi and Kuhn, 2002; Haug and Koch, 2009). An alternative approach is based on the Bethe-Salpeter equation for the two-particle correlation function (Strinati, 1988; Albrecht *et al.*, 1998; Rohlfing and Louie, 1998; Onida, Reining, and Rubio, 2002; Drueppel *et al.*, 2018).

A lattice made out of static ions is unrealistic; not only temperature but also quantum fluctuations cause the ions to move. At low temperatures, every ion undergoes small oscillations around its equilibrium position (lattice site) that lead to the normal modes of vibrations, with the dispersion relation $\omega_s(\mathbf{k})$ for branch s and wave vector $\mathbf{k}$. A quantum description yields the picture of phonons as the quanta of crystal vibrations, which are analogous to photons in quantum electrodynamics (Ashcroft and Mermin, 1976; Ibach and Lüth, 2013).

The spin degree of freedom of electrons and ions plays an important role in optical selection rules and a variety of magnetic phenomena. We discuss its relevance to OV-crystal interactions in Sec. IV.A.3.a.

The evolution in our understanding of electronic excitations is an example of how particles are to be thought of in solid-state physics. In Drude's and Sommerfeld's models electrons are individual particles randomly scattering from individual ions. Incorporating the effect of the entire lattice potential leads to "dressed" states and the corresponding quasiparticles, the Bloch electrons. Incorporating the electron-electron interaction leads to Landau's quasiparticles (Abrikosov, Gorkov, and Dzyaloshinski, 2012) in metals and excitons in semiconductors (Dexter and Knox, 1965).

This process of hybridization of correlated excitations yielding new quasiparticles goes on: including light as a degree of freedom, one finds exciton (Sec. IV.B) and plasmon (Sec. IV.C) polaritons or, including phonons, one finds polarons. A description based on collective excitations is a clever way to deal with the complexity found in condensed matter and also hints at the interconnectedness of idealized individual physical units (such as the Sommerfeld electron).

B. Structured systems

Modern technology and condensed-matter physics are inextricably intertwined. The electronic industry based on the solid state has constantly sought device miniaturization, since the invention of the transistor in the late 1940s or even earlier (Mills, 2011), and it has driven intense basic research on small semiconductor, metal, and hybrid structures; see Fig. 6.

The theory of nanoscale (10^{-9}–10^{-8} m) systems is built upon that of the bulk crystal and is discussed in Secs. III.C.3 and IV.A.1. However, nanostructures exhibit new effects due to their reduced dimensionality, the number of excitations involved, the existence of interfaces, the combination of different materials, etc., that require a reexamination of bulk models. Are the classical and semiclassical (e.g., Drude) models applicable? Can one use thermodynamics for a system with few particles? What assumptions are not valid for optics at the nanoscale? The result of almost half a century of research is a well-developed understanding of nanostructures that deserves dedicated attention (Bastard, 1988; Ihn, 2010).

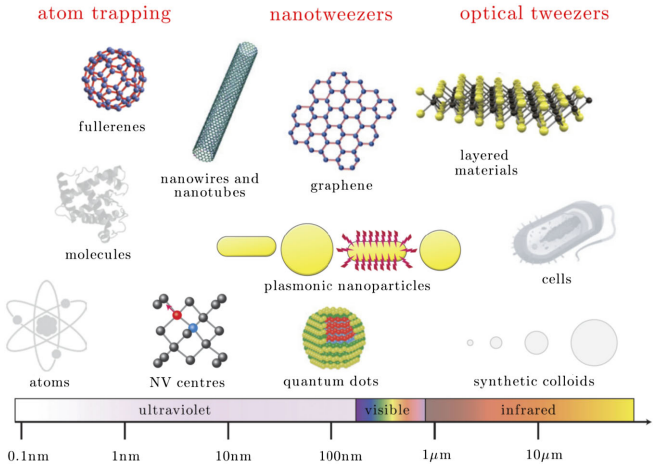

FIG. 6. Comparison of structures of different types and sizes. From Maragò *et al.*, 2013.

Section IV discusses in depth the interaction of OVs with structured systems.

C. Condensed-matter optics

Among crystals, semiconductors exhibit the richest response to light in the visible range of the electromagnetic spectrum. Halfway between metals and insulators, the electronic ground state has a completely filled valence (highest occupied energy) band separated from a completely empty conduction (lowest unoccupied energy) band by a few electron volts. Light in the visible range therefore carries the necessary amount of energy to induce electronic interband transitions between the valence and conduction bands. Metals with the Fermi energy lying inside the conduction band and metallic-dielectric hybrid systems also present interesting features. Their interaction with light is to a large extent understandable in terms of the Drude model for electrons in a single band (Sec. IV.C).

The general formulation of the light-matter interaction is based on the minimal-coupling Hamiltonian, in which the electromagnetic field is described in terms of potentials instead of fields. As discussed in Sec. II.B, potentials are not uniquely defined by the fields; instead, different gauges can be chosen. In an analysis of light-matter interactions, the consideration of the problem of gauge invariance is therefore important, particularly in the case of extended systems (solid-state bulk materials or nanostructures) and/or strongly varying electromagnetic fields (Sec. III.C.1). Owing to the phase singularities, OVs are indeed strongly varying fields; moreover, under certain experimental conditions the spatial variation can be further enhanced by tight focusing of a free propagating beam or by near-field techniques (Sec. IV.C).

A prevailing model of the interband optical excitation is that of vertical transitions, in which the photon's linear momentum is neglected. However, the vertical-transition approximation is incompatible with strongly inhomogeneous light beams such as OVs, and thus must be revisited (Sec. III.C.2).

Finally, the modeling of the dynamics of the optical excitation and the subsequent relaxation and dephasing

processes of the generated electronic excitations are discussed in Sec. III.C.3.

1. Gauge invariance

As a starting point for a theoretical description of the light-matter interaction (Cohen-Tannoudji, Dupont-Roc, and Grynberg, 1989), it is convenient to take the following Lagrangian L for a particle of charge q and mass m_0 in the presence of electromagnetic fields represented by scalar (Φ) and vector ($\mathbf{A}$) potentials [see Chap. 1 of Goldstein (1980)]:

$$L = \tfrac{1}{2}m_0\dot{\mathbf{r}}^2 - V(\mathbf{r}) + q\dot{\mathbf{r}}\cdot\mathbf{A}(\mathbf{r},t) - q\Phi(\mathbf{r},t), \tag{43}$$

with the electrostatic potential energy V due to the lattice and possibly other static sources and the canonical momentum

$$\mathbf{p} = \frac{\partial L}{\partial \dot{\mathbf{r}}} = m_0\dot{\mathbf{r}} + q\mathbf{A}(\mathbf{r},t). \tag{44}$$

Using a Legendre transformation $h = \mathbf{p}\cdot\dot{\mathbf{r}} - L$ the so-called minimal-coupling Hamiltonian is obtained as

$$h = \frac{1}{2m_0}[\mathbf{p} - q\mathbf{A}(\mathbf{r},t)]^2 + V(\mathbf{r}) + q\Phi(\mathbf{r},t), \tag{45}$$

which is the key quantity for the transition to a quantum mechanical description. The Hamiltonian is likewise expressed in terms of the electromagnetic potentials instead of the fields. This can be a source of trouble in calculations and the interpretation of results, particularly if approximations like the truncation of a basis are performed.

Electromagnetic potentials are auxiliary functions that assist us in the calculations involving the physically real and measurable electric and magnetic fields. Gauge transformations do not change the fields (Sec. II.B): The values of measurable electromagnetic quantities and their dynamics (governed by Maxwell's equations) are unaffected.

When charges enter the picture, one expects to have corresponding invariant equations of motion (EOMs) and quantities. The Schrödinger equation for the minimal-coupling Hamiltonian is preserved under a gauge transformation if the wave function undergoes a local phase transformation[7] $\psi^{(2)} = T_\chi\psi^{(1)} = \exp(iq\chi/\hbar)\psi^{(1)}$. The Hamiltonian transforms concomitantly by[8] $h^{(2)} = T_\chi h^{(1)}T_\chi^\dagger - q\partial_t\chi$. All other operators transform according to $O^{(2)} = T_\chi O^{(1)}T_\chi^\dagger$, which ensures that matrix elements and mean values of operators are invariant: $\langle\psi^{(1)}|O^{(1)}|\varphi^{(1)}\rangle = \langle\psi^{(2)}|O^{(2)}|\varphi^{(2)}\rangle$. Note the special transformation rules that obey h (the operator driving the system's dynamics) and the scalar and vector potentials [Eqs. (12a) and (12b)]. A physically meaningful quantity $\mathcal{O}$ should have gauge-invariant eigenvalues of its operator O, and it should retain its functional form upon transformation: $O^{(2)} = O^{(1)}(\mathbf{A}^{(2)},\Phi^{(2)})$ (Scully and Zubairy, 1997). Examples of physical and nonphysical quantites are the mechanical ($\boldsymbol{\pi} = \mathbf{p} - q\mathbf{A}$) and canonical ($\mathbf{p} = -i\hbar\boldsymbol{\nabla}$) momenta, respectively. Evidently the Hamiltonian (45) is not a physical operator, but by excluding the scalar potential one gets a physical operator called the instantaneous energy (Yang, 1976). Nor is $h_0 = \mathbf{p}^2/(2m_0) + V$ a physical operator if $\mathbf{A} \neq 0$.

In addition to eigenvalues and expectation values of operators, one is concerned with the transition probabilities (Yang, 1976; Ballentine, 2014) induced by the optical field. These transition rates are usually calculated in the framework of time-dependent perturbation theory. For this purpose the minimal-coupling Hamiltonian is split into an unperturbed part

$$h_0 = \frac{\mathbf{p}^2}{2m_0} + V(\mathbf{r})$$

in the absence of electromagnetic fields and a perturbation that depends on scalar and/or vector potentials such as

$$h_I = -\frac{q}{2m_0}[\mathbf{p}\cdot\mathbf{A}(\mathbf{r},t) + \mathbf{A}(\mathbf{r},t)\cdot\mathbf{p}] + q\Phi(\mathbf{r},t), \tag{46}$$

in which the quadratic term in $\mathbf{A}$ has been neglected. Perturbation theory then predicts transition rates between eigenvectors $|\eta_i\rangle$ of h_0, satisfying the eigenvalue equation $h_0|\eta_i\rangle = \varepsilon_i|\eta_i\rangle$. In most cases one is interested in the transition rates for monochromatic fields with frequency ω, for which the interaction Hamiltonian (like the potentials and fields) can be split into a positive and a negative frequency part according to

$$h_I = h_I^{(+)}e^{-i\omega t} + h_I^{(-)}e^{i\omega t}. \tag{47}$$

Transition rates in first-order perturbation theory (describing single-photon absorption or emission processes) are then given as follows by Fermi's golden rule:

$$\Gamma_{fi} = \frac{2\pi}{\hbar}[|\langle\eta_f|h_I^{(+)}|\eta_i\rangle|^2\delta(\varepsilon_f - \varepsilon_i - \hbar\omega) + |\langle\eta_f|h_I^{(-)}|\eta_i\rangle|^2\delta(\varepsilon_f - \varepsilon_i + \hbar\omega)]. \tag{48}$$

Using higher-order perturbation theory, transition rates for multiphoton absorption and emission processes can be obtained.

These transition rates involve gauge-dependent quantities. Therefore, the following question arises: Do the transition rates change if the potentials are transformed by a gauge function χ according to Eqs. (12a) and (12b), leading to a modified interaction Hamiltonian $h_I^{(2)} = h_I^{(1)} + \Delta h_{I\chi}$, where $h_I^{(1)}$ refers to the interaction Hamiltonian in the original gauge? Using the fact that χ has a harmonic time dependence and can be separated into positive and negative frequency components, the correction terms are given by

$$\Delta h_{I\chi}^{(\pm)} = -\frac{q}{2m_0}[\mathbf{p}\cdot\boldsymbol{\nabla}\chi^{(\pm)}(\mathbf{r}) + \boldsymbol{\nabla}\chi^{(\pm)}(\mathbf{r})\cdot\mathbf{p}] \pm i\omega q\chi^{(\pm)}(\mathbf{r}). \tag{49}$$

As can be easily checked, the gauge field satisfies the commutation relation

[7] This is also the case in relativistic quantum mechanics with the Dirac equation.

[8] The transformed Hamiltonian can also be written by replacing old potentials by new potentials.

$$[h_0, \chi^{(\pm)}(\mathbf{r})] = \frac{\hbar}{2m_0 i}[\mathbf{p}\cdot\nabla\chi^{(\pm)}(\mathbf{r}) + \nabla\chi^{(\pm)}(\mathbf{r})\cdot\mathbf{p}]. \quad (50)$$

Using this relation, the matrix elements of the correction terms to the interaction Hamiltonian are given by

$$\langle\eta_f|\Delta h_{I_\chi}^{(\pm)}|\eta_i\rangle = -\frac{iq}{\hbar}(\varepsilon_f - \varepsilon_i \mp \hbar\omega)\langle\eta_f|\chi^{(\pm)}(\mathbf{r})|\eta_i\rangle. \quad (51)$$

These matrix elements therefore vanish when the energies satisfy the energy selection rules in Eq. (48). We can draw several conclusions from this result: (i) transition rates for resonant transitions, as described by Fermi's golden rule, are unchanged and are therefore gauge invariant; (ii) this no longer holds if approximate eigenfunctions of h_0, such as those from a variational calculation, are used for the rate calculation (Dalgarno and Lewis, 1956); and (iii) transitions in the case of a decaying states may also depend on the gauge (Fried, 1973; Lamb, Schlicher, and Scully, 1987). This is again related to the fact that h_0 does not completely describe the unperturbed system, but there are other parts, such as electron-phonon interactions or radiative decay due to the coupling to the photon vacuum, which lead to dephasing and a finite lifetime of the excited state.

For two-photon transitions, where the rate involves the summation of intermediate states, it has been shown that the exact result from second-order perturbation theory is independent of the gauge, while a truncation of the basis of the intermediate states can lead to strongly gauge-dependent results, and the convergence behavior with an increasing number of basis functions may strongly depend on the gauge (Bassani, Forney, and Quattropani, 1977). Furthermore, nonresonant two-photon transitions in the case of a broadened line may also depend on the gauge (Kobe, 1978). However, for broadenings that are not too large this gauge dependence will be weak because the deviations of the energy from the resonance condition are small.

To avoid such possible gauge dependencies one may try to find a formulation of the coupling only in terms of measurable fields. The dipole-moment approximation for the coupling of light to atoms (or other sufficiently localized structures) accomplishes this. We assume that a smooth external electromagnetic field with wavelength much larger than the spatial extent of the electron wave function is impinging on an atom centered at $\mathbf{r} = 0$. If the sources of the field are far away, $\Phi^{(1)} \simeq 0$ can be assumed and $\mathbf{A}^{(1)}(\mathbf{r}, t)$ can be approximated as $\mathbf{A}^{(1)}(0, t)$. The Hamiltonian in the Coulomb gauge then reads $h^{(1)} = [\mathbf{p} - q\mathbf{A}^{(1)}(0,t)]^2/2m_0 + V(\mathbf{r})$. The Göppert-Mayer (1931) gauge transformation $\chi = -\mathbf{r}\cdot\mathbf{A}^{(1)}(0,t)$ produces new potentials $\mathbf{A}^{(2)} = 0$ and $\Phi^{(2)} = -\mathbf{r}\cdot\mathbf{E}(0,t)$, and consequently $h^{(2)} = \mathbf{p}^2/2m_0 + V(\mathbf{r}) - q\mathbf{r}\cdot\mathbf{E}(0,t)$, i.e., a Hamiltonian completely described in terms of the electric field.

We note, however, that the Hamiltonian with the electric dipole coupling is only an approximation. The exact gauge transformation results in a vector potential $\mathbf{A}^{(2)}(\mathbf{r}, t) = \mathbf{A}^{(1)}(\mathbf{r}, t) - \mathbf{A}^{(1)}(0, t)$, which vanishes only in the case of a homogeneous electromagnetic field, i.e., in the limit of an infinite wavelength. Moreover, even in the case of a system much smaller than the wavelength one can find a gauge transformation to a null vector potential only in the cases in which the coupling to the magnetic field is negligible. If there is a non-negligible magnetic coupling, $\mathbf{A} \neq 0$ in all gauges.

In general, the dipole-moment approximation fails to describe extended matter states and/or highly inhomogeneous light fields. In the case of the coupling to a crystalline solid, however, a formulation in terms of dipole moments remains possible due to the Bloch theorem and the shortness of the length of the unit cell compared to the wavelength. The dipole moment then refers to a single unit cell. In other cases it can be improved by other gauge transformations (Cohen-Tannoudji, Dupont-Roc, and Grynberg, 1989; Quinteiro, Reiter, and Kuhn, 2015, 2017b) or by formally extending the dipole-moment Hamiltonian to $h_I = -q\mathbf{r}\cdot\mathbf{E}(\mathbf{r}, t)$ (Kira *et al.*, 1999). All these transformations share the fact that they retain some spatial dependence of the potentials and fields; see Sec. IV.A.2.

2. Vertical-transition approximation

A widely used approximation in semiconductor optics is that of vertical transitions (Dresselhaus, 2001). The excitation of an electron from the valence to the conduction band annihilates a photon with energy around that of the semiconductor band gap. We exemplify this for the excitation of a GaAs bulk crystal (band-gap energy $E_g = 1.44$ eV at 300 K). The corresponding photon's linear momentum[9] is $q \simeq 8 \times 10^{-3}$ nm^{-1}. The quasimomentum k of the electron is restricted to the first Brillouin zone with maximum value $k_{\max} = \pi/a \simeq 6$ nm^{-1}, where a is the linear size of the unit cell. By arguing that $q \ll k_{\max}$, one often neglects q. This is equivalent to neglecting the spatial variation of the light field over a unit cell. Futhermore, neglecting the spatial variation of the light field over the entire system leads to the vertical-transition approximation. In the electron-hole or exciton picture a vertical transition corresponds to the generation of an electron-hole pair or an exciton with vanishing center-of-mass momentum.

This vertical-transition approximation has proven to be useful. However, the conservation of linear momentum in light-matter interactions must be taken into account in some cases of historical and current interest. In the late 1950s Hopfield (1958) developed the theory of hybrid exciton-photon quasiparticles, known as exciton polaritons, a topic that has attracted renewed interest in recent years, particularly in the field of semiconductor nanostructures, and is currently being extensively explored in theory, experiments, and applications (Sec. IV.B). A decade later and almost simultaneously, Gibson, Kimmitt, and Walker (1970), and Grinberg (1970) investigated the photon-drag effect (Gibson and Walker, 1971; Cameron *et al.*, 1975). In Grinberg's words, "In the absorption of light by free carriers, the momentum of the electromagnetic wave is absorbed together with its energy. Consequently, the electron system can acquire a translational motion that is manifest in the form of a current or a voltage." The effect is currently being used in commercial detectors. If the light is circularly polarized, carriers may pick both the photon's linear momentum and the spin AM, resulting in the generation of a spin-dependent electric current (Shalygin *et al.*, 2007).

[9]Rigorously speaking, the photon's linear momentum is $\hbar\mathbf{q}$.

Taking into account the linear momentum of the photon, the transitions are no longer vertical. Nevertheless, there is still a well-defined momentum transfer. In the electron-hole picture the generated electron-hole pair has a center-of-mass momentum given by the photon's momentum. In contrast, for strongly inhomogeneous light fields the photon no longer has a well-defined momentum, which leads to a broadening of the transitions in k space and thus to an uncertainty in the center-of-mass momentum of the generated exciton or electron-hole pair (Hess and Kuhn, 1996; Rossi and Kuhn, 2002; Herbst *et al.*, 2003).

In structures with cylindrical symmetry it is often convenient to characterize the electronic state not by the linear momentum $\mathbf{k}$ but by its OAM with respect to the symmetry axis, which is specified by a quantum number m. Here a light field that can be assumed to be spatially homogeneous over the structure leads to "vertical" transitions in the sense that the quantum numbers m of the initial and final states in an absorption or emission process are the same.

To describe the interaction of OVs with condensed matter, the assumption of a slowly varying field is violated, particularly in the region around the phase singularity, and therefore has to be abandoned. Here the transfer of OAM has to be incorporated into the models in a similar way as the linear momentum in the case of polaritons or the photon-drag effect. In fact, based on such an approach circular photocurrents in bulk materials (Quinteiro and Tamborenea, 2009c) and nanostructures (Quinteiro and Berakdar, 2009) have been predicted. Recent measurements have confirmed this effect (Ge, 2020; Ji *et al.*, 2020).

3. Dynamics under light excitation

In a nutshell, a light beam creates an out-of-equilibrium many-electron state by altering the populations of conduction and valence bands as well as the quantum coherences within and between bands (Rossi and Kuhn, 2002). With no further energy input, the overall state eventually relaxes and loses quantum coherence through different channels, most notably electron-phonon and electron-electron scattering and radiative recombination. Many tools have been developed to measure and model the generation of a nonequilibrium state in matter by means of an optical excitation and the subsequent relaxation and dephasing back to the equilibrium state.

The dynamics of optically excited semiconductors are described starting from a second quantization picture with creation (annihilation) operators $a^\dagger_{b\alpha}$ ($a_{b\alpha}$) denoting the creation (annihilation) of an electron in the state $\psi_{b\alpha}(\mathbf{r})$ in band b with quantum number α. In bulk material α is the three-dimensional wave vector $\mathbf{k}$ of the Bloch electron, and the Bloch function $\psi_{b\mathbf{k}}(\mathbf{r})$ is given by Eq. (41). In a spatially confined system α may be a purely discrete (multi)index (as in the case of a quantum dot) or a combination of a discrete and a continuous index (such as a subband index and a two-dimensional wave vector in the case of a quantum well). The states in such systems are often well described in terms of the envelope-function approximation (Bastard, 1988; Ihn, 2010) by a wave function

$$\psi_{b\alpha}(\mathbf{r}) = \mathcal{E}_{b\alpha}(\mathbf{r}) u_b(\mathbf{r}), \tag{52}$$

for a state with energy $\varepsilon_{b\alpha}$. Here $\mathcal{E}_{b\alpha}(\mathbf{r})$ denotes the envelope function and the k dependence of the lattice-periodic Bloch function is neglected; i.e., $u_{b\mathbf{k}}(\mathbf{r})$ is replaced by the function at the band edge $u_{b\mathbf{k}_0}(\mathbf{r}) = u_b(\mathbf{r})$ (Bastard, 1988). The Hamiltonian of the noninteracting electrons then reads

$$H_0 = \sum_{b\alpha} \varepsilon_{b\alpha} a^\dagger_{b\alpha} a_{b\alpha}, \tag{53}$$

while the coupling to a light field in any gauge has the general structure

$$H_I = \sum_{b'\alpha',b\alpha} h^I_{b'\alpha',b\alpha} a^\dagger_{b'\alpha'} a_{b\alpha}, \tag{54}$$

with $h^I_{b'\alpha',b\alpha} = \langle b'\alpha'|h_I|b\alpha\rangle$ and the interaction Hamiltonian h_I, as in Eq. (46).

The expectation value of any single-particle operator of the electrons can be calculated from the single-particle density matrix

$$\rho_{b'\alpha',b\alpha}(t) = \langle a^\dagger_{b'\alpha'}(t) a_{b\alpha}(t)\rangle, \tag{55}$$

which satisfies the equation of motion

$$\begin{aligned} i\hbar \frac{d}{dt}\rho_{b'\alpha',b\alpha} &= \langle [a^\dagger_{b'\alpha'} a_{b\alpha}, H_0 + H_I]\rangle \\ &= (\varepsilon_{b\alpha} - \varepsilon_{b'\alpha'})\rho_{b'\alpha',b\alpha} \\ &\quad + \sum_{b''\alpha''} (h^I_{b\alpha,b''\alpha''}\rho_{b'\alpha',b''\alpha''} - h^I_{b''\alpha'',b'\alpha'}\rho_{b''\alpha'',b\alpha}). \end{aligned} \tag{56}$$

Note that while in Eq. (56) we have explicitly used the Heisenberg picture, $\rho_{b'\alpha',b\alpha}(t)$ as an expectation value is independent of the picture and the same Eq. (56) could be obtained using the Liouville–von Neumann equation in the Schrödinger picture. When dealing with the dynamics of optically excited semiconductors, it is often sufficient to restrict the model to two bands, the valence band (v) and the conduction band (c). The system is then described using three single-particle density matrices, the intraband coherences $\rho_{v,\alpha'\alpha} \equiv \rho_{v\alpha',v\alpha}$ and $\rho_{c,\alpha'\alpha} \equiv \rho_{c\alpha',c\alpha}$ (including occupations for $\alpha = \alpha'$), and the interband coherence $\rho_{vc,\alpha'\alpha} \equiv \rho_{v\alpha',c\alpha}$. We return to these equations for various types of structures later in the review. As a reference for the description of solid-state systems driven by OVs, here we give an overview of the theoretical background for the standard case of a bulk semiconductor excited by a homogeneous light field.

In the case of a homogeneous excitation of a bulk semiconductor, the single-particle density matrices are diagonal in the wave vector $\mathbf{k}$ and the dynamical variables reduce to the electron occupations in the valence and conduction bands $\rho_{v,\mathbf{k}}$ and $\rho_{c,\mathbf{k}}$, as well as the interband coherence (also called the interband polarization) $\rho_{vc,\mathbf{k}}$. The coupling to the light field is treated in terms of the vertical-transition approximation. The interaction matrix elements in the electric-field gauge then reduce to $h^I_{c\mathbf{k},v\mathbf{k}} = -\mathbf{d}_{cv}\cdot\mathbf{E}(t)$ with the interband dipole matrix element

$$\mathbf{d}_{cv} = \frac{q}{v}\int_v u_c^*(\mathbf{r})\mathbf{r}u_v(\mathbf{r})d\mathbf{r}. \tag{57}$$

A more detailed discussion of the coupling to the light field including intraband and interband processes as well as spatially inhomogeneous light fields is given in Sec. IV.A.1.

In the simplest case the optical excitation is described in terms of a generation rate $g_{\mathbf{k}}$ according to

$$\frac{d}{dt}\rho_{c,\mathbf{k}} = -\frac{d}{dt}\rho_{v,\mathbf{k}} = g_{\mathbf{k}}, \tag{58}$$

where $g_{\mathbf{k}}$ is obtained from Fermi's golden rule and reads, for a spatially homogeneous light field $\mathbf{E}$ with frequency ω,

$$g_{\mathbf{k}} = \frac{2\pi}{\hbar^2}|\mathbf{d}_{cv}\cdot\mathbf{E}|^2(\rho_{v,\mathbf{k}} - \rho_{c,\mathbf{k}})\delta(\omega_{\mathbf{k}} - \omega), \tag{59}$$

with $\hbar\omega_{\mathbf{k}} = \varepsilon_{c\mathbf{k}} - \varepsilon_{v\mathbf{k}}$. In the case of excitation by a short laser pulse, the δ function is replaced by the spectral shape of the pulse.

The coupling to the light field, however, not only generates populations of electrons and holes, it also creates an interband coherence $\rho_{vc,\mathbf{k}}$ between the light-coupled states. In the present case of noninteracting electrons, a closed set of EOMs for the occupations and the interband coherence is obtained as

$$\frac{d}{dt}\rho_{c,\mathbf{k}} = -\frac{d}{dt}\rho_{v,\mathbf{k}} = -\frac{2}{\hbar}\mathrm{Im}[\mathbf{d}_{cv}\cdot\mathbf{E}(t)\rho^*_{vc,\mathbf{k}}], \tag{60a}$$

$$\frac{d}{dt}\rho_{vc,\mathbf{k}} = -i\omega_{\mathbf{k}}\rho_{vc,\mathbf{k}} + \frac{i}{\hbar}\mathbf{d}_{cv}\cdot\mathbf{E}(t)(\rho_{v,\mathbf{k}} - \rho_{c,\mathbf{k}}), \tag{60b}$$

with $\mathrm{Im}[\cdots]$ denoting the imaginary part. Each optically coupled pair of valence- and conduction-band states represents a two-level system and Eqs. (60a) and (60b) correspond to a set of optical Bloch equations (OBEs) for these two-level systems (Haug and Koch, 2009). An extension including intraband terms of the electric field was given by Rossi and Kuhn (2002). Generalizations of the OBEs to the case of excitation of semiconductor bulk and various elementary nanostructures are discussed in Secs. IV and V.

The EOMs (60a) and (60b) were derived in the electron picture. Alternatively, one may work in the electron-hole picture, in which the annihilation of an electron with the wave vector $\mathbf{k}$ in the valence band is replaced by the generation of a hole with the wave vector $-\mathbf{k}$. Instead of the occupation of the valence-band states, one then uses the occupation of the hole states given by $\rho_{h,-\mathbf{k}} = 1 - \rho_{v,\mathbf{k}}$; the other two variables remain the same. The excitation of an electron from the valence to the conduction band is then interpreted as the generation of an electron-hole pair, where the electron and the hole have opposite momenta. An advantage of the electron-hole picture is the fact that before the optical excitation the system is in a well-defined vacuum state with all dynamical variables being zero. In this review, however, we mainly use the equally valid electron picture because it provides more compact notation, especially in systems with more than two bands or when intraband processes are included.

In a real semiconductor, particularly in the case of excitation close to the band gap, the many-body nature of the electronic system cannot be neglected. The attractive Coulomb interaction between the electron and the hole leads to the formation of bound exciton states that manifest themselves in discrete absorption lines below the band gap. The general structure of the electron-electron interaction Hamiltonian in a multiband model is given by

$$H_{ee} = \frac{1}{2}\sum_{ijkl}\langle ij|h_{ee}|kl\rangle a_i^\dagger a_j^\dagger a_l a_k, \tag{61}$$

in which the latin characters represent band and envelope indices (for example, $i = b_i\alpha_i$) and

$$h_{ee} = \frac{q^2}{4\pi\epsilon_0\epsilon_s|\mathbf{r}-\mathbf{r}'|},$$

with the static dielectric constant ϵ_s. For the two-band bulk system of Bloch states, this leads to

$$H_{ee} = \frac{1}{2}\sum_{\mathbf{k}\mathbf{k}'\mathbf{g}\neq 0} V_{\mathbf{g}}(2a^\dagger_{c\mathbf{k}+\mathbf{g}}a^\dagger_{v\mathbf{k}'-\mathbf{g}}a_{v\mathbf{k}'}a_{c\mathbf{k}} + a^\dagger_{v\mathbf{k}+\mathbf{g}}a^\dagger_{v\mathbf{k}'-\mathbf{g}}a_{v\mathbf{k}'}a_{v\mathbf{k}} + a^\dagger_{c\mathbf{k}+\mathbf{g}}a^\dagger_{c\mathbf{k}'-\mathbf{g}}a_{c\mathbf{k}'}a_{c\mathbf{k}}),$$

with $V_{\mathbf{g}} = q^2/V\epsilon_0\epsilon_s g^2$, where we have neglected terms that do not conserve the number of particles in each band as well as the interband exchange term (Fetter and Walecka, 2012). Those terms are of a short-range nature and are therefore often of minor importance. To obtain the contribution from the electron-electron interaction to the EOMs of the single-particle density matrices, we need the commutators of $a^\dagger_{b'\mathbf{k}'}a_{b\mathbf{k}}$ with H_{ee}. For the interband operator $a^\dagger_{v\mathbf{k}'}a_{c\mathbf{k}}$ this leads to

$$[a^\dagger_{v\mathbf{k}'}a_{c\mathbf{k}}, H_{ee}] = \sum_{\mathbf{k}_1,\mathbf{g}\neq 0} V_{\mathbf{g}}(a^\dagger_{v\mathbf{k}'}a^\dagger_{v\mathbf{k}_1+\mathbf{g}}a_{v\mathbf{k}_1}a_{c\mathbf{k}+\mathbf{g}} - a^\dagger_{v\mathbf{k}'+\mathbf{g}}a^\dagger_{c\mathbf{k}_1-\mathbf{g}}a_{c\mathbf{k}_1}a_{c\mathbf{k}} + a^\dagger_{v\mathbf{k}'}a^\dagger_{c\mathbf{k}_1+\mathbf{g}}a_{c\mathbf{k}_1}a_{c\mathbf{k}+\mathbf{g}} - a^\dagger_{v\mathbf{k}'+\mathbf{g}}a^\dagger_{v\mathbf{k}_1-\mathbf{g}}a_{v\mathbf{k}_1}a_{c\mathbf{k}}). \tag{62}$$

Analogous equations are obtained for the intraband operators.

When taking the expectation value of Eq. (62), we observe that we get expectation values of four operators. Thus, instead of our getting a closed set of EOMs, this constitutes the starting point of an infinite hierarchy of equations for expectation values of an increasing number of operators, much like the Bogoliubov-Born-Green-Kirkwood-Yvon hierarchy of statistical thermodynamics (Huang, 1963).

A variety of techniques have been developed to treat such many-body systems. In a correlation expansion approach (Rossi and Kuhn, 2002) [also called the cumulant or cluster expansion approach (Kira *et al.*, 1999; Florian *et al.*, 2013)], one starts again with the single-particle density matrices ρ_c, ρ_v, and ρ_{vc}. The expectation values of four operators appearing in their EOMs, which represent two-particle density

matrices, are then separated into a sum over all possible factorizations into single-particle density matrices and the rest containing two-particle correlations. The same factorization scheme is applied to higher-order density matrices, leading to correlations among an increasing number of particles. Setting up EOMs for these higher correlations leads to an infinite set of equations of motion that need to be truncated by an approximation in order to become closed.

On the lowest order, all correlations are neglected, which leads to the time-dependent Hartree-Fock approximation. When a spatially homogeneous system is again considered, only single-particle density matrices that are diagonal in $\mathbf{k}$ are nonzero. Reordering the operators in Eq. (62) such that the creation and annihilation operators in a factorization are next to each other leads to

$$\langle [a_{v\mathbf{k}}^{\dagger} a_{c\mathbf{k}}, H_{ee}] \rangle = -\sum_{\mathbf{g}\neq 0} V_{\mathbf{g}} [\rho_{vc,\mathbf{k}+\mathbf{g}} (\rho_{v,\mathbf{k}} - \rho_{c,\mathbf{k}}) - \rho_{vc,\mathbf{k}} (\rho_{v,\mathbf{k}+\mathbf{g}} - \rho_{c,\mathbf{k}+\mathbf{g}})]. \tag{63}$$

Note that the restriction of the summation to $\mathbf{g} \neq 0$ in Eq. (63), which reflects the total charge neutrality, eliminates all Hartree-type factorizations.

Adding the contributions from the electron-electron interaction to the OBEs (60) leads to the semiconductor Bloch equations (SBEs) (Lindberg and Koch, 1988). They have the same structure as the OBEs, but with renormalized energies and field couplings:

$$\frac{d}{dt}\rho_{c,\mathbf{k}} = -\frac{d}{dt}\rho_{v,\mathbf{k}} = -2\mathrm{Im}[\tilde{\Omega}_{\mathbf{k}}(t)\rho_{vc,\mathbf{k}}^{*}], \tag{64a}$$

$$\frac{d}{dt}\rho_{vc,\mathbf{k}} = -i\tilde{\omega}_{\mathbf{k}}\rho_{vc,\mathbf{k}} + i\tilde{\Omega}_{\mathbf{k}}(t)(\rho_{v,\mathbf{k}} - \rho_{c,\mathbf{k}}). \tag{64b}$$

The external light field is complemented with an internal field resulting from the interband term of the Coulomb interaction, leading to an effective Rabi frequency $\tilde{\Omega}_{\mathbf{k}}(t)$ according to

$$\hbar\tilde{\Omega}_{\mathbf{k}}(t) = \mathbf{d}_{cv} \cdot \mathbf{E}(t) + \sum_{\mathbf{g}\neq 0} V_{\mathbf{g}} \rho_{vc,\mathbf{k}+\mathbf{g}}. \tag{65}$$

The energies of the electrons in the valence and conduction bands are renormalized by the intraband Coulomb terms, leading to the effective transition frequency $\hbar\tilde{\omega}_{\mathbf{k}} = (\tilde{\varepsilon}_{c\mathbf{k}} - \tilde{\varepsilon}_{v\mathbf{k}})$. For the conduction-band states this leads to

$$\tilde{\varepsilon}_{c\mathbf{k}} = \varepsilon_{c\mathbf{k}} - \sum_{\mathbf{g}\neq 0} V_{\mathbf{g}} \rho_{c,\mathbf{k}+\mathbf{g}}. \tag{66}$$

For the valence-band states the derivation produces the analogous result. However, the single-particle energy usually is defined in such a way that it already includes the energy renormalization of the completely filled valence band. Therefore, only the missing electrons in the valence band, i.e., the holes, contribute to the renormalization, and we have

$$\tilde{\varepsilon}_{v\mathbf{k}} = \varepsilon_{v\mathbf{k}} + \sum_{\mathbf{g}\neq 0} V_{\mathbf{g}} (1 - \rho_{v,\mathbf{k}+\mathbf{g}}). \tag{67}$$

This result is indeed directly obtained if the calculations are performed in the electron-hole picture. The internal field gives rise to the appearance of exciton lines in the absorption spectrum, while the energy renormalizations lead to a density-dependent reduction of the band gap. In the linear response regime the occupations in the valence and conduction bands are replaced by their equilibrium values and Eq. (64b) can be written in the form of a Wannier equation driven by a homogeneous light field, reflecting the excitation of excitons with vanishing center-of-mass motion. In Sec. IV.A.2 the Wannier equation for the case of excitation of a bulk semiconductor by a Bessel-type OV is derived and we see that under these conditions excitons with a nonvanishing center-of-mass momentum are generated.

Going beyond the level of the SBEs and including correlation effects, either due to the Coulomb interaction or due to the electron-phonon interaction, one obtains scattering and dephasing contributions that lead to a redistribution of the carriers in the bands and a loss of interband coherence. Keeping correlations up to only a given level, one can solve the equations for these correlations numerically, which corresponds to a quantum kinetic description of the scattering and dephasing processes (Schilp, Kuhn, and Mahler, 1994). Alternatively, they can be formally solved by performing a Markov approximation, which leads to scattering contributions to the SBEs similar to those found in a Boltzmann equation (Rossi and Kuhn, 2002).

For inhomogeneous optical excitation, the vertical-transition approximation fails, and electron states with different initial and final quasimomenta are coupled; here off-diagonal variables such as $\rho_{c,\mathbf{k}'\mathbf{k}}(t)$, $\rho_{v,\mathbf{k}'\mathbf{k}}(t)$, and $\rho_{vc,\mathbf{k}'\mathbf{k}}(t)$ are relevant. The off-diagonal terms contain the information on the space dependence and the EOMs then also describe spatial transport phenomena. The factorization of the Coulomb contributions to the EOM [Eq. (62) and the corresponding equations for the intraband variables] now also involves Hartree-like factorizations describing the self-consistent electric field caused by the inhomogeneous charge distribution. While the spatial information is rather hidden in this nondiagonal momentum representation, a more intuitive interpretation is provided by a Wigner function representation in terms of functions $\rho_{c,\mathbf{K}}(\mathbf{r},t)$, $\rho_{v,\mathbf{K}}(\mathbf{r},t)$, and $\rho_{vc,\mathbf{K}}(\mathbf{r},t)$, where $\mathbf{K} = (1/2)(\mathbf{k}+\mathbf{k}')$ and the $\mathbf{r}$ dependence is obtained from a Fourier transformation with respect to $\mathbf{k}-\mathbf{k}'$ (Rossi and Kuhn, 2002). We return to the Wigner and other mixed momentum-position representations when discussing the excitation of a bulk semiconductor by OVs in Sec. IV.A.2. Nonlinear scattering and dephasing terms in the EOMs of single-particle density matrices for inhomogeneous systems have also been derived by employing Lindblad-type superoperators (Rosati *et al.*, 2014).

Another widely used approach to describe optically induced dynamics in many-body systems is based on nonequilibrium Green's functions (Haug and Jauho, 2008; Balzer and Bonitz, 2013). The main difference compared to density matrix-based approaches is the fact that the basic variables, the single-particle

Green's functions, are two-time functions. The theory was developed in the 1960s by Kadanoff and Baym (1962) and Keldysh (1964) as a generalization of the equilibrium Green's function approach. While in the equilibrium case a single type of Green's function contains the full information about the system, out of equilibrium in general four different functions are needed. The information on the dynamics of occupations and coherences is obtained from the "less" and "greater" Green's functions $G^<$ and $G^>$, respectively, while spectral information is provided by the retarded and advanced Green's functions G^r and G^a, respectively. For electrons in the general multiband system $G^<$ and G^r are defined as

$$G^<_{b\alpha,b'\alpha'}(t_1,t_2) = -i\langle a^\dagger_{b'\alpha'}(t_2)a_{b\alpha}(t_1)\rangle,$$
$$G^r_{b\alpha,b'\alpha'}(t_1,t_2) = -i\Theta(t_1-t_2)\langle[a_{b\alpha}(t_1),a^\dagger_{b'\alpha'}(t_2)]_+\rangle,$$

with $\Theta(x)$ denoting the Heaviside step function and $[\cdots,\cdots]_+$ the anticommutator. $G^>$ and G^a are defined analogously. On the level of time-dependent Hartree-Fock theory, this approach again leads for the equal time variables to the SBEs. Many-body effects like scattering and dephasing can then be described in terms of a generalized Dyson equation, which can be treated within a diagrammatic expansion using Feynman diagrams. Nonequilibrium Green's functions have been used to study the effects of OV pulses on the disordered surface of a topological insulator, as discussed in Sec. IV.A.3.d.

Yet another popular approach is the use of the Liouville–von Neumann equation (Rossi, 2011) for the dynamics of the density operators $\rho(t)$ by the equation $i\hbar d\rho/dt = -[\rho,H]$ (note the difference in sign compared to the Heisenberg equation of motion). Here expectation values result from $\langle\mathcal{O}\rangle(t) = \mathrm{Tr}[\mathcal{O}\rho(t)]$. This approach is particularly useful in the case of systems with a discrete spectrum, such as atoms or semiconductor nanostructures like quantum dots, interacting with a bath. Relaxation and dephasing processes are often described in terms of a Lindblad superoperator (Lindblad, 1976) acting on ρ, which leads to a nonunitary time evolution but preserves basic properties of the density operator like Hermiticity and positivity (Breuer and Petruccione, 2002). For important special cases (a prototypical example being the coupling of a semiconductor quantum dot to acoustic phonons), a numerically exact solution of the optically driven many-body problem can be obtained in the framework of a real-time path integral approach (Vagov *et al.*, 2011).

The experimental exploration of the crystal's excited states and their evolution is done with linear and nonlinear optical techniques (Shah, 1999; Axt and Kuhn, 2004; Lu and Fu, 2018; Kalt and Klingshirn, 2019; Shree *et al.*, 2021). In photoluminescence spectroscopy the sample is excited at a fixed high energy, and the resulting photons emitted by the electrons undergoing radiative decay are recorded as a function of frequency; in a variant of that, photoluminescence excitation, the system is excited at varying energies, and the resulting emission is measured at a fixed frequency. Nonlinear spectroscopic techniques (Cundiff, 2008; Boyd, 2020) rely on the fact that the polarization of the system responds to a strong electric field in nonlinear ways $P \propto \chi^{(n)}E^n$, with $\chi^{(n)}$ an nth-order susceptibility. They are more powerful than linear methods because they can probe a variety of processes, such as the decay of populations and dephasing of coherences. In a typical experiment a sequence of laser pulses is used to "pump" the crystal creating the out-of-equilibrium state and to "probe" the state of the system after some delay. Specific techniques are pump-probe spectroscopy, which measures the dynamics of populations generated by the pump beam, but also time-dependent energy shifts, intraband coherences, or a perturbed free-induction decay (Koch, Peyghambarian, and Lindberg, 1988; Joschko *et al.*, 1997; Krügel *et al.*, 2007), Faraday and Kerr rotation that measures the spin dynamics and spin decoherence (Kikkawa and Awschalom, 1999; Kugler *et al.*, 2011), and four-wave mixing as well as 2D spectroscopy (Cundiff and Mukamel, 2013), which, depending on the pulse sequence and the extraction of the signal, can measure both interband coherence and population dynamics and allows for the separation of homogeneous and inhomogeneous broadening (Honold *et al.*, 1988; Lindberg, Binder, and Koch, 1992; Koch *et al.*, 1993). Pump-probe and four-wave-mixing spectroscopy on bulk semiconductors using OV pulses is discussed in Sec. IV.A.2.

When it comes to measuring nanostructures, bulk techniques can probe only an ensemble of particles, missing important properties of individual particles that are blurred by inhomogeneous broadening. Single-nanostructure measurements are better suited for this task. One can use emission or extinction (absorption) spectroscopy (Chatterjee *et al.*, 2018). In the latter the extinction of light going through the nanostructure at different frequencies is measured, yielding a spectrum that reveals large portions of the energy level structure. In contrast, typically emission spectroscopy relies on the emission of light from the lowest excited energy states. In addition, pump-probe (Sotier *et al.*, 2009; Henzler *et al.*, 2021) or four-wave-mixing (Patton *et al.*, 2006; Wigger *et al.*, 2020) techniques are currently sensitive enough to be applied to single nanostructures.

In all the cases discussed thus far the coupling to light is used as an excitation and/or measurement tool with the goal to obtain information on the spectral and/or dynamical properties of the material system. In some situations, however, when the coupling is sufficiently strong, the light becomes part of the system and one can no longer separate the system and the light dynamics. Instead, the coupling of electronic excitations and light leads to the emergence of new quasiparticles, such as different types of polaritons. Prominent examples are exciton polaritons in semiconductor microcavities, which have been extensively studied in recent years (Weisbuch *et al.*, 1992; Deng, Haug, and Yamamoto, 2010; Kavokin *et al.*, 2017). Their generation and dynamics were modeled based on the Heisenberg equation of motion (Ciuti, Schwendimann, and Quattropani, 2001; Portolan *et al.*, 2008; Shelykh *et al.*, 2010; Quinteiro, Dmitruk, and Aligia, 2012; Vasilieva, Zingan, and Khadzhi, 2018), one-particle Green's functions (Citrin, 1994; Savona *et al.*, 1997, 1999; Quinteiro, Fernández-Rossier, and Piermarocchi, 2006; Quinteiro, 2008), and the Liouville equation (Quinteiro and Piermarocchi, 2005; Shelykh, Kavokin, and Malpuech, 2005). In addition, the Gross-Pitaevskii equation, the bosonic version of the Hartree-Fock equation, has been used for the quasibosonic polaritons to account for their interaction and the excitation by a source

field (Shelykh *et al.*, 2006; Gippius *et al.*, 2007; Liew and Shelykh, 2009).

In metallic nanostructures the light couples to the electron plasma. Close to surfaces of the metal or interfaces between the metal and a dielectric environment, this gives rise to the formation of surface plasmon polaritons, which are another example of quasiparticles that treat light and matter on an equal footing. Simple models of plasmonics combine the Drude model for electrons in metals and Maxwell's equations of electrodynamics (Maier, 2007). Here the Drude model provides a dielectric function for the response of the electron plasma in the metal to an external perturbation. This and the dielectric constant of the dielectric material are plugged into the Helmholtz equation for the propagation of the electromagnetic field; the solutions are the plasmon polaritons. For plasmon polaritons in the subwavelength scale, a quasistatic approximation for the fields can be used in a small metallic sphere surrounded by a dielectric. For larger particles for which the quasistatic approximation fails, one can resort to Mie theory (Mie, 1908). The imaging of plasmon polaritons can be done using different techniques, and near-field microscopy stands among them as a powerful one. In photon scanning tunneling microscopy a metallic tip is brought close to the surface so that it couples to the evanescent field; this makes the collection of photons out of the surface and their measurement possible (Maier, 2007).

IV. OPTICAL VORTICES MEET CONDENSED MATTER

About a decade ago, two independent works addressed the topic of the excitation of condensed-matter systems by OVs. One of them provided theoretical predictions (Quinteiro and Tamborenea, 2009c) and the other experimental results (Ueno *et al.*, 2009). The former predicted the generation of circular electric currents in bulk semiconductors, a new type of "circular photon-drag" effect. The latter demonstrated, using four-wave-mixing techniques, the transfer of OAM to excitons in GaN semiconductors. Since then, many groups have contributed to the advancement of the subject by investigating the interaction of OVs with bulk semiconductors, nanostructures, metals, metal-dielectric interfaces, microcavities, etc. In this section we review the basic tools to study the interaction of light beams having phase singularities with condensed-matter systems, and in so doing we report on what has been learned thus far about each system from theory and experiments.

A. Semiconductor optics and the silent assumptions

Two pervasive assumptions must be abandoned before theoretical progress and real understanding in OV-semiconductor physics can be made, and other assumptions must also be reexamined in the broader interface between condensed matter and OVs; see Table I. The first one is the vertical-transition approximation (Sec. III.C.2), in which the momentum of the photon is neglected, which eliminates from the start the most important effects of OV-semiconductor interactions, such as the generation of electric currents in bulk or the excitation of normally inaccessible states in quantum dots. The second one is the dipole-moment approximation (Sec. III.C.1) that assumes a constant electric field at the position of the matter system; if the system is localized at the optical phase singularity (intensity zero point), then the dipole-moment approximation fails completely to account for the interaction. We note that these two assumptions are related. They are most detrimental, and their reevaluation, as conducted earlier and in this and the following sections, shows that they can (and indeed must) be safely dropped. The reexamination of other well-entrenched (although not extremely harmful) assumptions widens our understanding of the topic and provides extra tools to model particular problems.

The dipolelike interaction Hamiltonian $h_I = -\mathbf{d}\cdot\mathbf{E}(\mathbf{r},t)$ with $\mathbf{d} = q\mathbf{r}$ has proven useful in treating the interaction of semiconductors with inhomogeneous fields, such as accounting for the transfer of linear momentum in exciton-polariton physics [see Khitrova *et al.* (1999), Appendix A.2]. However, Quinteiro, Reiter, and Kuhn (2015) recognized that the proper electric interaction Hamiltonian for parallel momenta OVs is different and must be derived by manner of a new twisted-light gauge transformation, leading to the interaction Hamiltonian $h_I = -[1/(\ell+1)]\mathbf{d}_\perp\cdot\mathbf{E}(\mathbf{r},t)$ for flat structures, which was further generalized to include the interaction with antiparallel

TABLE I. Silent assumptions based on quasihomogeneous beams (plane waves, Gaussian beams, etc.) mainly used in condensed-matter optics, and their applicability for describing the interaction with OVs.

	Silent Assumptions	
		Beams
Feature	Quasihomogeneous	Optical vortex
Coupling	Dipole moment or dipolelike electric interaction	Nondipole
k-space transition	Vertical	Tilted
Interaction field	**E**	**E** and **B**
Interaction with field component	Transverse	Transverse and longitudinal
Convenient representation	Plane waves	Bessel, LG, Mathieu, and other functions
Archetypical system	Bulk	Quantum ring
Effects on optical-to-structure axis displacement	Transition amplitudes	Transition amplitudes and selection rules

momenta OVs using the Poincaré gauge with interaction Hamiltonian $h_I = -\mathbf{d}\cdot\mathbf{E}^{\text{eff}}(\mathbf{r},t) - \mathbf{m}_B\cdot\mathbf{B}^{\text{eff}}(\mathbf{r},t)$, with $\mathbf{m}_B = -(q/2m)(\mathbf{p}\times\mathbf{r})$ and effective fields of the form $\mathbf{E}^{\text{eff}} = f_{\mathbf{E}\perp}(\ell)E_\perp(\mathbf{r},t) + f_{Ez}(\ell)E_z(\mathbf{r},t)$ and correspondingly for $\mathbf{B}^{\text{eff}}$ (Quinteiro, Reiter, and Kuhn, 2017b).

Bulk is the archetypical system to theoretically study the interaction of condensed matter with spatially uniform light (typified by plane waves), providing the simplest approach and the clearest results and interpretation. This is due mostly to the fact that both the envelope part of the Bloch electronic wave function and plane waves are usually treated in Cartesian coordinates. However, for OVs the situation is different: vortices are written most easily in cylindrical coordinates, and the analytical treatment of their interaction with bulk systems is thus cumbersome (Sec. IV.A.2).

Fourier analysis and plane waves are widespread tools for understanding wave optics and quantum mechanics, and it is easy to oversee that other bases are good representations as well. In fact, a light field with a single singularity is much more easily represented by a single Bessel or LG function.

The research on the effects produced by uniform light brings about another prejudice. Light at the optical frequencies predominantly interacts with matter via its electric field. However, some OVs present an especially intense magnetic field that makes the magnetic interaction dominant [consider Eq. (24b) for $\{\sigma = \pm 1, \ell = \mp 2, \gamma = 1\}$; for details see Quinteiro *et al.* (2019)].

The widespread use of plane waves may lead us to disregard the longitudinal component of the beam in the light-matter interaction. OVs present significant components in the direction of propagation; see Eqs. (24a) and (24b). The presence of a field component E_z does not contradict the transversality of the field, for each plane wave composing the beam is transverse to its propagation direction or, in other words, $\nabla\cdot\mathbf{E} = 0$ is satisfied (Sec. II.F).

Finally, the relative position of the vortex optical axis and nanostructure symmetry axis has a direct influence on optical selection rules, in stark contrast to the interaction with plane waves that presents no optical axis whatsoever, and their positioning with respect to the system is irrelevant. The subject of displaced optical axes brings about the topic of intrinsic and extrinsic AM, as discussed by Bliokh and Nori (2015).

1. Basics

Among several approaches to model the light-matter interaction, such as the Gross-Pitaevski equation for exciton polaritons in microcavities or nonequilibrium Green's functions, the method involving reduced density matrices has found the most widespread applications in the study of OV-semiconductor interactions. As anticipated in Sec. III.C.3, the basic variables are the intraband ($b = b'$) and interband ($b \neq b'$) single-particle density matrices $\rho_{b'\alpha',b\alpha}(t) = \langle a^\dagger_{b'\alpha'}(t)a_{b\alpha}(t)\rangle$, with the operators $a^\dagger_{b\alpha}$ ($a_{b\alpha}$) denoting the creation (annihilation) of an electron in the state $\psi_{b\alpha}$ [Eq. (52)] in the band b with envelope-function quantum number α. The equations of motion for $\rho_{b'\alpha',b\alpha}(t)$ are most conveniently obtained using the Heisenberg EOM for the operators. When many-body interactions, such as the Coulomb interaction or the electron-phonon interaction, are involved, higher-order density matrices involving more than one creation and one annihilation operator appear in the EOM of the single-particle density matrices, and the resulting hierarchy of equations has to be truncated at a certain level.

An essential building block is the matrix element of the light-matter interaction Hamiltonian h_I, which enters the derivation of the EOM through its second quantization form $H_I = \sum_{bb'\alpha\alpha'}\langle b'\alpha'|h_I|b\alpha\rangle a^\dagger_{b'\alpha'}a_{b\alpha}$. The matrix element is also featured in other common calculations, such as in Fermi's golden rule to calculate transition rates, as shown in Eq. (59) for the homogeneous case. In the following we first present the matrix element for an arbitrary basis and then present the EOM; in doing so we comment on the silent assumptions and their incompatibility with a sound description of OV-matter interactions.

We model a direct band-gap semiconductor with wave functions $\psi_{b\alpha}(\mathbf{r})$ that can represent either a Bloch state for bulk [see Eq. (41)] or the state of a nanostructure in the envelope-function approximation [see Eq. (52)] excited by an OV. Following the standard practice, only states close to the band edges (with the approximation for the microscopic wave function $u_{b\mathbf{k}} \to u_{b\mathbf{k}_0} \doteq u_b$, with $\mathbf{k}_0$ the wave vector at the corresponding band edge) are used, so $\psi_{b\alpha}(\mathbf{r}) = \mathcal{E}_{b\alpha}(\mathbf{r})u_b(\mathbf{r})$ [Eq. (52)]. For bulk, according to Bloch's theorem, the envelope function is given by a plane-wave $\mathcal{E}_{\mathbf{k}}(\mathbf{r}) = \exp(i\mathbf{k}\cdot\mathbf{r})/\sqrt{V}$ [Eq. (41)]. The electron spin (or in the presence of spin-orbit coupling the z component of the total angular momentum) can be included in either the band index b or the state index α. Since the interaction Hamiltonian depends only on spatial coordinates, the corresponding matrix elements are diagonal in spin, but not in the total angular momentum. Therefore, the interaction selects the spin and angular momentum projections that are excited [the so-called optical orientation Meier and Zakharchenya (2012)] through the polarization of light and the microscopic wave function u_b (Bastard, 1988). In Sec. IV.A.3 we return to the spin-orbit interaction and discuss this point in more detail.

The OV-matter interaction Hamiltonian in its general form reads [see Eq. (46)]

$$\begin{aligned} h_{\text{OV}} &= -\frac{q}{2m_0}[\mathbf{p}\cdot\mathbf{A}(\mathbf{r},t) + \mathbf{A}(\mathbf{r},t)\cdot\mathbf{p}] + q\Phi(\mathbf{r},t) \\ &= -\frac{q}{m_0}\mathbf{A}(\mathbf{r},t)\cdot\mathbf{p} + q\Phi'(\mathbf{r},t), \end{aligned} \tag{68}$$

with $\Phi'(\mathbf{r},t) = \Phi(\mathbf{r},t) - (\hbar/2m_0 i)[\nabla\cdot\mathbf{A}(\mathbf{r},t)]$ and the $\mathbf{A}^2$ term being neglected. Different gauges are considered in special cases, as they may require specific approximations (Sec. IV.A.3).

The matrix element is handled by recognizing that the periodicity in the unit cell [$u_b(\mathbf{r}+\mathbf{R}) = u_b(\mathbf{r})$] allows one to do an additional simplification (Haug and Koch, 2009). The integral over the entire crystal is separated into integrals over the unit cell and a summation over all the unit cells in the volume $V = Nv$, with v the volume of the unit cell and N the number of unit cells. Thus, with $\mathbf{r} \to \mathbf{x} + \mathbf{R}$ (see Fig. 7)

$$\langle b'\alpha'|h_{\mathrm{OV}}^{(\mathbf{A})}|b\alpha\rangle = \langle b'\alpha'|h_{\mathrm{OV}}^{(\mathbf{A}1)}|b\alpha\rangle + \langle b'\alpha'|h_{\mathrm{OV}}^{(\mathbf{A}2)}|b\alpha\rangle$$
$$= -\frac{q}{m_0} v \sum_{\mathbf{R}} \mathcal{E}^*_{b'\alpha'}(\mathbf{R})\mathbf{A}(\mathbf{R},t)\cdot\left[\mathcal{E}_{b\alpha}(\mathbf{R})\frac{1}{v}z\int_v d\mathbf{x}\, u^*_{b'}(\mathbf{x})\mathbf{p}u_b(\mathbf{x})\right.$$
$$\left. - i\hbar\boldsymbol{\nabla}\mathcal{E}_{b\alpha}(R)\frac{1}{v}\int_v d\mathbf{x}\, u^*_{b'}(\mathbf{x})u_b(\mathbf{x})\right], \tag{69a}$$

$$\langle b'\alpha'|h_{\mathrm{OV}}^{(\Phi)}|b\alpha\rangle = \langle b'\alpha'|h_{\mathrm{OV}}^{(\Phi 1)}|b\alpha\rangle + \langle b'\alpha'|h_{\mathrm{OV}}^{(\Phi 2)}|b\alpha\rangle$$
$$= qv\sum_{\mathbf{R}} \mathcal{E}^*_{b'\alpha'}(\mathbf{R})\mathcal{E}_{b\alpha}(\mathbf{R})\left[\boldsymbol{\nabla}\Phi'(\mathbf{R},t)\cdot\frac{1}{v}\int_v d\mathbf{x}\, u^*_{b'}(\mathbf{x})\mathbf{x}u_b(\mathbf{x})\right.$$
$$\left. + \Phi'(\mathbf{R},t)\frac{1}{v}\int_v d\mathbf{x}\, u^*_{b'}(\mathbf{x})u_b(\mathbf{x})\right]. \tag{69b}$$

Here we assume that the envelope functions and the potentials vary slowly over a unit cell and keep only the lowest orders. The two terms in Eq. (69a) arise from the action of the momentum operator $\mathbf{p} = -i\hbar\boldsymbol{\nabla}$ on the lattice-periodic part and the envelope part of the wave function, respectively, while the two terms in Eq. (69) reflect the lowest orders in the expansion of Φ'.

The microscopic wave functions $u_{b\mathbf{k}_0}$ at a fixed $\mathbf{k}_0$ form a complete orthonormal system in a unit cell; thus, $v^{-1}\int_v d\mathbf{x}\, u^*_{b'}(\mathbf{x})u_b(\mathbf{x}) = \delta_{bb'}$. Therefore, the second terms on the right-hand side of Eqs. (69a) and (69b) give rise to intraband processes. When $v\sum_{\mathbf{R}}$ is replaced by the integral $\int d\mathbf{R}$ over the entire system, these processes are described using the matrix elements

$$\langle b\alpha'|h_{\mathrm{OV}}^{(2)}|b\alpha\rangle = \int d\mathbf{R}\mathcal{E}^*_{b\alpha'}(\mathbf{R})\left[\frac{i\hbar q}{m_0}\mathbf{A}(\mathbf{R},t)\cdot\boldsymbol{\nabla}\right.$$
$$\left. + q\Phi'(\mathbf{R},t)\right]\mathcal{E}_{b\alpha}(\mathbf{R}). \tag{70}$$

If the microscopic wave functions u_b have a well-defined parity, the first terms on the right-hand side of Eqs. (69a) and (69b) give rise to purely interband processes because the operators $\mathbf{p}$ and $\mathbf{x}$ both have odd parity. In many typical semiconductors the parities of u_b are different in the valence band (v) and the conduction band (c); these terms then induce dipolar transitions between the valence and conduction bands. With $b' = c$ and $b = v$ and introducing the momentum and dipole matrix elements $\mathbf{p}_{cv} = v^{-1}\int_v d\mathbf{x}\, u^*_c(\mathbf{x})\mathbf{p}u_v(\mathbf{x})$ and $\mathbf{d}_{cv} = qv^{-1}\int_v d\mathbf{x}\, u^*_c(\mathbf{x})\mathbf{x}u_v(\mathbf{x})$ [see Eq. (57)], respectively, we obtain for the interband-transition matrix element

$$\langle c\alpha'|h_{\mathrm{OV}}^{(1)}|v\alpha\rangle = \int d\mathbf{R}\,\mathcal{E}^*_{c\alpha'}(\mathbf{R})\left[-\frac{q}{m_0}\mathbf{A}(\mathbf{R},t)\cdot\mathbf{p}_{cv}\right.$$
$$\left. + \boldsymbol{\nabla}\Phi'(\mathbf{R},t)\cdot\mathbf{d}_{cv}\right]\mathcal{E}_{v\alpha}(\mathbf{R}). \tag{71}$$

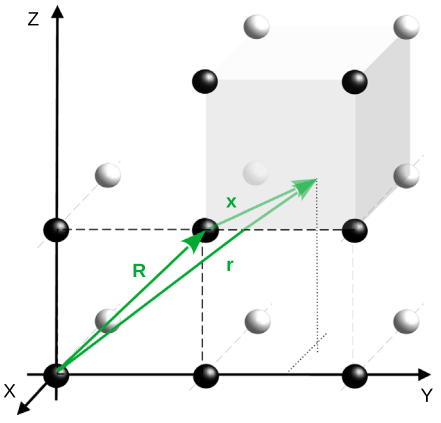

FIG. 7. Representation of a crystal with the change of variables to calculate the interaction Hamiltonian matrix element $\mathbf{r} \to \mathbf{x} + \mathbf{R}$, in which $\mathbf{R}$ points to unit cells and $\mathbf{x}$ maps the points within a unit cell.

Assuming a bulk semiconductor with plane-wave envelope functions and a spatially homogeneous electric field $\mathbf{E}(t)$, we recover the vertical-transition approximation, either in the Coulomb gauge with $\mathbf{A}(t) = -\int_{t_0}^t \mathbf{E}(t')dt'$ and $\Phi = 0$ or in the dipole (Göppert-Mayer) gauge with $\mathbf{A} = 0$ and $\Phi' = \Phi = -\mathbf{r}\cdot\mathbf{E}(t)$, which leads to $\boldsymbol{\nabla}\Phi'(\mathbf{R},t) = -\mathbf{E}(t)$ (Sec. III.C.3). In some semiconductors, with a prototype being cuprous oxide (Cu_2O), the parities of the valence- and conduction-band states at the band extrema are the same. In this case one has to take into account the linear order in $\mathbf{k}$ in the expansion of the microscopic wave functions $u_{b\mathbf{k}}$ around the band extrema, which leads to weaker, so-called second class transitions (Elliott, 1957; Nikitine, 1969).

The rotating wave approximation (RWA) further simplifies the coupling Hamiltonian. Recalling that all fields are real quantities, we separate the potentials into the positive and negative frequency components $\mathbf{A} = \mathbf{A}^{(+)} + \mathbf{A}^{(-)}$, with $\mathbf{A}^{(\pm)} \propto \exp(\mp i\omega t)$, and proceed correspondingly for Φ. The RWA stipulates that in a frame rotating with the light field only slowly varying terms are to be retained. For a light field resonant or near resonant to an interband transition $\mathbf{A}^{(+)}$ and $\Phi^{(+)}$ ($\mathbf{A}^{(-)}$ and $\Phi^{(-)}$) account for the absorption (emission) of light by the material system. On the other hand, a matrix element $\langle b'\alpha'|h_{\mathrm{OV}}|b\alpha\rangle$ implies the transition $b\alpha \to b'\alpha'$. Therefore, matrix elements compatible with the RWA are (i) a transition from the valence band to the conduction band induced by $A^{(+)}$, (ii) a transition from the

conduction band to the valence band induced by $A^{(-)}$ (Scully and Zubairy, 1997; Cohen-Tannoudji, Dupont-Roc, and Grynberg, 1998). For light fields in the optical frequency range, intraband terms are far off resonant and are therefore neglected in the RWA. They are usually important if there is (either alone or in addition to the optical field) a static or low-frequency electromagnetic field leading to intraband transport terms (Rossi and Kuhn, 2002) or phenomena like the static or dynamical Franz-Keldysh effect (Franz, 1958; Keldysh, 1958; Jauho and Johnsen, 1996). Furthermore, they become important in the case of strongly off-resonant or extremely strong light fields, where the RWA is not applicable, such as when dealing with two-photon transitions (Duc, Meier, and Koch, 2005) or high-harmonics generation (Golde, Meier, and Koch, 2008). If not explicitly otherwise stated, in the following we assume that the RWA is applicable and we neglect the intraband matrix elements $h^{(2)}_{\mathrm{OV}}$.

To describe the interaction with OVs, one has to depart from traditional semiconductor optics by keeping the spatial structure of the beam at the level of the entire system in Eq. (71).[10] From a different standpoint, one is abandoning the vertical-transition and dipole-moment approximations, at least in their most strict senses. A strict dipole-moment approximation requires a spatially uniform vector potential $\mathbf{A}$ and a scalar potential Φ linear in $\mathbf{r}$, that bring the integrals in the case of bulk Bloch functions, where α corresponds to the wave vector $\mathbf{k}$, into $\delta_{\mathbf{k}\mathbf{k}'}$ or, in the case of angular momentum eigenstates, where α comprises an angular momentum quantum number m, into a $\delta_{mm'}$. In contrast to smooth fields, OVs have a spatial structure that strongly varies on the scale of the semiconductor. For example, a monochromatic Bessel beam with angular frequency ω, single topological charge ℓ, and polarization σ for general γ [Eq. (23)] reads

$$\tilde{\mathbf{A}}(\mathbf{r},t) = A_0 J_\ell(q_r r) e^{i\ell\varphi}\mathbf{e}_\sigma - i\gamma\sigma\frac{q_r}{q_z}\frac{A_0}{\sqrt{2}} J_{\ell+\sigma}(q_r r) e^{i(\ell+\sigma)\varphi}\mathbf{e}_z, \tag{72a}$$

$$\tilde{\Phi}(\mathbf{r},t) = i(1-\gamma)\sigma\frac{c^2}{\omega}\frac{A_0}{\sqrt{2}} q_r J_{\ell+\sigma}(q_r r) e^{i(\ell+\sigma)\varphi}, \tag{72b}$$

with amplitude A_0. The space dependence of the potentials precludes the simplification of Eq. (71), leading to vertical transitions in $\mathbf{k}$ or m or, more generally, diagonal transitions in α. Note that the dipole-moment approximation at the level of the microscopic wave function is, however, retained; therefore, multipolar transitions are possible only between envelope states; for further discussion see Sec. VI.B.3.

Using the interband matrix elements of the interaction Hamiltonian according to Eq. (71), we can now specify the general EOM (56) to the two-band case, leading to

$$i\hbar\frac{d}{dt}\rho_{vc,\alpha\alpha'} = \Delta_{c\alpha',v\alpha}\rho_{vc,\alpha\alpha'} + \sum_\beta(\langle c\alpha'|h^{(1)}_{\mathrm{OV}}|v\beta\rangle\rho_{v,\alpha\beta} - \langle c\beta|h^{(1)}_{\mathrm{OV}}|v\alpha\rangle\rho_{c,\beta\alpha'}), \tag{73a}$$

$$i\hbar\frac{d}{dt}\rho_{v,\alpha\alpha'} = \Delta_{v,\alpha'\alpha}\rho_{v,\alpha\alpha'} + \sum_\beta(\langle v\alpha'|h^{(1)}_{\mathrm{OV}}|c\beta\rangle\rho_{vc,\alpha\beta} - \langle c\beta|h^{(1)}_{\mathrm{OV}}|v\alpha\rangle\rho_{cv,\beta\alpha'}), \tag{73b}$$

$$i\hbar\frac{d}{dt}\rho_{c,\alpha\alpha'} = \Delta_{c,\alpha'\alpha}\rho_{c,\alpha\alpha'} + \sum_\beta(\langle c\alpha'|h^{(1)}_{\mathrm{OV}}|v\beta\rangle\rho_{cv,\alpha\beta} - \langle v\beta|h^{(1)}_{\mathrm{OV}}|c\alpha\rangle\rho_{vc,\beta\alpha'}), \tag{73c}$$

with $\Delta_{c\alpha',v\alpha} = \varepsilon_{c\alpha'} - \varepsilon_{v\alpha}$, and $\Delta_{b,\alpha'\alpha} = (\varepsilon_{b\alpha'} - \varepsilon_{b\alpha})$ for $b \in \{c, v\}$. The contributions of the Coulomb interaction are not included here. As discussed in Sec. III.C.3, they involve two-particle density matrices (i.e., expectation values of four operators) that after factorization give rise to renormalizations of energies and light field similar to the homogeneous bulk case [Eq. (64)]. In Sec. IV.A.2 the Coulomb term is considered during a discussion of excitonic effects associated with the excitation of bulk semiconductors by an OV.

In the case of a homogeneous bulk semiconductor, the single-particle density matrices are diagonal in $\mathbf{k}$. With the interaction matrix elements for a homogeneous electric field, Eqs. (73a)–(73c) immediately reduce to Eqs. (60a) and (60b), thereby implying vertical transitions.

In general, however, owing to the nondiagonal character of the interaction matrix elements even a density matrix that is initially diagonal in α will not remain diagonal over the course of time. Assuming at a given time the single-particle density matrices to be diagonal in α, according to the EOM (73) in the next time step the density matrix elements with all combinations $(\alpha\alpha')$, for which also the interband matrix element $\langle c\alpha'|h^{(1)}_{\mathrm{OV}}|v\alpha\rangle$ is nonzero, will be nonzero.

Owing to the lack of a diagonal (or vertical) nature of the light-induced transitions, the EOMs are considerably more complicated than Eqs. (60a) and (60b) for the homogeneous bulk system, for they couple in principle all possible values of the quantum number α in each band, even without taking into account the many-body effects. If one is not interested only in the carrier generation process itself, typically the EOMs have to be complemented by some relaxation terms. In the simplest case one can simply include phenomenological interband and intraband relaxation times. A more microscopic description of scattering, relaxation, and recombination processes can be

[10]This is not to be confused with a "parametrical" dependence, in which $\mathbf{R}$ is a constant indicating the position of a nanostructure and no integration is performed on $\mathbf{R}$.

obtained by adding Boltzmann-like scattering terms, which can be formally derived using a correlation expansion of the terms induced by the coupling of the electrons to phonons, to other electrons, or to the photon vacuum (Rossi and Kuhn, 2002).

Besides a full numerical solution of the system of equations involving a suitable restriction of the set of quantum numbers or a suitable discretization in the case of (quasi)continuous quantum numbers, general approaches to solve this system of equations under specific conditions exist and provide further insight into the optical properties and dynamics induced by the excitation with OVs. Under low-excitation conditions, a perturbative, iterative approach in terms of the amplitude of the driving field (or its potentials) provides approximate solutions for interband and intraband density matrices for a system initially in its electronic ground state. To lowest order, i.e., without electromagnetic fields, the only nonzero matrix elements are the valence-band populations $\rho^{(0)}_{v,\alpha\alpha'}=\delta_{\alpha\alpha'}$, while $\rho^{(0)}_{c,\alpha\alpha'}=\rho^{(0)}_{vc,\alpha\alpha'}=0$ (the superscript indicates the order). The only nonzero source term then appears in interband coherences $\rho_{vc,\alpha\alpha'}$; thus, the lowest-order interband coherence $\rho^{(1)}_{vc,\alpha\alpha'}$ is linear in the driving amplitude A_0; see Eq. (72). This in turn induces a second-order term in the intraband coherences and occupations. Following this iterative process, it is seen that interband (intraband) coherences come only in odd (even) powers of the amplitude. Keeping in mind that the interband density matrix elements oscillate with the frequency of the band gap while the intraband coherences oscillate with frequencies corresponding to energy differences in the bands, the transfer of OAM from light to electrons can thus be separated into fast (odd) and slow (even) contributions. However, this separation into fast and slow variables is possible only if the RWA is applicable. Non-RWA contributions in the interband matrix elements of the interaction Hamiltonian lead to additional fast contributions in the intraband density matrices. When intraband matrix elements according to Eq. (70) are included, interband and intraband coherences as well as occupations appear in all orders of the field.

A different approach based on a quasiequilibrium approximation relies on the difference in timescales of scattering-induced relaxation and light-induced excitation processes. For sufficiently strong scattering the intraband populations can be approximated by quasiequilibrium distributions with a given temperature and chemical potential, allowing for a solution of the interband coherence that feeds slowly varying EOMs for intraband coherences or populations (Chow and Koch, 1999). In this way, absorption spectra of highly excited semiconductors can be obtained.

2. Bulk

Bloch states are the natural representation of electrons in a bulk crystal; although not especially well suited to describe the interaction with OVs, they still shed light on interesting features that complement those learned from a representation of electrons in cylindrical states and connect well to what we learned about the modal decomposition of OVs in Sec. II.F.

In semiconductor optics, one is concerned mostly with interband processes, in which an electron undergoes transitions between the valence and conduction bands, separated from each other by the band gap E_g. The transition is induced by resonant or nearly resonant light $\hbar\omega\simeq E_g$. The simplest theoretical model is that of a two-band semiconductor excited by a monochromatic single-singularity OV. Working in the Coulomb and radiation gauge, the scalar potential vanishes and the relevant light-matter interaction matrix element [Eq. (71)] between the Bloch states $\psi_{b\alpha}(\mathbf{r})=\exp(i\mathbf{k}\cdot\mathbf{r})u_b(\mathbf{r})/\sqrt{V}$ is given by

$$\langle c\mathbf{k}'|h^{(1)}_{\mathrm{OV}}|v\mathbf{k}\rangle=-\frac{q}{m_0}\mathbf{p}_{cv}\cdot\frac{1}{V}\int d\mathbf{R}\,e^{-i(\mathbf{k}'-\mathbf{k})\cdot\mathbf{R}}\mathbf{A}(\mathbf{R},t).$$

That is, it involves the Fourier transform of the beam profile. Irrespective of the particular form of the single-singularity OV being considered (see Sec. II.C), the vector potential has in the component j the form

$$A_j(\mathbf{r},t)=A_{0j}(r)e^{in_j\varphi}e^{i(q_zz-\omega t)}+\mathrm{c.c.},\tag{74}$$

with $n_j=\ell,\ell+\sigma,\ldots$ and $A_{0j}(r)$ the space- and n_j-dependent amplitude. We handle the calculation of the matrix elements in the following way. Because of the symmetry of the light field we use a normalization volume of the Bloch functions in the form of a cylinder with radius R_0 and height L. We split the integral into one in-plane integral and one in the z direction and use the vectors $\boldsymbol{\kappa}=\mathbf{k}'-\mathbf{k}$ and $\mathbf{R}$ in the cylindrical coordinates $\{\kappa_r,\varphi_\kappa,\kappa_z\}$ and $\{R,\varphi,Z\}$, respectively, leading to $\boldsymbol{\kappa}\cdot\mathbf{R}=\kappa_rR\cos(\varphi_\kappa-\varphi)+\kappa_zZ$; see Eq. (33). The z integral simply reduces to $\int dZ\,e^{i(q_z-\kappa_z)z}=L\delta_{q_z,\kappa_z}$. To simplify the in-plane integral, we introduce the Jacobi-Anger identity $e^{iu\cos\eta}=\sum_t i^tJ_t(u)e^{i\eta t}$ (Korenev, 2002); compare this to Eq. (36). The resulting matrix element is

$$\langle c\mathbf{k}'|h^{(1)}_{\mathrm{OV}}|v\mathbf{k}\rangle|_j=-\frac{q}{m_0}p_{cv,j}(-i)^{n_j}\delta_{q_z,\kappa_z}e^{-i\omega t}e^{in_j\varphi_\kappa}\times\frac{2}{R_0^2}\int dR\,RJ_{n_j}(\kappa_rR)A_{0j}(R),$$

where we have taken into account the fact that due to the RWA only the positive frequency component $\mathbf{A}^{(+)}$ of the potential contributes to the matrix element describing a transition from the valence band to the conduction band.

A simplification of the last integral is possible if we specify the radial profile of the beam. If the beam profile is of the Bessel type $[A_{0j}(R)=A_{0j}J_{n_j}(q_rR)]$, we use the orthogonality $\int_0^\infty RJ_\alpha(\kappa_rR)J_\alpha(q_rR)dR=\delta(\kappa_r-q_r)/q_r$ and replace the delta function $\delta(q_r-\kappa_r)$ with $(R_0/\pi)\delta_{q_r,\kappa_r}$, which is appropriate for the cylindrical normalization volume with radius R_0. The contribution of the jth component of the vector potential to the matrix element then reads

$$\langle c\mathbf{k}'|h^{(1)}_{\mathrm{OV}}|v\mathbf{k}\rangle|_j=-(-i)^{n_j}p_{cv,j}A_{0j}\frac{2q}{\pi m_0q_rR_0}\times\delta_{q_r,\kappa_r}\delta_{q_z,\kappa_z}e^{in_j\varphi_\kappa}e^{-i\omega t}.\tag{75}$$

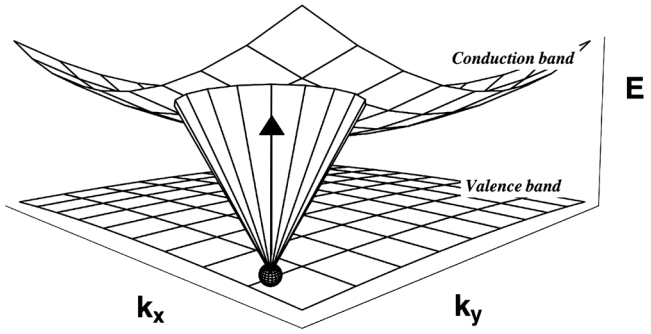

FIG. 8. Representation of the electronic excitation of a bulk semiconductor in the Bloch electron representation. An electron in the valence band is promoted to a superposition state in the conduction band. From Quinteiro and Tamborenea, 2009c.

The factor δ_{q_z,κ_z} imposes conservation of the linear momentum in the z direction, while the factor δ_{q_r,κ_r} fixes the in-plane distance of the vectors $\mathbf{k}'$ and $\mathbf{k}$. However, there is no explicit expression signaling the conservation of OAM, which is due to the fact that Bloch states are not eigenstates of the angular momentum operator.

We can get additional insight by looking at the infinitesimal time evolution of an electron initially in the Bloch state $\psi_{v\mathbf{k}}(\mathbf{r})$. Realizing that the evolution operator for a single-particle state in the interaction picture for short times δt is given by $U = 1 - (i\delta t/\hbar)h_{\mathrm{OV}}$ leads one to $\psi(\mathbf{r},\delta t) = \psi(\mathbf{r},0) - (i\delta t/\hbar)\delta\psi(\mathbf{r})$. Initially assuming an electron in the Bloch state $\psi_{v\mathbf{k}}(\mathbf{r})$, we obtain

$$\begin{aligned}\delta\psi(\mathbf{r}) &= \sum_{\mathbf{k}'}\psi_{c\mathbf{k}'}\langle c\mathbf{k}'|h^{(1)}_{\mathrm{OV}}|v\mathbf{k}\rangle \\ &= -\frac{2q}{\pi m_0 q_r R_0}e^{-i\omega\delta t}\sum_j(-i)^{n_j}p_{cv,j}A_{0j} \\ &\quad\times\int d\varphi_\kappa e^{in_j\varphi_\kappa}\psi_{c\mathbf{k}+\bar{\boldsymbol{\kappa}}}(\mathbf{r}) \\ &= f(\mathbf{r})\psi_{c\mathbf{k}}(\mathbf{r}),\end{aligned} \tag{76}$$

in which the action of δ_{κ,q_r} and δ_{q_z,κ_z} has been incorporated by defining $\bar{\boldsymbol{\kappa}} = (q_r,\varphi_\kappa,q_z)$. The second form stresses the fact that the new wave function is not an eigenstate of the crystal Hamiltonian (Quinteiro and Tamborenea, 2009c). Pictorially, the excitation looks like a cone in momentum space with a fixed aperture q_r; see Fig. 8. The final superposition is formed by states lying on the curve resulting from the intersection of the cone and the conduction band, with each state having a particular phase $\exp(in_j\varphi_\kappa)$. The existence of a conelike excitation is not surprising: According to Sec. II.F the OV can be decomposed into a superposition of plane waves with wave vectors lying on the surface of a cone and varying phases. In the picture of plane waves, each component induces a one-k-state-to-one-k-state electronic transition, with conservation of its linear momentum; the entire excitation is, however, one k state to a superposition of many k states.

The expectation value of the OAM picked by electrons and the concomitant electric-current density $\mathbf{j} = (q\hbar/m_0)\mathrm{Im}[\psi^*\nabla\psi] - (q^2/m_0)\mathrm{Re}[\psi^*\mathbf{A}\psi]$ can be studied in

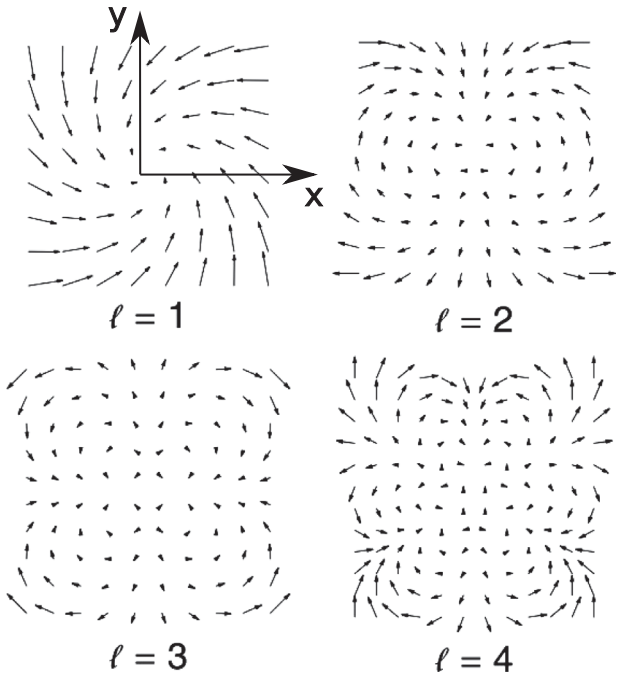

FIG. 9. First-order electric current in bulk for $\ell = 1,\ldots,4$ and the fixed polarization $\sigma = -1$. The current cycles in time and z following the electric field, as shown in Fig. 2. From Quinteiro and Tamborenea, 2009c.

powers of A_0 (Quinteiro and Tamborenea, 2009a). The first-order ($\propto A_0^1$) current is of microscopic origin and analogous to the optical polarization induced by plane waves. The vector potential imprints its spatial and temporal pattern onto the electronic state (see Fig. 9), and a net circulation of around $r = 0$ is observed only for $\{\ell = \pm 1, \sigma = \mp 1\}$, but with a zero time average. The second-order ($\propto A_0^2$) current is macroscopic and produces a net circulation with a nonzero average. The circular electric current generated by OVs in a semiconductor represents a new example of photon-drag effects that has recently been observed in experiments (Ge, 2020; Ji *et al.*, 2020).

Extensions to the previously explained simple model have been done thus far in two directions. On the one hand, a model still without electron-electron interactions was used to predict electronic transitions, OAM transfer, and electric currents using a more suitable representation of electrons by envelope states factorizing in cylindrical coordinates instead of the plane-wave envelope of Bloch states (Quinteiro and Tamborenea, 2010). On the other hand, the EOMs relevant to excitons and derived quantities were deduced using Bloch states and including electron-electron interactions (Quinteiro, 2010).

The symmetry mismatch between OVs and Bloch states led to a complex model of the optical excitation in bulk that ultimately required the transformation of Bloch states into a cylindrical representation using the Jacobi-Anger identity. One can directly face the OV-bulk problem instead using cylindrical coordinates. For a large system and in the presence of the envelope-function approximation, bulk properties are independent of the chosen boundary, whether it be a cubic box or a cylinder. Since the optical excitation takes place at the band edges, the envelope-function approximation is applicable and one can describe electron states using [see also Eq. (52)]

$$\psi_{b\mathbf{k}m}(r) = NJ_m(k_r r)e^{im\varphi}e^{ik_z z}u_b(\mathbf{r}),$$

which is defined inside a large cylinder of height L, radius R_0, quasimomenta k_z, k_r, and OAM $\hbar m$. The electron wave function with the normalization constant N is expressed by the cylindrical coordinates $\{r, \varphi, z\}$ (Quinteiro and Tamborenea, 2010). From the strong similarities between the representation of a typical single-singularity OV [Eq. (72)] and electron states in a cylinder, we foresee that the light-matter matrix element will be simpler than in the case of Bloch states based on plane waves. The interband matrix element with vector potential according to Eq. (74) having $A_{0j}(r) = A_{0j}J_{n_j}(q_r r)$ reads in the basis of the cylinder functions

$$\begin{aligned}\langle c, k_r', m', k_z'|h_{\mathrm{OV}}^{(1)}|v, k_r, m, k_z\rangle &= -\frac{q}{m_0}p_{cv,j}A_{0j}NN'\delta_{k_z',k_z+q_z}\delta_{m',m+n_j} \\ &\times \int dR\, RJ_{m'}(k_r'R)J_{n_j}(q_rR)J_m(k_rR). \end{aligned} \tag{77}$$

In fact, when the final values m' and k_z' are fixed, the matrix element reflects the conservation of the orbital quantum number m and the linear quasimomentum k_z, and only the radial quantum numbers k_r' and k_r are coupled by an integral over the Bessel functions of the beam and the initial and final electron states. We thus obtain a complementary situation compared to the calculation in the Bloch state basis. Whereas there the transfer in the radial component of the Bloch wave vector κ_r was fixed while the angle was continuous, now the change of the angle dependence, characterized by the quantum numbers m' and m, is fixed and the radial quantum number in the Bessel function changes continuously.

It is instructive to look at the lowest-order results of interband and intraband variables obtained for a monochromatic Bessel beam. When one assumes a sufficiently small paraxiality parameter q_r/q_z, the longitudinal field component can be neglected, and we assume a transverse vector potential amplitude $\mathbf{A}_0$ and a beam with a given topological charge ℓ. The zeroth order is given by a completely filled valence band, i.e., $\rho_{v,\alpha\alpha'}^{(0)} = \delta_{\alpha\alpha'}$ with $\alpha = (k_r, m, k_z)$, and all other density matrices vanish.

At first order we obtain from Eqs. (73a)–(73c) an interband coherence according to

$$\rho_{vc,\alpha\alpha'}^{(1)} = -\langle c\alpha'|h_{\mathrm{OV}}^{(1)}|v\alpha\rangle\frac{1-e^{-i(\varepsilon_{c\alpha'}-\varepsilon_{v\alpha}-\hbar\omega)t/\hbar}}{\varepsilon_{c\alpha'}-\varepsilon_{v\alpha}-\hbar\omega}. \tag{78}$$

Inserting the matrix element from Eq. (77), we thus find that the OV excites interband coherences with $m' - m = \ell$, $k_z' - k_z = q_z$, and in general arbitrary k_r' and k_r.

At second order Eqs. (73a)–(73c) give rise to intraband coherences and, as a special case, the populations in the conduction band and the valence band. For the populations of the conduction-band states, one gets

$$\rho_{c,\alpha'\alpha'}^{(2)} = 4\sum_{\alpha}\frac{|\langle c\alpha'|h_{\mathrm{OV}}^{(1)}|v\alpha\rangle|^2}{(\varepsilon_{c\alpha'}-\varepsilon_{v\alpha}-\hbar\omega)^2} \times \sin^2\left(\frac{(\varepsilon_{c\alpha'}-\varepsilon_{v\alpha}-\hbar\omega)t}{2\hbar}\right). \tag{79}$$

While the populations start to grow quadratically in t, for longer times the growth is linear, with the growth rate given by Fermi's golden rule, as expected for transitions in a continuous spectrum.

Important observables that one can calculate from the coherence are the OAM and the electric current in the electronic system. Gauge invariance imposes the need to appropriately express the quantities for which expectation values are to be calculated. In the Coulomb gauge, as is the case here, the OAM and electric current depend on the mechanical momentum of electrons $\mathbf{p} - q\mathbf{A}$; the first (second) term gives rise to the so-called paramagnetic (diamagnetic) contributions. A detailed calculation of the OAM and electric current was done by Quinteiro and Tamborenea (2010). The results, which are in agreement with those from the simple model for Bloch states, show that the interband coherence produces a fast oscillation of the OAM and a current with zero average, while the occupations and intraband coherences induce a permanent transfer of the OAM from the light to the electrons that generate a slow electric current with a nonzero mean value. The latter can be seen as the consequence of tilted transitions when one plots the energies of the valence- and conduction-band states versus their angular momentum quantum number m, a feature that is later discussed in more detail in the context of the excitation of quantum rings (Sec. IV.A.3.a). Note that the OAM associated with the beam is also proportional to the square of the field amplitude, as seen in Eq. (1).

Yet another extension to the simple single-particle bulk model is the inclusion of the Coulomb interaction, which allows for the description of excitons. Excitonic effects are important for a correct description of a light-matter interaction close to the band edge, particularly at low excitation densities, because they qualitatively modify the absorption spectrum leading to discrete lines below the band-to-band continuum. In fact, excitonic effects already appear at the lowest order in the field amplitude, i.e., when one considers the EOM for the interband coherence alone (Haug and Koch, 2009). Quinteiro (2010) considered the excitation of a bulk semiconductor with two energy bands by a monochromatic and transverse OV in a Bloch state representation. The nonvertical nature of optical transitions induced by OVs makes it convenient to work in a mixed representation of momentum and space coordinates, in analogy with the general approach based on Wigner functions discussed by Rossi and Kuhn (2002).

The derivation of the contributions to the EOM of the single-particle density matrix elements due to the electron-electron interaction Hamiltonian [Eq. (62)] was discussed in Sec. III.C.3, and the results on the level of the time-dependent Hartree-Fock theory was given for the case of a homogeneous two-band semiconductor in Eqs. (64)–(67). The excitation by an inhomogeneous light field, particularly by an OV, leads to inhomogeneous excitations, which are described by nondiagonal density matrices $\rho_{vc,\mathbf{kk}'}$, $\rho_{v,\mathbf{kk}'}$, and $\rho_{c,\mathbf{kk}'}$. The derivation of

the EOM proceeds in the same way as for a homogeneous system, only in the factorization of four-operator terms as in Eq. (63) off-diagonal terms also have to be kept. This has two consequences: (i) The renormalizations of the field and the energies [see Eqs. (65)–(67)] become nondiagonal in $\mathbf{k}$ and $\mathbf{k}'$ and (ii) the renormalizations of the energies get additional contributions from Hartree terms, which vanish in the homogeneous case due to charge neutrality. The full off-diagonal terms (in an electron-hole representation) were given by Rossi and Kuhn (2002). Here we restrict ourselves to the lowest order, i.e., to the linear response of the semiconductor to the excitation with an OV.

From the previous discussion we recall that interband density matrices appear in odd orders of the field and intraband density matrices in even orders. Restricting ourselves to the linear order therefore implies setting $\rho_{v,\mathbf{k}\mathbf{k}'} = \delta_{\mathbf{k}\mathbf{k}'}$ and $\rho_{c,\mathbf{k}\mathbf{k}'} = 0$. Since the renormalizations of the energies are caused by deviations of the intraband density matrices from their equilibrium value, they do not contribute to the first-order response. The equation of motion for the interband density matrix then reads

$$i\hbar\frac{d}{dt}\rho_{vc,\mathbf{k}\mathbf{k}'} = \Delta_{c\mathbf{k}',v\mathbf{k}}\rho_{vc,\mathbf{k}\mathbf{k}'} + \langle c\mathbf{k}'|h_{\mathrm{OV}}|v\mathbf{k}\rangle - \sum_{\mathbf{g}\neq 0} V_{\mathbf{g}}\rho_{vc,\mathbf{k}-\mathbf{g}\mathbf{k}'-\mathbf{g}}, \tag{80}$$

with $\Delta_{c\mathbf{k}',v\mathbf{k}} = \varepsilon_{c\mathbf{k}'} - \varepsilon_{v,\mathbf{k}}$.

The evolution of the coherence is driven by the OV-matter matrix element [Eq. (75)], which in the case of excitation by a Bessel beam can be translated into a nonvanishing matrix element $\langle c\mathbf{k}+\bar{\boldsymbol{\kappa}}|h_{\mathrm{OV}}|v\mathbf{k}\rangle$, with $\bar{\boldsymbol{\kappa}} = q_r\cos\varphi_\kappa\hat{\mathbf{x}} + q_r\sin\varphi_\kappa\hat{\mathbf{y}} + q_z\hat{\mathbf{z}}$, in which q_r and q_z are fixed by the corresponding parameters of the beam and φ_κ is variable. Once again we find the connection to the modal decomposition and the solution of the bulk problem in Bloch states: the matrix element gives rise to a nonvanishing contribution for each plane wave on a cone.

Instead of using a nondiagonal $\mathbf{k}$ representation of the density matrix elements, it can be useful to employ various types of mixed $(\mathbf{k},\mathbf{r})$ representations. The starting point is typically a transformation from the wave vectors $\mathbf{k},\mathbf{k}'$ to some relative and center-of-mass wave vectors according to $\mathbf{k} = \mathbf{K} - \eta\boldsymbol{\kappa}$ and $\mathbf{k}' = \mathbf{K} + \eta'\boldsymbol{\kappa}$, with $\eta + \eta' = 1$. A spatial variable is then obtained by Fourier transformation with respect to one of the wave vectors. Choosing $\eta = \eta' = 1/2$ and Fourier transforming with respect to $\boldsymbol{\kappa}$ leads to an interband Wigner function [and correspondingly to intraband Wigner functions when one transforms the intraband density matrices (Rossi and Kuhn, 2002)]. Especially for the interband variable in the case of parabolic bands with $\varepsilon_{c\mathbf{k}} = E_g + \hbar^2k^2/2m_c$ and $\varepsilon_{v\mathbf{k}} = -\hbar^2k^2/2m_v$ with conduction-band and valence-band masses m_c and m_v, respectively, and band gap E_g, the choice $\eta' = m_c/M$ and $\eta = m_v/M$, with $M = m_c + m_v$, can be more convenient because it leads to $\Delta_{c\mathbf{k}',v\mathbf{k}} = \hbar^2K^2/2\mu + \hbar^2\boldsymbol{\kappa}^2/2M + E_g$, with $\mu^{-1} = m_c^{-1} + m_v^{-1}$. In contrast to Fourier transforming with respect to $\boldsymbol{\kappa}$, as in the case of the Wigner function, here it is more useful to perform a Fourier transform with respect to $\mathbf{K}$. When a temporal Fourier transform is performed, the function $\tilde{\rho}_{\boldsymbol{\kappa}}(\omega,\mathbf{r})$ is defined as

$$\tilde{\rho}_{\boldsymbol{\kappa}}(\omega,\mathbf{r}) = \frac{1}{2\pi}\sum_{\mathbf{K}}\int dt\rho_{vc,\mathbf{K}+\frac{m_v}{M}\boldsymbol{\kappa},\mathbf{K}-\frac{m_c}{M}\boldsymbol{\kappa}}(t)e^{i(\mathbf{K}\cdot\mathbf{r}+\omega t)}, \tag{81}$$

which satisfies the equation of motion

$$\begin{aligned}\left[\hbar\omega - E_g - \frac{\hbar^2\boldsymbol{\kappa}^2}{2M} + \frac{\hbar^2}{2\mu}\boldsymbol{\nabla}^2 + V(\mathbf{r})\right]\tilde{\rho}_{\boldsymbol{\kappa}}(\omega,\mathbf{r}) &= V\delta(\mathbf{r})\left\langle c, \frac{m_c}{M}\boldsymbol{\kappa}|h_{\mathrm{OV}}|v, -\frac{m_v}{M}\boldsymbol{\kappa}\right\rangle \\ &= -V\delta(\mathbf{r})\frac{2q}{\pi m_0 q_r R_0}(-i)^\ell\mathbf{p}_{cv}\cdot\mathbf{A}_0\delta_{q_r,\kappa_r}\delta_{q_z,\kappa_z}e^{i\ell\varphi_\kappa},\end{aligned} \tag{82}$$

where we have used the identity $\sum_{\mathbf{K}}\exp(i\mathbf{K}\cdot\mathbf{r}) = V\delta(\mathbf{r})$ and assumed an excitation by a transverse Bessel beam with the topological charge ℓ and the longitudinal (transverse) wave vector q_z (q_r).

The homogeneous part of Eq. (82) takes the form of a Wannier equation for a quasiparticle with mass M and center-of-mass momentum $\hbar\boldsymbol{\kappa}$. The relative motion of the electron and hole reflects the motion of a particle with the reduced mass μ in the Coulomb potential $V(\mathbf{r})$. The right-hand side is the source term that describes the excitation by the OV. Equation (82) is solved using a composition $\tilde{\rho}_{\bar{\boldsymbol{\kappa}}} = \sum_\nu b_\nu\psi_\nu$ of solutions ψ_ν to the homogeneous equation [see Chap. 10 of Haug and Koch (2009)], where ν summarizes the quantum numbers for both the relative and the center-of-mass motion.

Because of the function $\delta(\mathbf{r})$ in the source term, we notice that in the case of excitation by an OV only excitons with an s-type wave function of the relative motion can be excited. As a consequence of the factors $\delta_{q_r,\kappa_r}\delta_{q_z,\kappa_z}$, a superposition of excitons with nonvanishing center-of-mass wave vector in the longitudinal and radial directions, determined by the corresponding wave vector components of the beam, is excited, with the relative phases determined by the topological charge ℓ.

By an inverse Fourier transform, the coherence in momentum space is recovered and can be used to derive the local polarization of the system, and from it the susceptibility and optical response. The spectrum presents a small shift compared to the conventional exciton theory due to the center-of-mass motion.

Thus far we have discussed dipole-allowed excitonic transitions, as they appear in many III-V or II-VI semiconductors. In some materials the microscopic dipole ($\mathbf{d}_{cv}$) or momentum ($\mathbf{p}_{cv}$) matrix element between the band edge states vanishes for symmetry reasons, and one has to go to the next order in the expansion of the microscopic wave function with respect to $\mathbf{k}$ (Elliott, 1957). This is the case in bulk Cu_2O, a material that has recently attracted a lot of attention because of the observation of Rydberg excitons with quantum numbers up to ~26 (Kazimierczuk *et al.*, 2014). In this material selection rules differing from the typical zinc blende semiconductors hold. Using group theoretical methods, Konzelmann, Krüger, and Giessen (2019) analyzed the selection rules for the excitation of large (about 400 nm radius) Rydberg excitons in bulk Cu_2O by OVs and concluded that usually dipole forbidden s and d envelope-function excitons can be driven not only by the quadrupole field of even topological charge

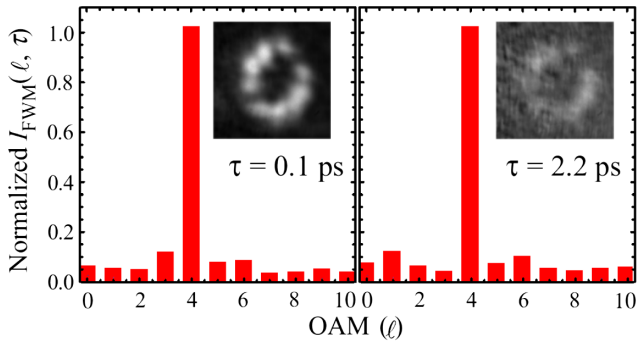

FIG. 10. Experimental evidence of OAM transfer to excitons in bulk GaN. Shown are the OAM spectrum and intensity profile (insets) of the FWM signal produced by pump with $\ell_1 = -2$ and probe with $\ell_2 = 1$ after a delay τ giving rise to a signal with $\ell = 4$, which is in agreement with theory. Adapted from Shigematsu *et al.*, 2016.

$\ell = 0, 2, 4$ but also by dipole transitions with odd topological charge $\ell = 1, 3$.

A number of experiments have been performed on bulk semiconductors that shed light on the excitation by OVs of bulk systems. Ueno *et al.* (2009) performed a four-wave-mixing (FWM) experiment in bulk GaN using a pair of LG beams to study the coherent dynamics of excitons. The FWM signal was measured to predominantly carry the topological charge $2\ell_2 - \ell_1$, which is the expected value for excitons picking the OAM of pump and probe pulses with ℓ_1 and ℓ_2, respectively. Shigematsu *et al.* (2016) extended these studies by analyzing the transfer of OAMs to values other than the expected one of $2\ell_2 - \ell_1$. In fact, additional values of OAMs are carried by the signal, as shown in Fig. 10. According to Shigematsu *et al.*'s theoretical analysis, this can be attributed to a space-dependent dephasing that generates a distribution of ℓ in the OAM spectrum even in the case of excitation with beams with well-defined OAMs. The dephasing was analyzed by comparing experiments, theory, and numerical simulations. From the experimental data they extracted a decay of the degree of OAMs, with a decay time of 88 ± 3 ps that happens to be much longer than the exciton dephasing time $T_2 = 1.9$ ps, suggesting that the OAM of the excitons is more robust than its phase coherence. Numerical simulations also show the detrimental effect of a defect on the OAM spectrum, supporting the hypothesis that space-dependent dephasing causes a broadening of the OAM signal. Four-wave-mixing experiments with OVs have also been performed on quantum wells (Persuy *et al.*, 2015), and they are discussed in Sec. IV.A.3.d.

In a different type of experiment Noyan and Kikkawa (2015) studied the dynamics of OAM transfer to the electronic degrees of freedom in doped and undoped bulk GaAs. Using time-resolved pump-probe spectroscopy and concentrating on the incoherent regime, they extended the results on the exciton dynamics beyond the coherent regime addressed in four-wave-mixing spectroscopy. The results show an unusually long decay time (picoseconds to nanoseconds) of the time-resolved OAM dichroism that can be explained neither by the typical decay times associated with momentum scattering nor by the effect of transfer of OAM from the electronic spatial to the spin degree of freedom.

The experimental work by Noyan and Kikkawa (2015) and Shigematsu *et al.* (2016) agrees on the fact that the decay time of the OAM signal is longer than expected from traditional arguments in similar systems excited by nonvortex light. One may try to explain from topology these long-lived OAM states. We have previously shown that the electric-field pattern is imprinted in the electronic state polarization. As its name suggests, every OV carries a different topological charge ℓ and imprints a particular pattern on matter. A change to the topologically distinct electronic polarization therefore implies a global change that is unlikely to occur by local interactions.

The impact of OAMs on the spin polarization of photoelectrons in unstrained GaAs excited by LG beams was experimentally studied by Clayburn *et al.* (2013), who found no supporting evidence that the OAM of light is transferred to the spin of photoexcited electrons. Later Solyanik-Gorgone and Afanasev (2019) studied the photoionization of electrons using a theoretical model with near and remote basis functions, allowing for a calculation of selection rules using the Wigner-Eckart theorem. Their results agree with those of Clayburn *et al.* (2013) after they are averaged over space; however, their model provides insight into the spatial dependence of the optical orientation, which is not available in the experiment and would be relevant to the photoexcitation of small semiconductor systems. Cygorek, Tamborenea, and Axt (2015) showed that the spin-orbit interaction in extended systems fails to transfer orbital-to-spin angular momentum of the photoexcited electron, thus complementing the theoretical explanation of the null experimental result of Clayburn *et al.*

Another argument for understanding the null experimental results is that the OV acts on the envelope part of the wave function [Eq. (69)], and thus does not affect the optical orientation, which is dictated only by the polarization (spin AM) of the light. On the other hand, a recent experiment showed a measurable effect on the polarized photocurrent generated by LG beams on GaAs photocathodes (Sordillo *et al.*, 2019). The seemingly different results from different experimental setups, and what theory explains, reflect a controversy that calls for more research on the subject.

3. Semiconductor elementary nanostructures

Material, geometry, and dimensionality strongly influence the properties of elementary nanostructures. Those based on semiconductor materials are among the most studied ones, and they are building blocks for more complex structures, for instance, microcavities (Sec. IV.B). They are quantum dots [zero dimensional (0D)] (Reimann and Manninen, 2002; Biasiol and Heun, 2011; Jacak, Hawrylak, and Wojs, 2013), quantum rings [one dimensional (1D)] (Biasiol and Heun, 2011; Fomin, 2014), quantum wires (1D) (Zhang *et al.*, 2017; Barrigón *et al.*, 2019), and quantum wells (Kelly and Nicholas, 1985; Weber *et al.*, 1999; Rosencher, Vinter, and Levine, 2012). Other systems with reduced dimensionality, which have become highly topical in the past decade, are atomically thin (2D) materials (or van der Waals materials) with the prototype graphene (Novoselov, 2011) and the class of transition metal dichalcogenides (TMDs) (Mak *et al.*, 2010; Splendiani *et al.*, 2010), which, when rolled up into nanotubes, can again form 1D systems (Fig. 6). Here 0D, 1D, and

TABLE II. Light-matter interaction Hamiltonians and their uses with an optical vortex. The fourth column refers to Hamiltonians applicable to nanostructures (Nanostr.).

Light-Matter Interaction Hamiltonians					
	Hamiltonian	Applicable to Bulk	Applicable to Nanostr.	Note(s)	Reference(s)
Minimal coupling	$[\mathbf{p}-q\mathbf{A}(\mathbf{r},t)]^2/2m+q\Phi(\mathbf{r},t)$	✓	✓	Difficult to interpret and compare to experiments.	Cohen-Tannoudji, Dupont-Roc, and Grynberg (1989)
Dipole moment	$-\mathbf{d}\cdot\mathbf{E}(t)$	✗	✗	Completely ignores the phase singularity. Applicable only to a component of the OV with no singularity.	Göppert-Mayer (1931) and Cohen-Tannoudji, Dupont-Roc, and Grynberg (1989)
Dipolelike electric	$-\mathbf{d}\cdot\mathbf{E}(\mathbf{r},t)$	✗	✗	Does not properly capture phase singularity. Applicable only to a component of the OV with no singularity.	Khitrova *et al.* (1999), Rossi and Kuhn (2002), Herbst *et al.* (2003), and Reiter *et al.* (2006, 2007)
Twisted light	$-[(1/(\ell+1)]\mathbf{d}_\perp\cdot\mathbf{E}(\mathbf{r},t)$	✗	✓	Applicable to flat structures $z\ll r_\perp$.	Quinteiro, Reiter, and Kuhn (2015)
Poincaré	$-\mathbf{d}\cdot\mathbf{E}^{\mathrm{eff}}(\mathbf{r},t)-\mathbf{m}_B\cdot\mathbf{B}^{\mathrm{eff}}(\mathbf{r},t)$	✗	✓	Applicable to all OVs.	Cohen-Tannoudji, Dupont-Roc, and Grynberg (1989) and Quinteiro, Reiter, and Kuhn (2017b)

2D refer to systems where the dimensionality reflects the number of spatial dimensions with a continuous spectrum. Nanostructures can be fabricated by molecular beam epitaxy, chemical vapor deposition, self-assembly, catalytic growth, exfoliation, etc. (Moriarty, 2001; Ihn, 2010).

The analytical description of their electronic properties often uses the envelope-function approximation with the resulting electron wave function $\psi_{b\alpha}(\mathbf{r})=\mathcal{E}_{b\alpha}(\mathbf{r})u_b(\mathbf{r})$ [see Eq. (52)], where $u_b(\mathbf{r})$ is the microscopic Bloch wave function at the band edge and $\mathcal{E}_{b\alpha}(\mathbf{r})$ is the envelope wave function, with α denoting the necessary quantum numbers for the specific structure under consideration. As an example, the envelope wave function for a one-dimensional quantum ring is $\mathcal{E}_{bm}(\mathbf{r})=N\exp(im\varphi)R_b(r)Z_b(z)$, with the normalization N and the OAM (or magnetic) quantum number m. The restriction to one-dimensional motion implies fixed radial (R_b) and height (Z_b) wave functions that, however, may be different for different bands.

Two main distinctions in the OV-matter interaction arise when the size of the material system is reduced below the characteristic size of the beam. On the one hand, studies on bulk semiconductors (Sec. IV.A.2) have been done exclusively in terms of vector and scalar potentials because the approximations involved in the use of other gauges that set up the interaction in terms of fields often create difficulties when applied to extended systems. However, other gauges are often useful in treating the OV-nanostructure interaction; these are the twisted-light gauge (Quinteiro, Reiter, and Kuhn, 2015), the Poincaré gauge (Cohen-Tannoudji, Dupont-Roc, and Grynberg, 1989; Quinteiro, Reiter, and Kuhn, 2017b), the electric-field or dipolelike coupling gauge (Khitrova *et al.*, 1999; Rossi and Kuhn, 2002; Herbst *et al.*, 2003; Reiter *et al.*, 2006, 2007), and the Power-Zienau-Woolley gauge (Cohen-Tannoudji, Dupont-Roc, and Grynberg, 1989). We exclude the dipole-moment approximation or Göppert-Mayer transformation because when the space dependence of the field is completely neglected it misses the characteristics of OVs. We discuss different gauges, summarized in Table II, at the appropriate point in the following. On the other hand, to observe new effects related to OVs the electron's wave function should span the phase singularity. The new effects are strongest when the nanostructure is fully centered with the singularity; this is discussed first, and only later is the dependence of the light-matter interaction and selection rules on the lateral displacement of the nanostructure and OV singularity axes reviewed.

a. The paradigmatic case of the quantum ring

As the name suggests, quantum rings (QRs) are structures that confine electrons and holes to an annular region, which can be 1D if only a single transverse wave function in each band is involved, or 2D or 3D if several subbands contribute. Quantum rings of high quality have been fabricated by molecular beam epitaxy in GaAs (Tong, Yoon, and Wang, 2012) and GaSb (Kobayashi *et al.*, 2004), and in Si by chemical vapor deposition (Yu *et al.*, 2007). They are among the basic semiconductor nanostructures that have been extensively studied in the past few decades, for they help us to understand basic principles [such as the Aharonov-Bohm effect and persistent currents (Kleemans *et al.*, 2007; Bluhm *et al.*, 2009; Schwiete and Oreg, 2009)], and because they promise various uses in nanotechnology, such as the control of spin states near the ring (Räsänen *et al.*, 2007) or the possibility to build lasers out of a stack of rings (Suárez *et al.*, 2004). Quantum rings represent the archetypical system to theoretically study OV-semiconductor interactions. This is simply due to the fact that both QR states and OVs are most naturally represented in cylindrical coordinates.

A model that captures the kinematics of electrons in a 1D QR including two bands without Coulomb interaction reveals interesting features. Quinteiro and Berakdar (2009) considered, in a second quantization formalism, interband transitions induced by the transverse component of the vector potential in the Coulomb gauge [$\gamma=1$ in Eq. (72)] with centered OV and QR axes. The OV-QR interaction matrix element [Eq. (71)]

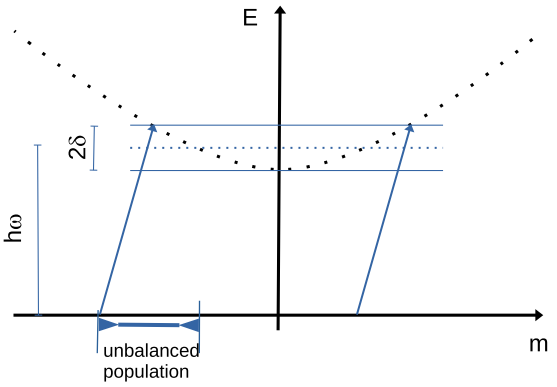

FIG. 11. Representation of tilted transitions in a QR by a finite-width (2δ) OV with a center frequency ω. For an easier understanding of the revelant process, we have realistically approximated the valence band as flat; the inclusion of the finite mass of holes is straightforward. The optical excitation generates a population imbalance, in the valence band in this simplified example, that brings about electric currents.

between wave functions with the envelope $\mathcal{E}_m(\mathbf{r}) = N\exp(im\varphi)R(r)Z(z)$ having fixed radial and longitudinal wave functions yields the simplest possible result in the RWA $\langle cm'|h^{(1)}_{\mathrm{OV}}|vm\rangle \propto \delta_{m',m+\ell}$. The EOMs (73a)–(73c) become

$$\begin{aligned}
\hbar\frac{d}{dt}\rho_{v,mm} &= 2\mathrm{Im}[\xi^*\tilde{\rho}_{vc,mm+\ell}],\\
\hbar\frac{d}{dt}\rho_{c,m+\ell m+\ell} &= -2\mathrm{Im}[\xi^*\tilde{\rho}_{vc,mm+\ell}],\\
i\hbar\frac{d}{dt}\tilde{\rho}_{vc,mm+\ell} &= \tilde{\Delta}_{cm+\ell,vm}\tilde{\rho}_{vcmm+\ell} + \xi(\rho_{v,mm} - \rho_{c,m+\ell m+\ell}),
\end{aligned} \tag{83}$$

with $\tilde{\Delta}_{cm+\ell,vm} = \varepsilon_{cm+\ell} - \varepsilon_{vm} - \hbar\omega$ and $\xi = -(q/m_0)\mathbf{p}_{vc}\cdot\mathbf{A}_0\exp(iq_z z_0)$, where equal envelope functions in the conduction and valence bands have been assumed. The equations are written in the rotating frame $\rho_{vc,mn} = \tilde{\rho}_{vc,mn}\exp(-i\omega t)$. As in the case of the semiconductor Bloch equations for noninteracting electrons in a homogeneous bulk system [Eq. (64)], the EOMs are completely decoupled and electrons undergo one-to-one transitions, but tilted in m space, see Fig. 11. The clearest description of an optical excitation process with an OV is thus achieved with 1D QRs, which in that sense are to OVs what bulk is to plane waves.

From the EOMs (83), in complete analogy with what was done for bulk one calculates the OAM transfer to electrons that contains "interband" coherence and "intraband" population contributions; see Fig. 12. The latter can be increased by increasing $|\ell|$, has a nonzero mean value, and follows the Rabi oscillations between bands. In the low-excitation regime and for short times, the z component of the angular momentum is given by $L_z^{(\mathrm{pop})} = (2n+1)\hbar\ell(\mathcal{R}_0 t)^2$, with $\mathcal{R}_0$ the Rabi frequency, t the time, and $2n+1$ the number of transition channels coupled by the light field (assuming that the OV has a spectral width, as shown in Fig. 11). It can be put to use by

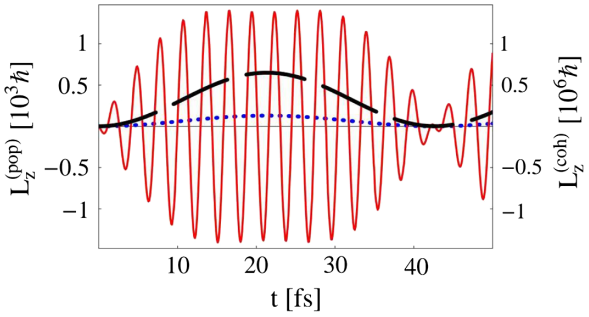

FIG. 12. OAMs of electrons in a QR. Interband (solid red curve) and intraband ($\ell = 1$ in dotted blue and $\ell = 5$ in dashed black) contributions. A similar plot holds for the electric current, calculated from a simple argument based on an electric-current loop. From Quinteiro and Berakdar, 2009.

shaping the pulse duration to set permanent electric currents and generate magnetic fields (Sec. V).

The intraband transitions in QRs also deserve attention. The theoretical simplicity exhibited by the 1D QR calls for further studies, in particular, to unveil the possible long-sought coupling of light's orbital and matter spin AM, with direct implications to technology, such as the generation of photoelectrons from bulk; see Sec. IV.A.2. To this end, a QR with a Rashba spin-orbit interaction was theoretically considered (Quinteiro, Tamborenea, and Berakdar, 2011) in a one-band model with intraband processes induced by the transverse component of a single-singularity centered OV. The problem requires the inclusion of the spin degree of freedom, transforming wave functions to spinors. The Rashba Hamiltonian reads $h_{\mathrm{SOI}} = (\alpha_R/\hbar)(\boldsymbol{\sigma}\times\boldsymbol{\pi})_z$, in which α_R is the Rashba constant, $\boldsymbol{\sigma}$ is the vector of Pauli matrices, and $\boldsymbol{\pi}$ is the mechanical momentum containing the vector potential (Sec. III.C.1). The full Hamiltonian is

$$\begin{aligned}
h = &\frac{\mathbf{p}^2}{2m_c} + V(\mathbf{r}) + \frac{\alpha_R}{\hbar}(\boldsymbol{\sigma}\times\mathbf{p})_z\\
&- \frac{q}{m_c}\mathbf{A}(\mathbf{r},t)\cdot\mathbf{p} - \frac{q\alpha_R}{\hbar}[\boldsymbol{\sigma}\times\mathbf{A}(\mathbf{r},t)]_z,
\end{aligned} \tag{84}$$

where m_c is the effective mass in the considered band and the Coulomb and radiation gauge have been assumed. An analytical solution is possible by separating h_0 from the perturbation [second line of Eq. (84)]. The expectation is that the term containing the product of Pauli matrices and OV vector potential may lead to coupling between the light's orbital and matter spin AM. From time-dependent perturbation theory without the RWA, Quinteiro, Tamborenea, and Berakdar (2011) concluded that the rate of spin conversion is not proportional to ℓ, which is in contrast to the original expectation. In addition, they found that antiparallel momenta beams produce unusual situations, an interesting finding given that other later reports also pointed to the fact that the interaction of antiparallel OV beams with matter present uncommon features (Quinteiro and Kuhn, 2014; Quinteiro, Reiter, and Kuhn, 2015; Quinteiro, Schmidt-Kaler, and Schmiegelow, 2017; Quinteiro *et al.*, 2019); see Fig. 14.

Mike, Szabó, and Földi (2018) studied a 2D QR using numerical calculations and described selection rules for the intraband transitions induced by OVs. The emission of light from OV-excited 2D QRs was numerically studied by Kraus, Wätzel, and Berakdar (2018). A few-picosecond light pulse induces rapid intraband transitions, and the subsequent dynamics under the action of electron-phonon relaxation emits light at different frequencies whose time dependence can also be analyzed. Particularly interesting is the influence of the external OV topological charge on the spectrum of short-lived high-harmonics emitted light.

A different photovoltaic effect was studied in a 2D QR using numerical simulations by Wätzel and Berakdar (2016) and Wätzel, Barth, and Berakdar (2017). They investigated in detail a centrifugal-type generation of electric currents in which the electrons separate in the radial direction due to their OAM and are collected by a ring or wire electrode.

A preliminary microphotoluminescence experiment using OVs with $\ell = 1$ on an ensemble of GaAs QRs yielded negative results (Johnson *et al.*, 2017). Johnson *et al.* speculated that the lack of observable effects was due to problems related to ensemble measurements (Sec. IV.A.3.b).

b. Excitation of quantum rings with tilted and/or displaced optical-vortex beams

On nanostructures smaller than the characteristic size of the beam, the relative position of the electron wave function to the optical axis matters; in fact, this also applies to atoms (Afanasev *et al.*, 2018; Quinteiro, Grinberg, and Schmiegelow, 2019), to trapped excitons, to impurities or defects in bulk (Shigematsu *et al.*, 2016), etc. The effects of OVs are indeed strongest when the electron cloud is centered with respect to the beam axis and excited at normal incidence. The dependence of the light-matter interaction and selection rule on the lateral displacement and tilt of field axis and nanostructure clarifies the outcome and precautions of experiments on a single nanostructure and an ensemble of nanostructures.

A reasonable strategy to cope with tilted and/or displaced beams is to use what we learned about head-on excitation. Thus, we must convert the incoming beam to a superposition of normal-incident OVs referred to the reference frame centered on the nanostructure. To reorient the incoming field one simultaneously transforms coordinates and rotates polarization vectors. Once the beam is transformed to a superposition of OVs at normal incidence, we rewrite each one as a superposition of OVs centered at the nanostructure. The composition of rotation and parallel transport of a single-singularity beam leads to a superposition of multiple single-singularity beams seen as impinging on the nanostructure head on. Every one of these OVs (with various topological charges) produces an optical transition on its own. Alternatively, one may state that from the reference frame attached to the nanostructure the displaced beam exhibits an extrinsic OAM (Bliokh and Nori, 2015) that can be converted, by translation, to a multitude of beams with intrinsic OAM.

A simpler scenario is that of a normal-incident OV, whose optical axis is displaced by a distance D from the nanostructure (Quinteiro, Lucero, and Tamborenea, 2010), as schematically shown in Fig. 13. Consider the transverse

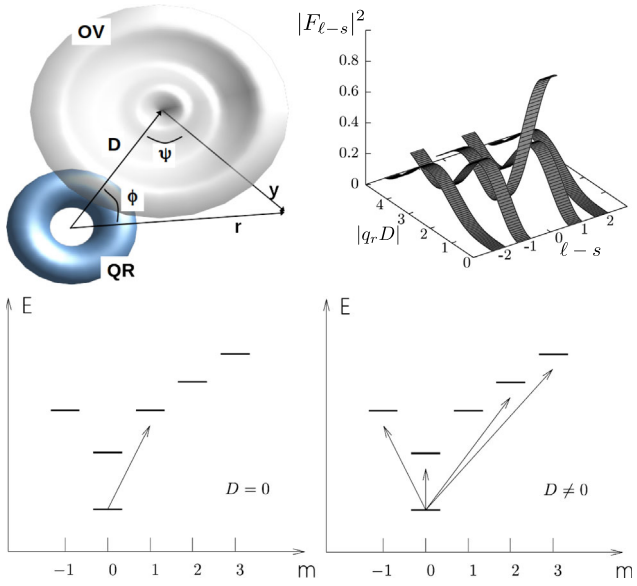

FIG. 13. Excitation of nanostructures by a displaced normal-incidence OV. Upper left panel: representation of the nanostructure (QR) and a displaced beam located at a distance D. Upper right panel: weights of the decomposition into vector potentials centered at the nanostructure; see Eq. (87). Lower panels: allowed optical interband transitions in a QR with magnetic quantum number m, examples for an OV with $\ell = 1$. Lower left panel: head-on excitation ($D = 0$). A pure one-to-one transition is predicted (Sec. IV.A.3.a). Lower right panel: once the field is displaced, transitions with other values of OAM transfer are possible. Adapted from Quinteiro, Lucero, and Tamborenea, 2010.

component of its vector potential $\mathbf{A}(\mathbf{y}, t)$ [Eqs. (4) and (21)] with a topological charge ℓ and a profile $\tilde{A}(\mathbf{y}_\perp) = A_0 F_\ell(\mathbf{y}_\perp) = A_0 J_\ell(q_r y)\exp(i\ell\varphi_y)$, for which the coordinate $\mathbf{y}$ is measured from the optical axis located at $\mathbf{D}$ from the nanostructure reference frame; see Fig. 13. Using the identity (Korenev, 2002)

$$J_\ell(q_r y)e^{i\ell\psi} = \sum_{s=-\infty}^{\infty} J_{\ell+s}(q_r D)J_s(q_r r)e^{is\phi}, \tag{85}$$

one obtains

$$\begin{aligned} F_\ell(\mathbf{y}_\perp) &= \sum_{s=-\infty}^{\infty} J_{\ell+s}(q_r D)J_s(q_r r)e^{is\phi}e^{i\ell(\varphi_y-\psi)} \\ &= \sum_{s=-\infty}^{\infty} (-1)^s J_{\ell-s}(q_r D)J_s(q_r r)e^{-is\phi}e^{i\ell(\pi+\phi+\varphi)} \\ &= \sum_{s=-\infty}^{\infty} (-1)^{\ell-s} F_{\ell-s}(D)F_s(\mathbf{r}_\perp), \end{aligned} \tag{86}$$

and the azimuthal angles with respect to a fixed axis are related by $\varphi_y = \pi + \psi + \phi + \varphi$ and $\varphi_D = \phi + \varphi$; see Fig. 13. Thus, $\mathbf{A}(\mathbf{y}, t)$ can be written as a superposition of vector potentials $\mathbf{A}(\mathbf{r}, t)$ with a topological charge s. The weight $F_{\ell-s}(\mathbf{D})$ of each component in the superposition depends on $\ell - s$, $q_r D$, and the angle ϕ. Therefore, the interaction with a QR produces one-m-to-many-m transitions induced by

$$h^{(+)} = \sum_{s=-\infty}^{\infty} (-1)^{\ell-s} F_{\ell-s}(\mathbf{D}) \left[-\frac{q}{m_0} \mathbf{A}_s^{(+)} \cdot \mathbf{p} \right], \quad (87)$$

as shown in Fig. 13.

Even nonvortex fields such as Gaussian beams exhibit the same behavior. When the optical axis is displaced and the beam width is of the same order or smaller than the size of the nanostructure, nonvertical transitions are allowed.

Somewhat connected to this discussion is the study of the interband transitions in a QR induced by inclined plane waves by Vänskä *et al.* (2011). They found that the tilt of the beam with respect to the QR axis results in new selection rules such that the OAM of the electrons' envelope ($\hbar m$) is not conserved. Moreover, by expressing the plane wave in terms of Bessel functions they concluded that the original beam can be seen as a superposition of OVs with various topological charges.

Finally, the preceding discussion clarifies a possible strategy to cope with a multiple-singularity field interaction, such as a superposition of displaced single-singularity beams, Mathieu beams, etc. (Sec. II.D). If multiple singularities shine on a coherent electronic excitation (such as in a mesoscopic QR), each one of them can be converted to OVs centered on the excitation [Eq. (86)]. The total interaction is then given by the sum of interaction terms as in Eq. (87), which translates into a sum of the responses in the regime of linear optics.

c. Quantum dots

Within the class of man-made nanostructures, quantum dots (QDs) are certainly among the most prominent ones. From a theoretical point of view, they are especially interesting since they present a discrete set of energy levels, much like atoms. This makes them particularly interesting candidates for applications in the field of quantum information technology, such as emitters of single photons (Michler *et al.*, 2000; Dusanowski *et al.*, 2019) or pairs of entangled photons (Stevenson *et al.*, 2006; Schimpf *et al.*, 2021). They are fabricated in a variety of different materials and shapes. Those fabricated from semiconductors inherit the band structure of the bulk material, and the discrete energy levels are grouped in shells, making them sensible to excitation by light.

Before engaging on the OV-QD interaction, we remind the reader that within the envelope-function approximation the wave function of electrons in a cylindrically symmetric nanostructure is given by Eq. (52) with the envelope function $\mathcal{E}_{bmn} = N \exp(im\varphi) R_{bmn}(r) Z_b(z)$ with angular momentum (m) and radial (n) quantum numbers (Jacak, Hawrylak, and Wojs, 2013). Here a factorization of in-plane and out-of-plane directions has been assumed and the thickness has been taken to be so small that only a single function Z_b contributes. The spin or (in the presence of spin-orbit coupling) the total angular momentum of the microscopic Bloch states can be included in the band index b. In addition to the envelope OAM $\hbar m$, the electron (or hole) has band and spin contributions to the AM. From the functional form of $\mathcal{E}_{bmn}(\mathbf{r})$, one immediately realizes that there will be a selection rule for the envelope AM, but as happened in bulk for cylindrical wave functions, a multitude of radial states are excited by an OV with a single topological charge.

Geometry dictates to a large extent the complexity of the interaction with light; we have seen that the simplest structure for an OV-nanostructure interaction is the QR. Therefore, our discussion focuses mainly on lens-shaped, cylindrically symmetric self-assembled QDs; however, we also comment here on the effects due to reduced symmetry, as in elongated QDs. Self-assembled QDs are routinely fabricated in laboratories around the world, and the theoretical and experimental knowledge is vast. In the early times of QD research experiments were commonly performed on ensembles of QDs exhibiting a distribution of sizes and, thus, of transition energies and dipole matrix elements; as a result of highly refined sample fabrication and detection efficiencies, current measurements on single QDs with good precision in the positioning of light beams with respect to the QD are routinely performed.

We now reexamine the generic Bessel-type OVs of Eqs. (21)–(24). From a viewpoint of control, these fields are highly tunable by changing the topological charge ℓ, the circular polarization σ, the relative OAM to SAM direction, the degree of paraxiality expressed by the ratio q_r/q_z, and the type of beam as determined by γ. The freedom in shaping the beam allows one to envisage different sorts of excitation modes; see Fig. 14 for three examples. One foresees that OVs have potential for applications that are considered in Sec. V. Here we concentrate on basic properties that are associated with the excitation of QDs by OVs with different parameter values. In addition to the standard case of excitation by a plane wave illustrated in Fig. 14(a), we discuss three modes of excitation of a cylindrically symmetric QD treated in an effectively six-band model [conduction, heavy-hole (HH), and light-hole (LH) bands, each with two orientations of the intrinsic angular momentum] without taking into account two-particle interactions. In the s-type conduction band the band and spin angular momentum consists only of a spin part with $J_z = \pm 1/2$; in the p-type valence bands the heavy-hole band is characterized by $J_z = \pm 3/2$ and the light-hole band is characterized by $J_z = \pm 1/2$.

The first mode [Fig. 14(b)] makes use of the OV parameters $\ell = \pm n$, $\sigma = \pm 1$ (parallel momenta beam), and $q_r/q_z \ll 1$; for any value of γ, the transverse field component dominates the interaction (see Table III), connecting the usual heavy-hole band states $J_z = \mp 3/2$ to the conduction-band states $J_z = \mp 1/2$ transferring the OAM and producing nonvertical transitions in the envelope quantum number m. Note that in this review we use the electron picture; the angular momenta of the valence-band states therefore have the opposite sign of the corresponding valence-band hole. A detailed study based on Fermi's golden rule (Quinteiro and Tamborenea, 2009b) concluded in addition that the strength of the excitation depends on the ratio ζ (typically small) of QD to beam sizes, and it compares to the strength of excitation by plane waves [mode (a)] as

$$\frac{|h_{\mathrm{OV}}|^2}{|h_{\mathrm{PW}}|^2} \simeq \zeta^{\ell}. \quad (88)$$

Moreover, the absorption spectrum for different types of OVs can be predicted (Kuhn, Reiter, and Quinteiro, 2015).

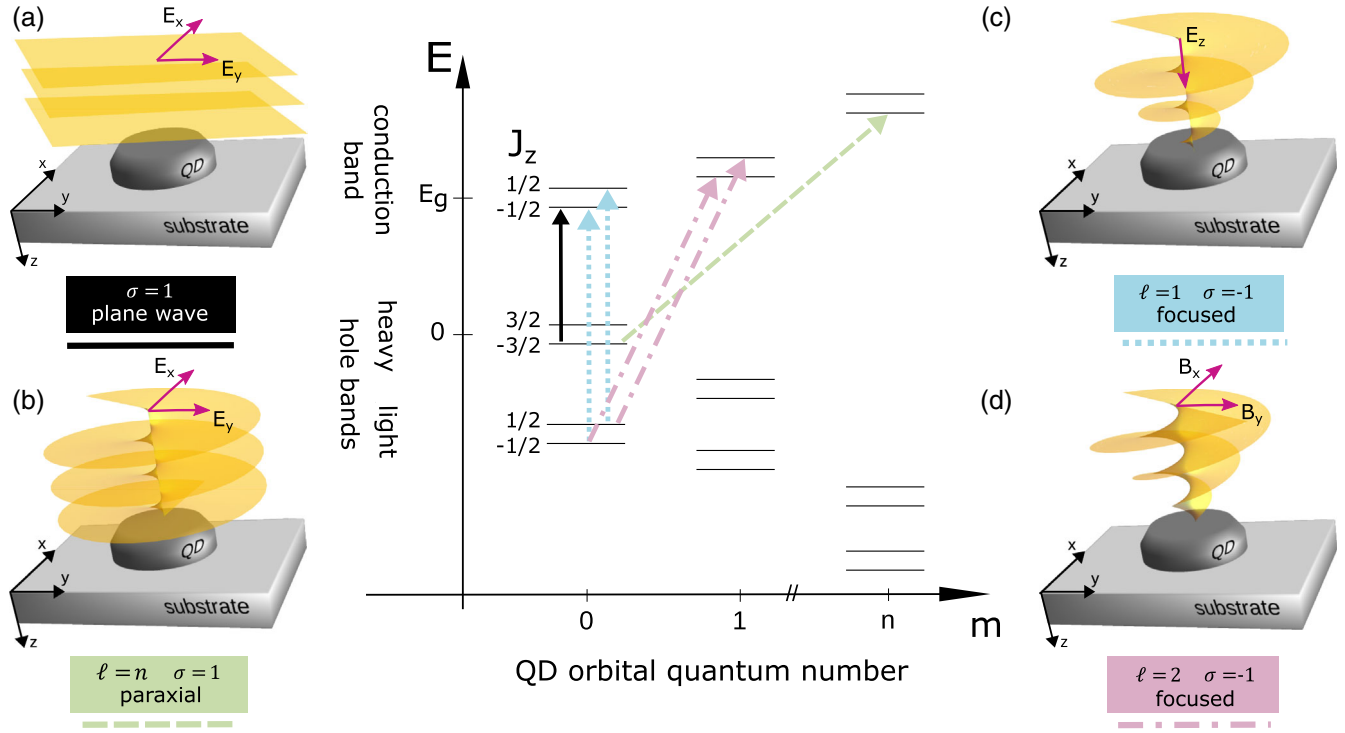

FIG. 14. Three possible modes of excitation of a lens-shaped semiconductor QD created by varying the OV beam parameters ℓ, σ, γ, and q_r/q_z. For comparison, (a) presents the usual excitation by a plane wave. (b)–(d) Representations of the field, the material system, and the modes of excitation; see Table III. Center panel: single-particle QD energy levels and characteristic transitions induced by the corresponding beam in each panel.

The second mode (c) of excitation relies on antiparallel spin and orbital momenta with $\ell = \pm 1$, $\sigma = \mp 1$, a high nonparaxiality degree $q_r/q_z \simeq 1$, and again an arbitrary γ (Quinteiro and Kuhn, 2014). For these sets of values, the interaction is dominated by an essentially homogeneous electric field in the longitudinal direction, a curious feature of OVs anticipated in Sec. IV.A. The interaction matrix element can be conveniently calculated using the dipole-moment approximation expressing the Hamiltonian in terms of fields; the lack of spatial dependence of the longitudinal component over the region of the QD enables one to use this approximation despite the fact that other components exhibit a phase singularity. If the frequency of the beam is tuned to excite electrons from the light-hole band with the Bloch microscopic part $u_\pm(\mathbf{r}) = \langle \mathbf{r}|J, J_z\rangle$ (Bastard, 1988), where $|J, J_z\rangle$ is

TABLE III. Dominant fields for the three modes of excitations of a self-assembled quantum dot, complemented by the case of excitation by a plane wave as mode (a). The symbol $\|$ refers to the relative orientation of SAM and OAM, with P denoting parallel and AP antiparallel orientations; arb. refers to an arbitrary value of γ. For comparison, we also present the excitation mode of a plane wave.

Excitation Modes of a Quantum Dot						
Mode	γ	σ	ℓ	q_r/q_z	$\|$	Dominant field
(a)	⋯	± 1	0	0	⋯	$\mathbf{E}(\tilde{\mathbf{r}}) = E_0\mathbf{e}_\pm$
(b)	arb.	± 1	$\pm n$	$\ll 1$	P	$\tilde{\mathbf{E}}(\mathbf{r}) = E_{0n}(q_r r)^n e^{\pm in\varphi}\mathbf{e}_\pm$
(c)	arb.	∓ 1	± 1	$\simeq 1$	AP	$\tilde{\mathbf{E}}(\mathbf{r}) = \mp E_0(q_r/q_z)\mathbf{e}_z$
(d)	1	∓ 1	± 2	$\simeq 1$	AP	$\tilde{\mathbf{B}}(r) = \mp B_0(q_r/q_z)^2\mathbf{e}_\pm$

$$|3/2,+1/2\rangle = -\frac{1}{\sqrt{6}}[(|p_x\rangle + i|p_y\rangle)\downarrow - 2|p_z\rangle\uparrow],$$
$$|3/2,-1/2\rangle = -\frac{1}{\sqrt{6}}[(|p_x\rangle - i|p_y\rangle)\uparrow + 2|p_z\rangle\downarrow], \quad (89)$$

with the atomic orbitals $|p_j\rangle$ and the spin orientation indicated by the arrows. The E_z component couples to the p_z orbital, producing electron-hole pairs with total (envelope + band+ spin) angular momentum equal to zero. Moreover, the strength of the interaction is, in contrast to the previous mode of excitation, comparable to that of irradiation by plane waves; this is due to the fact that $E_z(t)$ is approximately homogeneous over the extension of the QD.

In the third example (d), the beam is tuned to $\ell = \pm 2$, $\sigma = \mp 1$, a high nonparaxiality degree $q_r/q_z \simeq 1$, and $\gamma = 1$ (Quinteiro and Kuhn, 2014; Quinteiro, Reiter, and Kuhn, 2017a). The dominant contribution to the interaction comes from the in-plane components of the magnetic field that, close to the phase singularity, can be approximated by a constant. Once again, as anticipated in Sec. IV.A, this is an unusual behavior of OVs as it is a magnetic interaction at optical (ultrahigh) frequencies. The interaction can be expressed in terms of fields, although the use of the dipole-moment approximation is inappropriate. A correct and general theoretical description of the interaction with antiparallel momenta beams is provided by the Poincaré gauge (Quinteiro, Reiter, and Kuhn, 2017a) that results in the Hamiltonian

$$h_{\mathrm{OV}} = -\frac{q}{2m_0}\mathbf{B}_{\perp}(\mathbf{r},t)\cdot(\mathbf{r}\times\mathbf{p}),$$

which resembles the well-known magnetic-dipole interaction but with a space-dependent field. When resonant with the transitions from light-hole bands [Eq. (89)], the OV induces a nonvertical transition in m with zero band + spin angular momentum.

The previously mentioned studies expose the unlocking of new selection rules in QDs, i.e., transitions with changes in the envelope as well as the microscopic parts of the wave function. Most notable is the excitation of electron-hole pairs with an unusual AM, which results from the combination of a longitudinal electric field or a transverse magnetic field with light-hole states; the action of these OV components on bulk has not yet been reported (Sec. VI).

A more realistic model of a QD includes two-particle interactions and other effects. Such a model serves to verify or falsify the findings of the aforementioned simple model, can be used to predict new effects, and, most importantly, is useful to compare predictions to experiments. Holtkemper *et al.* (2020, 2021) included the Coulomb interaction, valence-band mixing, and the effects of QD asymmetry using a configuration-interaction approach. Figure 15 compares the spectra of a single-particle (reduced) model to the spectra of the full model with interactions.

The full model reproduces important features of the simplified model, for instance, the important predicted zero total AM e-LH pair $S \to s\mathrm{LH}\pm 0$ (for nomenclature see the caption of Fig. 15). In addition, we learn that this e-h pair strongly mixes with the $d \to s\mathrm{HH}\pm 2$ pair. Moreover, using a longitudinal electric field one can excite high-energy dark excitons, such as $d \to s\mathrm{HH}\pm 2(+S \to s\mathrm{LH}\pm 0)$. Note that the state with band + spin AM zero is not completely dark, as it can radiate into a field that propagates in the in-plane direction with an electric field in the z direction. In contrast, the exciton with a band + spin AM equal to 2 is truly dark. The full model awaits for experiments, especially on single QDs.

Quantum dot ensembles are a common and easy to prepare and measure experimental system. Though tempting for the study of OV-QD interaction, the analysis of signals obtained from such measurements presents a significant challenge. In Sec. IV.A.3.b we saw that nanostructures illuminated by tilted and/or displaced single-singularity OVs exhibit complex excitation paths that would result in complex spectra. Different QDs will react according to where the optical axis of the single-ℓ OV impinges the ensemble. An extinction experiment on an ensemble of QDs could record the intensity of the light passing through the sample as a function of the energy in a range that spans a number of QD levels. Simulated spectra are shown in Fig. 16. A simple or reduced model (see Figs. 15 and 14), as shown in the upper panel of Fig. 16, is used. We compare, for two values of the topological charge, the absorption spectra of an ensemble of QDs and a single centered QD. The ensemble spectra reveal no qualitative difference for the $\ell = 0$ (Gaussian) or $\ell = 1$ (OV) beams and would make the interpretation of measurements difficult. On the contrary, the single-QD spectra show clear differences; most notably, the peak at $E_g + \hbar\omega_c$ is seen only for $\ell = 1$.

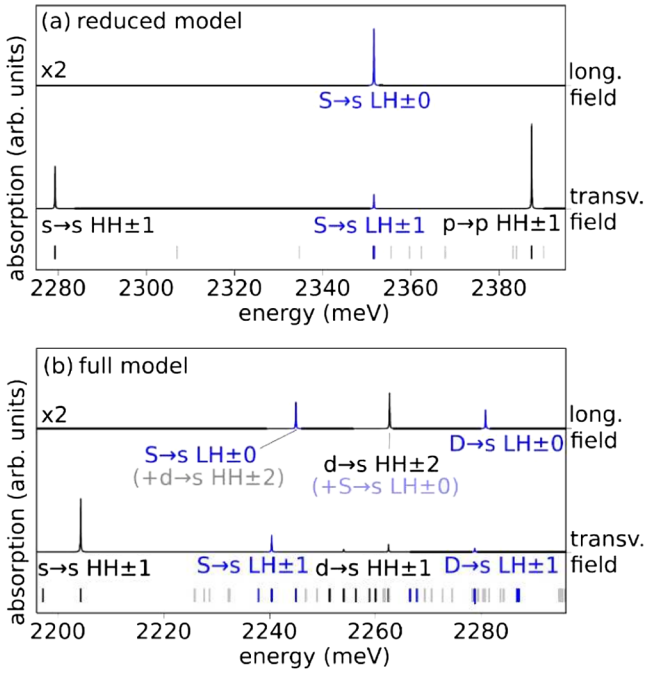

FIG. 15. Calculated spectra for a QD excited by the transverse and longitudinal components of an OV. (a) Single-particle picture. Lines correspond to electron-hole pairs. (b) Model including Coulomb interaction and valence-band mixing. Lines correspond to excitons. Each line is named according to its "envelope-hole → envelope-electron" pair, with the additional information of its light-hole (LH) or heavy-hole (HH) character and the microscopic (band + spin) angular momentum. The energy levels are grouped in shells $s, p, d, \ldots$ for electrons and heavy holes and $S, P, D, \ldots$ for light holes. In the full model, exciton states are superpositions of noninteracting pairs. When the superposition is dominated by more than one e-h pair, the second contribution appears in parenthesis: for example, $d \to s\mathrm{HH}\pm 2(+S \to s\mathrm{LH}\pm 0)$ is a high-energy exciton with an admixture of HH-e and LH-e pairs in which the holes are in different shells (d and s). From Holtkemper *et al.*, 2021.

d. Other nanostructures

The peculiarities of OVs also result in interesting new effects in nanostructures besides QRs and QDs. This is the case for two-dimensional systems and nanoparticles.

In a combined theoretical and experimental work Persuy *et al.* (2015) analyzed the OAM contributions to different diffraction orders of wave-mixing experiments. By performing four-wave-mixing spectroscopy with LG beams on a CdTe quantum well sample, they demonstrated that the selectivity of the OAM transfer can be used to extract a four-wave-mixing signal even in the case of collinear pump and probe beams, which suggests the possibility of enhanced spatial resolution by excitation through a microscope objective.

The action of a longitudinal electric-field component in the excitation of a quantum well was investigated theoretically by Sbierski, Quinteiro, and Tamborenea (2013). They considered an excitation in the infrared range to induce intersubband transitions, using OVs with different topological charges that impinge on the sample at normal incidence. As is the case for interactions with QDs (Secs. IV.A.3.c and V), the claim is that the excitation by an E_z component is experimentally easiest if

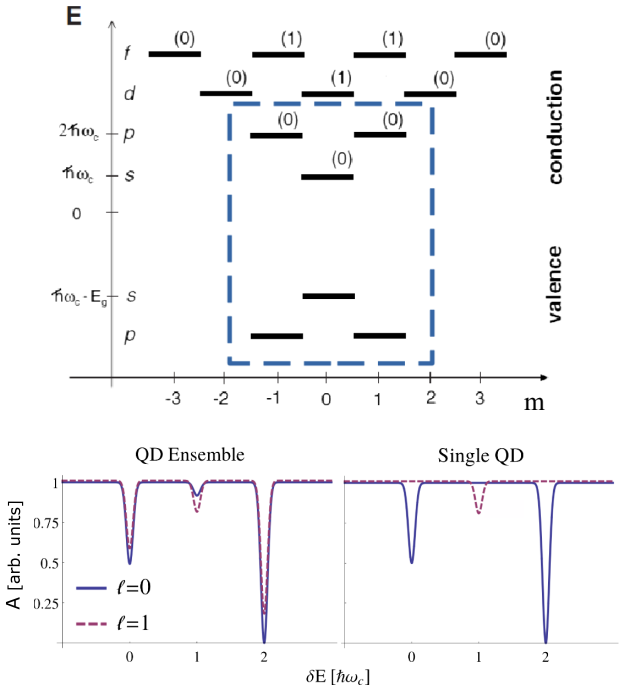

FIG. 16. Simulated extinction experiment on a single centered and an ensemble of QDs. Upper panel: single-particle energy levels of a QD in a reduced model, with m the envelope OAM, and in parenthesis the radial quantum number (Quinteiro and Tamborenea, 2009b). Lower panel: extinction spectra using beams with $\ell = 0$ (Gaussian) and $\ell = 1$ (LG). The light frequency $\omega = (E_g + \delta E)/\hbar$ scans the energy levels within the blue dashed box (upper panel). The absorption manifests as dips in the extinction spectra. No qualitative difference exists between the Gaussian and LG excitation for the ensemble measurement; in contrast, clear differences appear for an experiment on a single QD.

done at normal incidence because it does not require cleaving of the sample.

Cygorek, Tamborenea, and Axt (2015) theoretically studied QWs (and QDs) with Rashba interactions in order to explore the possibility of transferring angular momentum from an OV to the spin of electrons via the spin-orbit interaction. It was found that spin-orbit interactions at the level of the effective mass approximation are unable to produce the desired net transfer in large systems (thermodynamic limit), leaving quantum disks or dots and rings as the only possible scenarios for significant OAM to SAM transfer.

Tikhonova and Voronina (2022) analyzed the interband transitions in a semiconductor quantum well (disk) induced by a quantum nonclassical OV field, revealing a transfer of correlations to the electronic system.

The selection rules, transfer of OAM, and induced photocurrents in a two-dimensional electron gas were theoretically studied by Takahashi, Proskurin, and Kishine (2018, 2019). They found that the current in bulk is canceled out, but there remains a current that flows along the edge of the system, thereby inducing magnetization.

The electronic wave function kinematics in a macroscopic stripe of GaAs was numerically simulated using Schrödinger's equation (Wätzel, Moskalenko, and Berakdar, 2012). The deflection of the wave package occurs in the region where the OV intensity is significant; moreover, the report shows that even the use of OVs with random additional phases, simulating natural light, produces deviations of the electron's trajectory.

In a report combining experiments and Mie theory, Nechayev *et al.* (2019) considered the inverse problem of orbital-to-spin AM conversion. They showed that a linearly polarized OV focused on a silicon nanoparticle results in circularly polarized scattered light.

Using a time-dependent Keldysh–Green's function method, Shintani *et al.* (2016) considered the effects of OV pulses on the disordered surface of a three-dimensional doped topological insulator; see Fig. 17. They determined the local charge and spin densities, showed that the inhomogeneous nature of the field plays an important role, and demonstrated that the OV imprints its polarization pattern on the charge densities, in agreement with what was found in Sec. IV.A.2 for bulk and is later seen in Sec. IV.B in the case of microcavities. Most interesting is that, owing to the locking between electron spin and momentum, the optical polarization pattern determines a spatially structured spin density. The momentum-spin locking might be an indirect way to control the spin using OVs. The imprinting of the spatial pattern of the OV field was also predicted in the excitation of two-dimensional chiral ferromagnets, leading to the formation of skyrmions (Fujita and Sato, 2017).

B. Microcavity exciton polaritons

Atoms, molecules, and nanostructures placed inside optical cavities display a variety of new phenomena (Yamamoto, Tassone, and Cao, 2000). A prominent example is the inhibition or enhancement of spontaneous emission due to the Purcell effect (Purcell, 1946), but there is much more. Inside a cavity, photons and matter excitations can be strongly or weakly coupled, depending on the experimental conditions. In the weak-coupling regime, the coupling between photons and matter excitations is smaller than the individual decay rates. As a result the particles retain their individual character, and the phenomena observed resemble that of free (off cavity) light-matter interactions. However, the matter-light interaction can be strongly reduced or enhanced depending on, for instance, the position of the active structure in the cavity. Under strong coupling, photons and matter states hybridize, and extraordinary effects take place.

In a cavity containing a semiconductor structure, photons couple to excitons and, in the strong-coupling regime, form exciton-polariton quasiparticles that for not too high densities follow Bose-Einstein statistics. A semiclassical model of exciton polaritons is deduced in a similar way to that of plasmon polaritons (Sec. IV.C): From quantum mechanics one calculates an exciton dielectric function that is used in the wave equation for electromagnetic fields. For a fully quantum mechanical treatment, one quantizes the electromagnetic field and writes a Hamiltonian for excitons, photons, and the mutual coupling (Khitrova *et al.*, 1999; Haug and Koch, 2009).

An extensively investigated system is that of a quantum well microcavity. The system is fabricated using on each side of the quantum well a set of thin layers of alternating refractive

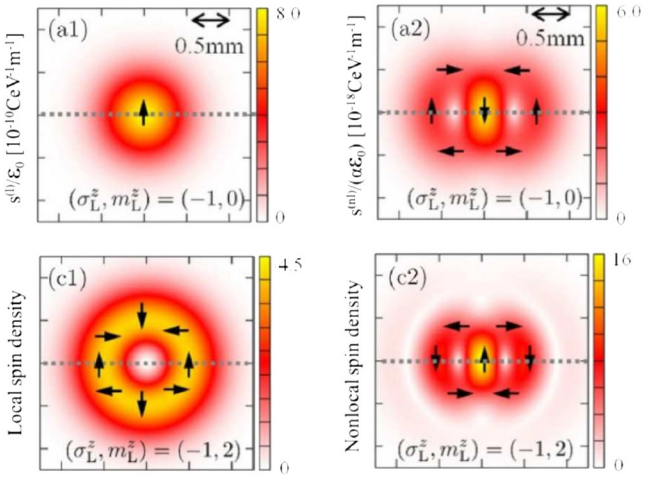

FIG. 17. Spin density induced by the electric field of an optical vortex. Left (right) panels: local (nonlocal) spin density. The color map and the direction of the arrow show the magnitude and direction of the spin density, respectively. $\sigma_L^z = \pm 1$ and m_L^z are the spin and orbital AMs of the beam, respectively. Adapted from Shintani *et al.*, 2016.

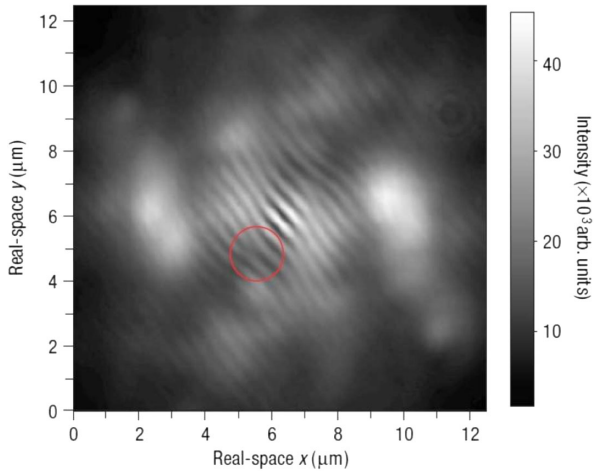

FIG. 18. Interferogram and extracted phase. The forklike dislocation can be seen within the red circle. Adapted from Lagoudakis *et al.*, 2008.

indices that act as mirrors, called distributed Bragg reflectors. By optically exciting the system from the outside, exciton-photon pairs or polaritons are formed. Many interesting phenomena have been reported. For a low polariton loss and low density of polaritons, thermalization produces a large population of zero-momentum polaritons that under suitable conditions form a Bose-Einstein condensate (Kasprzak *et al.*, 2006; Wertz *et al.*, 2010) that may lead to lasing (Deng *et al.*, 2003; Tsintzos *et al.*, 2008; Deng, Haug, and Yamamoto, 2010; Schneider *et al.*, 2013). Under strong excitation and in the strong-coupling regime, polaritons are seen to interact forming a liquid and to exhibit superfluidity (Lerario *et al.*, 2017).

Before examining the research in OV-microcavity physics, we recall that we have thus far considered only the action of external and fixed OVs on matter. Nevertheless, owing to the strong coupling of excitons and photons inside a microcavity, there is a mutual interaction between these constitutive particles. Thus, exciton-polariton vortices (called quantized vortices) can be observed without the need of pumping the microcavity with an external OV, as indeed reported by Lagoudakis *et al.* (2008). The spontaneous formation of vortical structures in a polariton fluid in a CdTe microcavity was inferred from forklike patterns in the interference of the luminescence signal coming out of the cavity; see Fig. 18. The exciton-polariton vortices are speculated to form out of a combination of system inhomogeneities and continuous (nonsingular) pumping. Theoretical modeling using the Gross-Pitaevskii equation supports the experimental findings (Lagoudakis *et al.*, 2008; Sigurdsson *et al.*, 2014; Abdalla *et al.*, 2018).

Further experimental investigations have revealed the existence of half-integer vortices in planar (Lagoudakis *et al.*, 2009) and ring (Liu *et al.*, 2015) cavities, which were first predicted in exciton-polariton systems by Rubo (2007). Half-integer vortices are known to occur in other systems such as He^3 (Salomaa and Volovik, 1987) and result from the two-component nature of polariton condensates (Toledo-Solano *et al.*, 2014).

Microcavities can be pumped using OVs. An experiment conducted by Kwon *et al.* (2019) demonstrated, again using interferometric techniques on the condensate luminescence, that a nonresonant LG pulse can inject quantized exciton-polariton vortices into planar GaAs microcavities. Furthermore, Kwon *et al.* showed that the chirality of the exciton-polariton vortex is highly controllable by the external field, which led them to conclude that the OAM of the pump beam is transferred to the exciton-polariton condensate.

A noteworthy procedure to inject quantized vortices is that of Boulier *et al.* (2016), in which four tilted and nonoverlapping Gaussian beams excite the microcavity in such a way as to produce exciton polaritons with appropriate linear momentum that convey OAM to the entire condensate. We note that the similarity to the modal decomposition of Sec. II.F is only apparent since the four Gaussian beams neither overlap to interfere nor have the appropriate phase difference.

C. Plasmonics

When light propagates inside a metal or a structured material containing metal-dielectric interfaces, the electromagnetic field interacts with conduction electrons, thereby producing quasiparticles called plasmon polaritons (Kawata, Ohtsu, and Irie, 2001; Novotny and Hecht, 2006; Maier, 2007). They exhibit notable effects, such as the confinement of the electromagnetic field to sizes of the order of a wavelength or less, and strong field enhancement. Plasmon polaritons exist in bulk and lower-dimensional systems. They are called surface plasmon polaritons (SPPs) when they are confined to a metal-dielectric interface and are called localized plasmon polaritons (LPPs) if further confined to, for instance, a small metallic sphere.

Surface plasmon polaritons are excitations that propagate along dielectric-metal interfaces but are bound in the perpendicular direction, with a corresponding evanescent field decaying in both directions from the surface. The SPP dispersion relation deviates significantly from that of light in dielectric media. For a single-interface ideal-conductor system (the paradigmatic case) the dispersion relation exhibits

a gap and a region where the in-plane wave vector can assume larger values than in dieletrics without appreciable changes in the frequency.

Owing to the spatial confinement in all directions, LPPs in plasmonic structures exhibit and are characterized by resonances in their response to external fields, such as resonance in polarizability. The resonance in polarizability results in a field enhancement, one of the main features exploited in applications. From the theory of the archetypical metallic subwavelength sphere in a dielectric medium, an understanding of other structures (such as ellipsoids and rods) can be built in which other phenomena occur, like multiple resonances, response dependent on the polarization of the excitation field, etc.

The textbook SPP is an object represented in Cartesian coordinates propagating in a uniform 2D system. As plane waves in free space, the object is a suitable building block for other, more complex excitations. But, as previously discussed, other geometries are more suitable in problems related to OVs. Liu *et al.* (2005) experimentally demonstrated SPPs in a circular system that result in the focusing of light at the center. The edge can be viewed as a set of pointlike sources (Ren *et al.*, 2011), with each emitting waves that converge inward.

Pointlike sources are also building blocks that help one understand, by the superposition principle, the SPP field of other plasmonic structures. A pointlike source on a metal-dielectric interface produces cylindrical waves of SPPs describable in terms of Hankel functions (Hecht *et al.*, 1996; Yin *et al.*, 2004; Chang, Gray, and Schatz, 2005; Nerkararyan *et al.*, 2010; Lee and Mok, 2016).

The natural next step toward the study of singular SPPs is to consider a spiral or an array of spirals (also called an Archimedean structure) milled on the metal-dielectric system. Excited from outside by a plane wave, the structure produces a vortex field around its center. The phenomenon is easy to understand: Regard the spiral as a set of pointlike sources, each emitting a secondary cylindrical wave as a result of the excitation at normal incidence by a circularly polarized plane wave of handedness σ. Their superposition at the spiral center produce a vortex, as next explained.

The field of a point source at the origin of coordinates is dominated by the electric-field z component, which in a medium with the evanescent constant χ reads, in analogy with Eq. (4), $E_z(\mathbf{r}) = \tilde{E}_z(\mathbf{r}_\perp)\exp(-\chi z - i\omega t) + \text{c.c.}$,

$$\tilde{E}_z(\mathbf{r}_\perp) = E_0 e^{i\sigma\phi} H_1^{(1)}(k\rho),$$

with $H_1^{(1)}$ a Hankel function of the first kind (outward propagation) of order 1, $\mathbf{r} = (\rho, \phi, z)$, and k the plasmon wave vector; we disregard in-plane attenuation. For observation points far from the source, $k\rho \gg 1$ and $H_1^{(1)}(k\rho) \simeq \sqrt{2/\pi k\rho}\,\exp[i(k\rho - 3\pi/4)]$; we then have

$$\tilde{E}_z(\mathbf{r}_\perp) = E_0' e^{i\sigma\phi}\sqrt{\frac{1}{k\rho}} e^{ik\rho},$$

with $E_0' = E_0 \exp(-i3\pi/4)\sqrt{2/\pi}$.

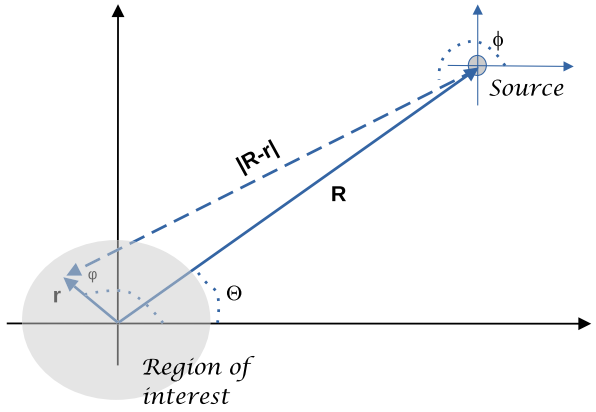

FIG. 19. Schematic of the coordinate transformation of a pointlike source that is used to generate the field of spirals.

We imagine the spiral as a set of infinitesimal segments, with each acting as a pointlike source. To calculate the outgoing field of each, we displace E_z to the corresponding position $\mathbf{R} = (R(\Theta), \Theta, z)$ on the spiral with $|m|$ turns, parametrized by $R(\Theta) = R_0 + m\Theta/k$; see Fig. 19. The observation point is now indicated by $\mathbf{r} = (r, \varphi, z)$. We approximated the distance $\rho = |\mathbf{R} - \mathbf{r}| \simeq R(\Theta) - r\cos(\Theta - \varphi)$ for the exponential factor, $\rho = |\mathbf{R} - \mathbf{r}| \simeq R_0$ for the denominator factor (as customary), and $\phi \simeq \Theta + \pi$,

$$\tilde{E}_z(\mathbf{r}_\perp) = -E_0' e^{i\sigma\Theta}\sqrt{\frac{1}{kR_0}} e^{ik[R(\Theta) - r\cos(\Theta-\varphi)]}.$$

The contribution of all point sources on the spiral to the field in the region close to the center is

$$\tilde{E}_z(\mathbf{r}) = -E_0' \frac{e^{ikR_0}}{\sqrt{kR_0}}\left[R_0 \int_0^{2\pi} d\Theta e^{-ikr\cos(\Theta-\varphi)} e^{i(m+\sigma)\Theta}\right].$$

Changing the variables to $\eta = \Theta - \varphi$, the integral becomes of the form of Eq. (36), and finally

$$E_z(\mathbf{r}, t) = E_0'' e^{i(m+\sigma)\varphi} J_{m+\sigma}(kr) e^{-\chi z - i\omega t} + \text{c.c.}, \quad (90)$$

with $E_0'' = -E_0'(-i)^{m+\sigma} 2\pi\sqrt{R_0/k}\exp(ikR_0)$. Note the similarities to the modal decomposition of Bessel beams in free space (Sec. II.F). Therefore, the superposed field close to the center presents a phase singularity. Figure 20 shows the numerical calculations of the field produced by 20 pointlike sources located on a single-turn spiral. We also show fitting curves comparing Bessel functions and numerical data. One notes that, given a spiral with a particular sense of rotation, the field at the origin has a dramatic change for each polarization of the light exciting the structure (Yang *et al.*, 2009). This is why the system is also referred to as a plasmonic lens, and the effect as a spin-orbit interaction or spin-to-orbital AM conversion. The generation of plasmons by such structures has been well documented in theoretical and experimental reports (Ohno and Miyanishi, 2006; Gorodetski *et al.*, 2008; Yang *et al.*, 2009; Kim *et al.*, 2010; Boriskina and Zheludev, 2014; Guo *et al.*, 2017; Spektor *et al.*, 2017). Plasmonic vortices

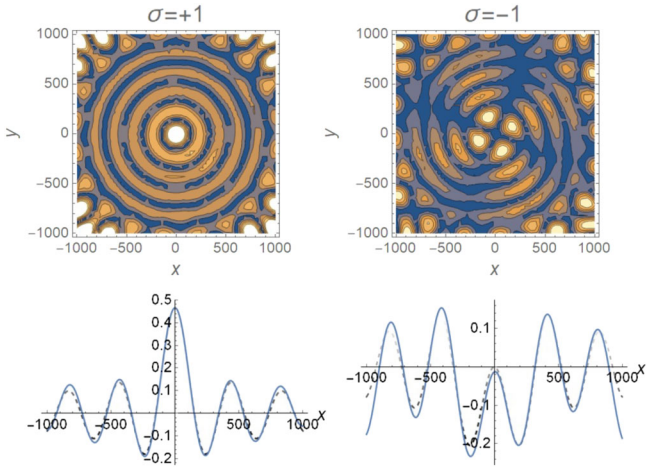

FIG. 20. Numerical calculations for a discrete single-turn spiral with $N = 20$ point sources and $m = -1$. Top row: Intensity maps. At $r = 0$ with $\sigma = 1$ there is a bright spot, while for $\sigma = -1$ there is a dark spot. Bottom row: For fixed $y = 0$ and as a function of x, numerical field amplitudes (solid blue lines) are fitted by a Bessel function J_0 ($\sigma = 1$) and J_{-2} ($\sigma = -1$) (dotted lines), showing a good match at short distances from the center and confirming the validity of the theoretical model [Eq. (90)]. Quantities are given in arbitrary units.

yield naturally subwavelength fields, achieving a lateral size of $\lambda/6$, with λ the wavelength of the incident external light (Spektor *et al.*, 2017). This is one of the most important features, as it allows one to explore a regime not accessible with far-field OVs that are limited by the diffraction limit.

Other plasmonic systems can generate singular fields, as demonstrated by Tsesses *et al.* (2019) using hexagonal structures. These act as sources of surface plane waves whose interference pattern produces a lattice of topological defects. We recall that the superposition of three or more plane waves results in singularities; see Fig. 2 and Dennis *et al.* (2010).

Interesting physics also occurs when one excites plasmonic structures with OVs. Sakai *et al.* (2016) numerically showed the creation of multipole LPPs in an air-suspended nanodisk (400 nm in diameter, 30 nm high) by studying the plasmon resonance and field maps as a function of topological charge and polarization of an incident OV. Kerber *et al.* (2018) explored the generation of plasmonic vortices in Archimedean structures by OV excitation. Their numerical results reinforce the notion that the OAM of the plasmonic vortex arises from a combination of OV parameters (topological charge and polarization) and the chirality of the plasmonic structure (Forbes and Andrews, 2018a). Through theory and numerical simulations Cao, Fu *et al.* (2021) showed that a metallic cylinder with a patterned surface reacts to incident OVs with positive and negative topological charge by either converting the incoming OAM or absorbing it.

D. Two-dimensional materials

A single layer of carbon atoms in a honeycomb lattice, known as graphene, displays striking features (Castro Neto *et al.*, 2009). It is best known for the Dirac-like behavior of electrons close to special points in k space, where no band gap exists, and the sublattice of graphene plays the role of (pseudo)spin. The seminal work of Novoselov *et al.* (2004) in graphene boosted the research on a variety of 2D materials (Novoselov, 2011), together with their applications (Fiori *et al.*, 2014; Zeng *et al.*, 2021).

Two-dimensional TMDs (a combination of a transition metal such as Mo or W and a chalcogen like S, Se, or Te) are complex systems of single or multiple layers of atomically thin covalently bound ions stacked and bound together by van der Waals forces (Miró, Audiffred, and Heine, 2014; Das *et al.*, 2015; Berkelbach and Reichman, 2018; Parvez, 2019; Shinde and Singh, 2019). In contrast to their bulk counterparts, they are direct band-gap semiconductors. A monolayer TMD shares with graphene the Dirac-like states; however, the electronic states in this case correspond to massive particles in a gapped two-band system. As in any semiconductor, exciton states are possible; in multiple layer structures excitons can be either spatially direct, with an electron and a hole in the same layer, or spatially indirect, with an electron and a hole in different layers. Compared to other semiconductor materials, TMDs are characterized by large exciton binding energies of the order of 500 meV, which is due mainly to the effectively strongly reduced screening in layers of these materials.

A first study of the interaction of graphene with OVs was conducted by Farias, Quinteiro, and Tamborenea (2013). They theoretically considered the interaction with the transverse component of an OV beam, which is described by the Hamiltonian

$$h = \hbar v_F(\alpha\sigma_x k_x - \sigma_y k_y) + e v_F[\alpha\sigma_x A_x(\mathbf{r}, t) - \sigma_y A_y(\mathbf{r}, t)], \tag{91}$$

with $\alpha = \pm 1$ designating each Dirac point and σ_i a Pauli matrix. Note the similarities with the Rashba Hamiltonian (84) for a QR: once again there is a term coupling the (pseudo)spin to the vector potential, thus suggesting the possible exchange of OAM and pseudo-SAM. Using the EOM, the evolution of the angular momentum and the induced current were calculated, reflecting the analog behavior of other systems excited by OVs in the intraband regime. New in the case of graphene is the fact that the light-matter interaction exchanges the pseudospin of the electrons, moving them from one sublattice to the other when the rotating wave approximation is invoked; however, this effect is not exclusive to OVs. Inglot *et al.* (2018) included a Rashba interaction and a static magnetic field and found no effect of the topological charge of the light field on the electron spin dynamics.

In their theoretical investigation Cao, Grass *et al.* (2021) considered the excitation by an OV of a graphene ring (Corbino disk) in the quantum Hall regime. The electric current between the inner and outer contacts was studied under disorder, and it was found that the current results from the transfer of OAM from light to electron states.

Simbulan *et al.* (2021) performed photoluminescence experiments in monolayer and bilayer MoS_2 excited with OVs, together with theoretical modeling and numerical simulations. They found a clear dependence of the energy shift on the OV topological charge that can be interpreted as

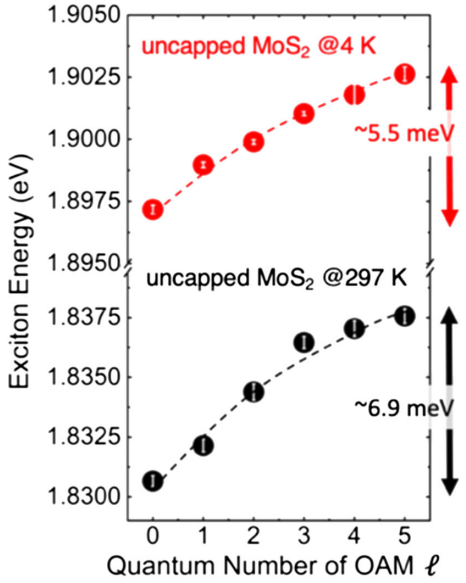

FIG. 21. Exciton energy shift for an uncapped MoS_2 sample at two different temperatures. The MoS_2 sample consists of one layer of MoS_2, one layer of *h*-BN, and SiO_2/Si. Adapted from Simbulan *et al.*, 2021.

resulting from the transfer of OAM to valley A excitons; see Fig. 21.

Transition metal dichalcogenides can easily be combined with other materials (Krasnok, Lepeshov, and Alú, 2018). Guo *et al.* (2020) implemented a hybrid system consisting of a TMD WS_2 on top of a plasmonic spiral structure on aluminum. The plasmonic vortex conveys its chirality to the achiral C excitons in WS_2, with a resulting second-harmonic generation emission that depends on the sense of circular polarization of the light exciting the plasmonic structure. Li *et al.* (2017) explored the coupling between MoS_2 excitons and plasmons from spirals using spectroscopy and numerical simulations and showed the enhancement of the photoluminescence signal for a particular state of polarization of the external light; see Fig. 22. These spin-dependent effects

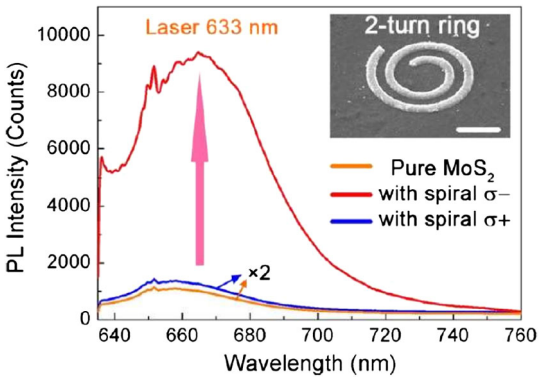

FIG. 22. Photoluminescence spectra of a MoS_2 monolayer with and without spiral structures under the excitation by light with different circular polarizations at 633 nm and laser power at 2.1 mW. Inset: Cross section view of 2-turn spiral structure (scale bar is 400 nm). From Li *et al.*, 2017.

are directly related to the spin-to-orbital AM conversion discussed in Sec. IV.C.

V. APPLICATIONS

Condensed-matter physics deals with basic physical phenomena as well as their applications. After having reviewed in Sec. IV the basic properties of OV–condensed-matter interactions, we now turn our attention to actual and prospective technologies.

Electronics, a vital technology based on semiconductors, relies exclusively on the charge of electrons. To keep up with technological progress, spintronics seeks to control the spin of electrons in nanostructured systems. A set of discoveries in the 1980s increased interest in applications based on spin, mainly giant magnetoresistance (Baibich *et al.*, 1988; Binasch *et al.*, 1989) but also the injection of spin-polarized electrons (Wolf *et al.*, 2001). Spintronics promises faster data processing, lower energy consumption, and higher miniaturization (Ahn, 2020; Hirohata *et al.*, 2020).

At around the same time Feynman (1982) proposed the concept of quantum computing for simulations of hard-to-solve many-body quantum systems. The new computer, based entirely on the principles of quantum mechanics, may outperform any conceivable classical computer (Steane, 1998; Galindo and Martin-Delgado, 2002). Basic elements of a quantum computer are according to the following five criteria formulated by DiVincenzo (2000): (i) a scalable system with logical units for storing and performing operations, the qubits; (ii) a procedure to prepare the set of qubits to a given initial state; (iii) long relevant decoherence times, much longer than the gate operation times; (iv) a "universal" set of quantum gates, which control the system dynamics via unitary transformations on qubits and thus implement the algorithms; and (v) a procedure to measure the final state of specific qubits, by reading the output of the computation.

The field of quantum technology is an expansive endeavor to outperform classical counterparts. Another example is the use of quantum light in quantum communication (Al-Amri, Andrews, and Babiker, 2021) for secure data transmission beyond classical protocols (Gisin and Thew, 2007; Liao *et al.*, 2018). Quantum computing, quantum communication, and spintronics have only recently become a reality, boosting the further exploration of diverse platforms and tools to implement their components and operations in more effective ways. A key feature for quantum technologies is entanglement. In fact, the entanglement of photons in OAM states has been observed in various experiments (Arnaut and Barbosa, 2000; Mair *et al.*, 2001; Franke-Arnold *et al.*, 2002; Krenn *et al.*, 2017), making OVs a valuable resource for applications in this field.

Solid-state physics has been an essential part of materials science, which aims to develop new fabrication and processing techniques for materials, including metals and semiconductors in various forms, in all sorts of applications. And material processing is starting to benefit from the use of OVs.

In the following, we classify applications by the area in which they were proposed or reported. This scheme is arbitrary since a proposed idea may serve several fields well

now or in the future; an example is the use of OVs in materials science [specifically in metal ablation, as reported by Hamazaki *et al.* (2010)], which may in the future become applicable in medicine for surgery (Jeffries *et al.*, 2007).

A. Semiconductor elementary nanostructures

Quantum dots are a platform for quantum technologies. Impurities or additional electrons charging the dot implement qubits via their spin. In quantum computing, one requires the control of single qubits and pairs of qubits as building blocks of more complex operations and, ultimately, algorithms. The operations on qubits can be done by optical means, improving speed and avoiding noise from electrical contacts. The single qubit operation requires the ability to control the spin direction at will. Many protocols have been devised to manipulate the in-plane (perpendicular to the nanostructure's z growth direction) spin component (Wolf *et al.*, 2001; Kroutvar *et al.*, 2004; Quinteiro, Dmitruk, and Aligia, 2012). However, it is challenging to control the longitudinal component necessary for completing all possible one-qubit operations. Quinteiro and Kuhn (2014, 2015) proposed the use of a sequence of three light pulses ($P_{\ell,\sigma}$) in the subpicosecond timescale to achieve full inversion of the spin z component of an extra electron charging a self-assembled semiconductor QD. The pulse sequence is independent of the initial spin state of the extra electron and works by inducing an e-LH pair with zero total AM (second excitation method of Fig. 14) in the QD. Figure 23 shows the results from numerical simulations of the density matrix ρ_{ij} using the master-equation formalism within a four-level system $i=\{1:|\uparrow 00\rangle, 2:|\downarrow 00\rangle, 3:|\uparrow\downarrow\Uparrow\rangle, 4:|\uparrow\downarrow\Downarrow\rangle\}$, with a single (double) arrow for the electron (hole). Note that the addition of electron-electron interactions does not affect the proposal significantly. As seen in Sec. IV.A.3.c, the full model still presents the most important ingredient of the proposal: the state $s \to s\mathrm{LH} \pm 0$, which is essential to the spin inversion.

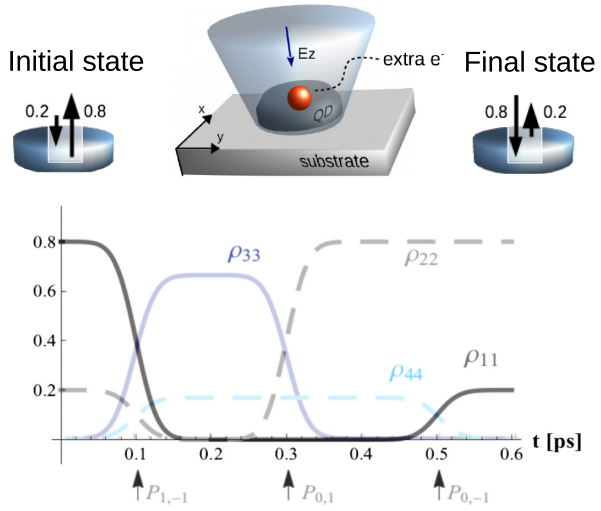

FIG. 23. Numerical simulations of the master equation for the extra electron plus e-LH system in a negatively charged QD, for the case in which the initial spin states of the extra electron is a superposition of up and down s_z. After the application of three normal-incident pulses (one an OV), full inversion is achieved on a subpicosecond timescale. Adapted from Quinteiro and Kuhn, 2014.

In fact, the $s \to s\mathrm{LH} \pm 0$ transitions in QDs may prove useful in quantum storage, as shown by Holtkemper *et al.* (2021). The Coulomb interaction produces an admixture of high-energy dark and optically active e-h pairs. In particular, as seen in Fig. 15, the e-HH pair $d \to s\mathrm{HH} \pm 2$ mixes with the e-LH pair $s \to s\mathrm{LH} \pm 0$, thereby forming an exciton that can be excited by the longitudinal component of the antiparallel $\ell = \pm 1$, $\sigma = \mp 1$ OV (the second excitation method of Fig. 14). After the light pulse is turned off, the system decays to its ground state; thus, the excited exciton relaxes, mainly by electron-phonon scattering without spin flip to the almost unmixed $s \to s\mathrm{HH} \pm 2$ state. This is optically forbidden, and thus robust against radiative recombination. The states $s \to s\mathrm{HH} + 2$ and $s \to s\mathrm{HH} - 2$ can be generated at will and represent qubits of information.

Yet another application of QDs is their use for the conversion of light's orbital AM to electronic spin AM, and vice versa. The device consists of a photonic crystal coupled to a QD, and it can work as an emitter or receiver for quantum communications (Fong *et al.*, 2018). For instance, in the emitter mode the spin state of the excited electron in the QD emits, upon recombination, light with a particular circular polarization. This drives a combination of quadrupole modes in the photonic crystal, which in turn is capable of emitting light with OAM; see Fig. 24.

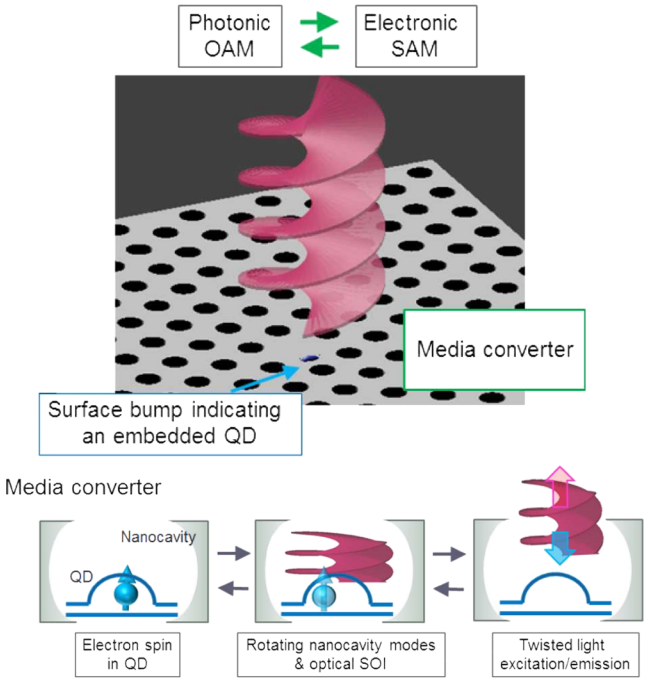

FIG. 24. Light's OAM to and from an electron spin AM conversion. Top panel: Device consisting of a photonic nanocavity with an embedded QD. Lower panels: Schematics of the conversion process. From left to right, the light emission of a spin-polarized electron drives the rotation of nanocavity modes, resulting in the nanocavity emitting an OV. From right to left, an OV drives the rotating modes, which in turn generates an electron spin in the QD. Adapted from Fong *et al.*, 2018.

Structured light, including OVs, can extract the spatial phase information of the excitonic wave functions in QDs. Holtkemper *et al.* (2020) proposed repeated absorption measurements of the state under investigation using complex fields formed out of a superposition of structured beams. A particular set of superposition coefficients will maximize the absorption. These coefficients can be directly related to the expansion coefficients of the exciton wave function in a given basis; in this way one deduces the complete exciton wave function, including the relative phases.

The transfer of OAM to nanostructures sets up an electric current that can be used in electronics, spintronics, and communications. One such application is the generation of magnetic fields in nanostructures, such as a QR (Kraus, Wätzel, and Berakdar, 2018) or bulk (Quinteiro and Tamborenea, 2009c) to control the spin state of a nearby impurity, QD, etc. Ji *et al.* (2020) demonstrated that the circular photon drag can serve to detect the OAM of light impinging a U-shaped device on WTe_2 for use in OAM-based communications.

The invention of new devices to generate OVs is an active field of research for possible use in comunications, sensing, and other applications (Kerridge-Johns, 2018). Semiconductor technology plays an important role in innovations in the field, especially in lasers that can create vortex fields from within the cavity; see also Sec. II.G. A good example is the vertical cavity surface-emitting laser (known as VCSEL) or the vertical external cavity surface-emitting laser (known as VECSEL) formed out of one or several semiconductor quantum wells coupled to additional intracavity devices; see Fig. 25. Examples of intracavity devices are metasurfaces (Seghilani *et al.*, 2016; Xie *et al.*, 2020) and spiral phase plates (Li *et al.*, 2015) that shape the beam to an OV. Micrometer-sized whispering gallery modes on solid-state systems can generate OVs with controllable topological charge and polarization state (Miao *et al.*, 2016; Zhang *et al.*, 2020; Chen *et al.*, 2021) and microlasers producing fractional OAM that can be controlled at gigahertz frequencies were reported by Zhang, Zhao *et al.* (2020).

STED microscopy, a technique that makes use of doughnut-shaped beams including OVs (Keller, Schönle, and Hell, 2007), can be used to read and control quantum states in nanostructures. Arroyo-Camejo *et al.* (2013) showed that individual nitrogen-vacancy (N-V) color centers can be resolved with STED microscopy up to 15 nm. A similar technique, so-called charge-state depletion microscopy was used by Chen *et al.* (2015) to detect and manipulate the state of N-V centers in diamond, with applications to sensing and quantum computation. The manipulation procedure combines Gaussian and doughnut-shaped beams to produce space-dependent changes in the populations of N-V^0 and N-V^- states, and they demonstrated subdiffraction manipulation of the order of a few nanometers.

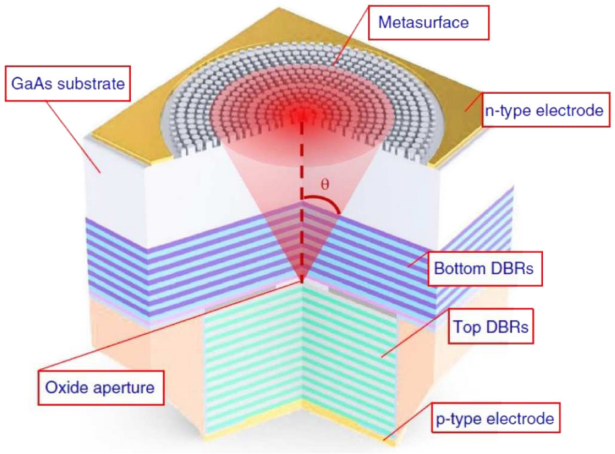

FIG. 25. Schematic of the metasurface-VCSEL system. The standard VCSEL structure and the beam-shaping metasurface integrated on the backside of the substrate. From Xie *et al.*, 2020.

B. Exciton polaritons

Exciton-polariton vortices (or quantum vortices) driven by external optical perturbation have been shown to be robust entities against changes in the power, shape, and size of the pump (Borgh *et al.*, 2012; Sigurdsson *et al.*, 2014; Kwon *et al.*, 2019; Ma *et al.*, 2020). Ma *et al.* (2020) demonstrated control and switching of the vortex topological charge in a few hundred picoseconds at nonresonant excitation. In their experiment a GaAs microcavity is excited by a ring-shaped cw field that creates a vortex exciton-polariton condensate rotating in a random sense. The topological charge is controlled and switched by an additional Gaussian laser beam that breaks cylindrical symmetry. In addition, Ma *et al.* showed robustness against the system's disorder and imperfection. Quantum vortices can also be trapped, moved, and mutually scattered, as shown by Pigeon, Carusotto, and Ciuti (2011), Sanvitto *et al.* (2011), and Dominici *et al.* (2015, 2018). Motivated by possible applications to quantum technology in information transfer and storage, Sigurdsson *et al.* (2014) considered in detail the switching and copying of quantum vortices of topological charge $\ell = \pm 1$ from one vortex to a second one created at a distance of tens of micrometers; see Fig. 26.

C. Plasmonics

Light in general, and OVs in particular, is used to trap and manipulate particles (Grier, 2003; Jones, Marago, and Volpe, 2015), and recent studies have suggested that the localization and enhancement of fields provided by plasmonics may improve optical tweezers. Liu *et al.* (2020) studied by numerical means plasmonic structures containing a spiral and a tip to trap or push away particles, depending on the topological charge of the plasmonic vortex. Hoshina, Yokoshi, and Ishihara (2020) compared two scenarios to rotate a particle using light: The first makes direct use of a LG beam, which can rotate the particle on only a macroscopic scale due to its large doughnut shape. The second employs the spin-to-orbital AM conversion by plasmon polaritons (Sec. IV.C): a circularly polarized light excites a nanostructure, consisting of four rectangular-shaped metallic pieces, that creates localized plasmonic vortices that rotate the particle on the nanometer scale.

The squeezing of fields by plasmonic structures was also exploited by Heeres and Zwiller (2014), who showed by numerical simulations that a set of nanoantennas can focus an incident OV to a subwavelength lateral size, thereby eluding

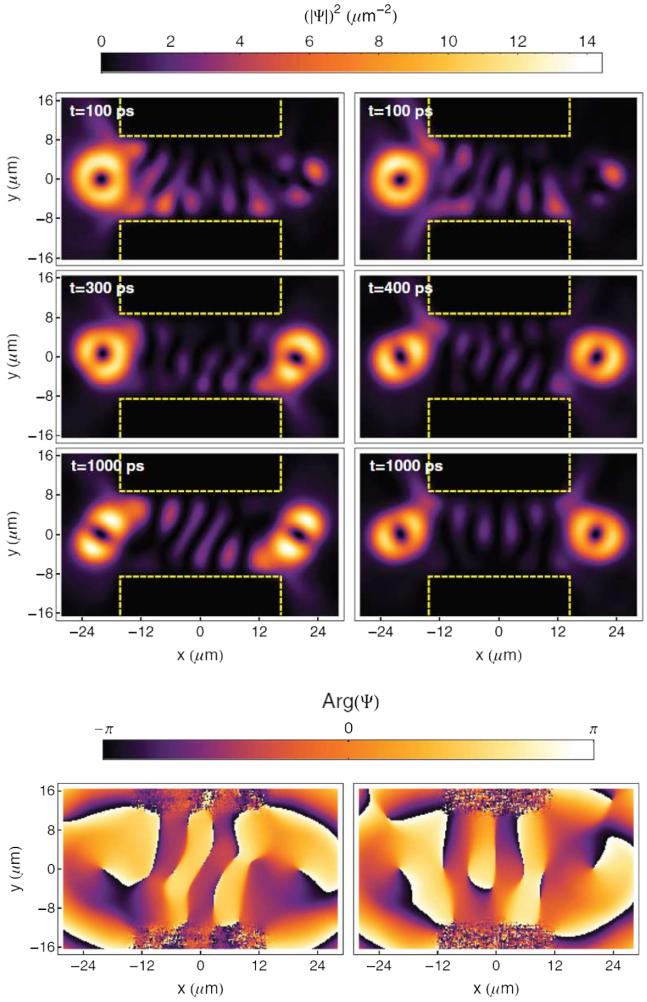

FIG. 26. Copying exciton-polariton vortices. Left column: density plots of the copier process (same topological charge). The yellow dashed lines show the edges of the guide. At $t = 300$ ps the transfer is complete, and at $t = 1000$ ps the state is nearly stationary. Right column: the inverter process (opposite topological charge). At $t = 400$ ps the transfer is complete, and at $t = 1000$ ps the state is nearly stationary. Bottom panels: phase profiles at $t = 1000$ ps. Adapted from Sigurdsson *et al.*, 2014.

the diffraction limit, and thus enhancing the light intensity close to the phase singularity. Large field intensities reduce the excitation time, improving the quantum operation speed and diminishing the importance of the decay or decoherence of states. Later Arikawa, Morimoto, and Tanaka (2017) demonstrated similar concepts in an experiment using terahertz OVs. They illuminated an array of eight antennas with an OV beam of ring diameter 310 μm and found within the array system that the OV was reduced to a ring diameter of 90 μm, a factor of 3.4 smaller; see Fig. 27.

Much work has been devoted to the exploitation of the additional degree of freedom of OAM (ℓ) for communication purposes, and high transfer rates have been achieved through fiber (Bozinovic *et al.*, 2013) and wireless (Wang *et al.*, 2012) channels by multiplexing with OAM states of light. Communication requires channels (Chen *et al.*, 2018), emitters (Jiang, Cao, and Feng, 2020), and receivers. Garoli *et al.* (2016) demonstrated an OV emitter. They designed a

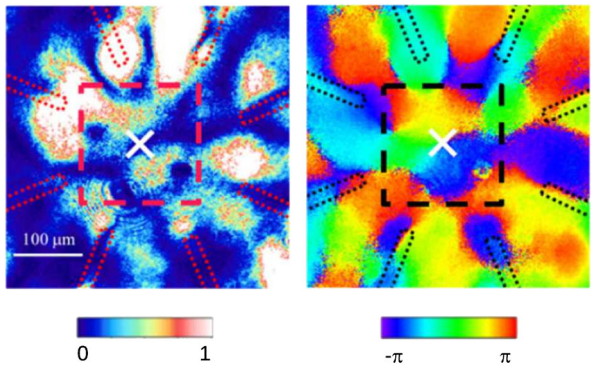

FIG. 27. Near-field distribution around the circular array antenna illuminated by a vortex beam with ring diameter 310 μm. Intensity (left image) and phase (right image) showing an intensity null at the center (white cross) and the 2π phase rotation. Adapted from Arikawa, Morimoto, and Tanaka, 2017.

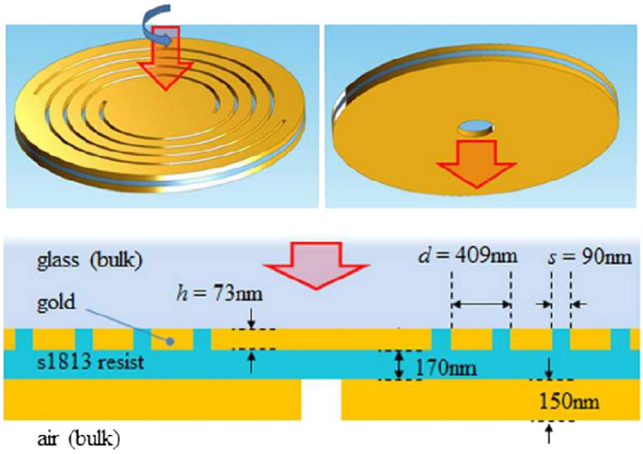

FIG. 28. Schematic illustration of the plasmonic structure emitter used to convert circularly polarized light into far-field OVs. Adapted from Garoli *et al.*, 2016.

plasmonic device consisting of a plasmonic lens (spiral structure) with a hole in its center and illuminated it with circularly polarized light. The plasmonic lens converts the nonsingular field, via the spin-to-orbital AM conversion effect, to a plasmonic vortex that upon interaction with the milled hole propagates an OV to the far field; see Fig. 28.

D. Materials science

A first use of OVs is to employ the doughnut shape of the beam, which can generate a different pattern than that of conventional Gaussian beams (Nolte *et al.*, 1997). Ablation in copper by OVs was demonstrated by Anoop *et al.* (2014), who showed the formations of annular structures of different characters depending on the values of light fluence and the number of pulses employed. Further investigation on the ablation dynamics of copper was conducted by Tsakiris *et al.* (2014) through experiments and numerical simulations. Optical vortices were reported to improve ablation on Ta plates by creating with a lower ablation fluence clearer and smoother ablated zones and less debris (Hamazaki *et al.*,

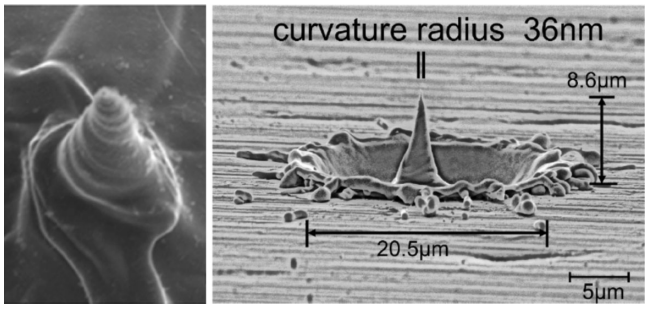

FIG. 29. Microneedles in tantalum fabricated by an optical vortex with a total AM of $J = 2$. Left image: 25° view. Right image: side view. Adapted from Toyoda *et al.*, 2012.

2010). Oosterbeek *et al.* (2018) extended the diagonal-scan method (Samad, Baldochi, and Vieira, 2008), which is used to determine the ablation threshold fluence, to weakly focused OVs and tested the method by measuring the ablation on silicon and quartz. In their inverse work, Nivas *et al.* (2015) sought to understand how an OV could be investigated via the ablation spots that it produces. They found that spot features such as the surface texture and the size of the annulus depend on the local fluence, number of pulses, and polarization (radial, azimuthal, or circular).

Optical vortices can do more than ablate structures in annular shapes, and the formation of chiral structures has been demonstrated by several groups. Such chiral nanostructures may help us to further probe the interaction of light with chiral matter, study the optical activity and chirality of molecules, and create new devices for quantum information purposes (Omatsu *et al.*, 2019). Chiral microstructures such as needles and fibers result from the direct illumination of intense OVs on metals (Omatsu *et al.*, 2010; Toyoda *et al.*, 2012; Syubaev *et al.*, 2017, 2019), silicon (Ablez *et al.*, 2020), azo-polymers (Ambrosio *et al.*, 2012; Juman *et al.*, 2014), isotropic polymers (Ni *et al.*, 2017), and photopolymerized resins (Lee *et al.*, 2018). Laser parameters control the formation of the structures, and most notably the helicity of the structure results from a combination of the light's OAM and SAM; see Fig. 29.

VI. CONCLUSIONS AND OUTLOOK

The early 1990s witnessed a breakthrough in optics with the development of techniques to generate coherent beams of highly inhomogeneous light known as OVs or twisted light. These objects exhibit unique features (most notably phase singularities and OAM) that challenge our intuition based on plane waves and Gaussian beams. These properties are more than a curiosity and bring about a new physics in their interaction with matter, with important implications for technology.

This review has addressed the physics of the interaction of OVs with condensed-matter systems, providing the theoretical basis and a detailed account of current progress in theoretical and experimental research as well as in applications to the field. In Sec. VI.A we summarize the main aspects discussed thus far. We then finish this review with an account of our perspective on the future directions that research on OV-condensed-matter interactions may take to unfold new physics and applications and on challenges associated with these developments. These are by no means exhaustive: they are meant to spark the reader's curiosity and to help one discover their own research line.

A. Concluding remarks

A historical account of discoveries leading to the understanding of light and its interaction with matter introduced the theoretical description of OVs. We surveyed their most curious and relevant properties. A key concept in the classification of optical beams is the paraxial approximation, which has been the basis for the majority of theoretical and experimental studies on optical beams either with or without singularities. Beams in this regime are characterized by purely transverse electric and magnetic fields, and OVs may exhibit a well-defined topological charge and circular polarization. The paraxial regime is limited to beams with characteristic lateral dimensions much larger than the wavelength. Going beyond this limit, the beams may exhibit interesting new phenomena such as a strong component in the propagation direction or a dominant magnetic field close to the singularity, and in general there are components with different topological charges. These features create new possibilities, for instance, for the optical control of nanostructures. We provided a detailed discussion and comparison of paraxial and full solutions of the Helmholtz equation, exemplified by the well-known Laguerre-Gauss and Bessel beams, respectively. Other solutions were mentioned, thus emphasizing the existence of OVs with multiple singularities. We discussed the derivation of OVs from potentials and the role of the gauge, particularly in the nonparaxial regime, as well as the representation of OVs in terms of plane waves, aspects of generation and measurement of the OAM content, and the impact that the subject has on physics, chemistry, and biology.

The field of OV–condensed-matter interactions builds on a long history of condensed-matter physics, particularly in solid-state physics and condensed-matter optics. To provide the necessary background, we offered a focused overview of the basic concepts of solid-state physics relevant to the field. A recount of the crystalline state reminded the reader of the electronic state of semiconductors and metals that form the basis of simple and complex systems. Bulk materials and the relevant nanostructures, like quantum wells, dots, and rings, together with the modern two-dimensional materials, were introduced. Motivated by the subject of the review, we focused on condensed-matter optics. The issues of gauge choice and invariance were carefully examined, and the usual approximation of vertical optical transitions for plane-wave-like or weakly inhomogeneous light fields was then revisited. A theoretical toolbox to treat the dynamics of condensed-matter systems under light excitation was presented in detail. The formalism most often applied in the field of OV–condensed-matter interactions is based on the equations of motion for the single-particle density matrices and aptly accommodates both light-matter and electron-electron interactions. However, other approaches like nonequilibrium Green's functions have also been used and are therefore reviewed.

Early sections of the review paved the way to the main part of the article: an analysis of the fundamental theory of the interaction of OVs with condensed-matter systems alongside a review of the current literature in the field. Standard semiconductor optics is a rich discipline despite the fact that it is based on strong simplifying assumptions regarding the light-matter interaction. We pointed out that these customary and almost silent assumptions are the first conceptual sacrifices needed to describe the effects of structured light on matter. The main misleading assumptions that must be abandoned are vertical-transition and dipole-moment approximations. And other notions that hinder a sound understanding of this new field are the beliefs that light beams interact with matter mostly (or only) via their transverse electric field, that bulk semiconductors represent the simplest model to understand the OV-matter interaction, and that light is always well represented by plane waves. Stripped away from notions that could lead us off track, we studied the theory of crystal-OV interactions that constitutes a building block to tackle phenomena taking place in many systems.

In bulk semiconductors, the light-matter Hamiltonian matrix elements in the case of strongly inhomogeneous light fields have to be recalculated and novel selection rules based on the conservation of total angular momentum are obtained. The OAM is transferred from the light beam to the photoexcited electrons, thereby generating macroscopic currents and ultrafast local magnetic fields. Various experiments have indeed confirmed this transfer of AM. When the electron-electron interaction is taken into account, the rich physics of excitons comes into play, modified by the finite OAM of the structured light, which results in the creation of excitons in a superposition of states with nonzero center-of-mass momentum.

Semiconductor nanostructures add the complexity of their own spatial inhomogeneity, which is typically handled using the envelope-function approximation. Here again novel matrix elements for the light-matter interaction dictate the allowed and forbidden optical transitions, which are distinct from those obtained in traditional optical excitation with plane waves. Quantum rings play a central role due to their specially adapted geometry to the cylindrical nature of the twisted light beams.

In semiconductor microcavities the strong coupling between excitons and light gives rise to the formation of exciton polaritons. Here vortical structures in the polariton fluid can also form spontaneously without the need of pumping by an OV. Analogously, in metallic nanostructures the light-matter coupling leads to plasmon polaritons, which again provide new features when one studies their interplay with OVs. Of particular interest are spiral geometries, which already provide a singularity in their structure and thus may create OVs from excitation by plane waves. Angular momentum transfer has also been observed for the OV excitation of two-dimensional materials. For all these systems theory and recent experiments have been reviewed.

The peculiarities of the interaction of OVs with condensed matter resulted in many theoretically proposed or already experimentally realized applications relevant to fields such as quantum technologies, communications, sensing, and materials science. They rely on the precise control and transfer of AM, the conversion of spin and orbital AMs, the switching and copying of quantum vortices, the squeezing of OVs to subwavelength lateral size, the creation of annular structures by ablation, etc. Other applications can be envisaged. In Sec. VII.B we finish this review with our views on possible future directions in the field.

B. Current limitations and future perspectives

In a little more than a decade, research on OV–condensed-matter interactions has covered a large number of topics; nevertheless, it is safe to say that the topic is far from being exhausted. A better understanding of basic principles on explored topics (such as bulk semiconductors) is still hindered by several factors, while other topics have been only superficially studied. These include two-dimensional and other van der Waals materials, superconductors, skyrmions, localized plasmon polaritons, color centers, and nonlinear effects in solids. In the following we discuss limitations in our present knowledge together with possible future directions to overcome these limitations.

1. Inhomogeneity and excitation strength

Inhomogeneity has been a central point throughout this review; we argued that when matter fields (wave functions) are subjected to spatial variations in light's amplitude and phase, curious effects take place. Optical vortices are special objects, as they have an unavoidable phase inhomogeneity at the singularity. Irrespective of the extent of the matter field, the vortex causes unexpected effects, as demonstrated by the excitation of a single Ca ion by far-field OVs (Schmiegelow *et al.*, 2016; Quinteiro, Schmidt-Kaler, and Schmiegelow, 2017; Afanasev *et al.*, 2018). However, this strong spatial phase variation comes at a cost: the amplitude in its vicinity is small. Optical transitions are orders of magnitude weaker than their counterparts induced by nonsingular beams [see Eq. (88)], with detrimental consequences to applications that require ultrafast transitions to improve speed operation and avoid data-destroying decay or dephasing processes.

One can speak of near-field versus far-field optics, and far-field beams can be further split into collimated or paraxial and strongly focused or nonparaxial ones. Loosely speaking, the degree of field inhomogeneity can be pushed furthest in near-field optics, for which the diffraction limit does not apply. In contrast, strongly focused (nonparaxial) far fields are limited to the order of the wavelength.

Most of our knowledge regards the action of far-field OVs in typical semiconductors, such as GaAs, for which optical transitions are weak. With applications in mind, it is then a must to improve fluence around the vortex.

Far-field optics with OVs can benefit from the use of high focusing techniques and materials with large band gaps. Abbe's diffraction-limit law states that the minimum resolution d is given by $d = \lambda/2\mathrm{NA}$, with $\mathrm{NA} \lesssim 1.4$ (Chen *et al.*, 2017; Wang *et al.*, 2017) the numerical aperture of the optical system; the resolution is a measure of the beam's lateral size. High focusing is achieved by increasing the NA to decrease the lateral size of the beam. Alternatively, a change in the wavelength will compress the minimally achievable lateral size too. In interband optical transitions, the size of the band

gap determines the photon's wavelength. Semiconductors with larger band gaps (Andreev and O'Reilly, 2000; Ranjan *et al.*, 2003; Kako *et al.*, 2004; Arakawa and Kako, 2006; Jarjour, Oliver, and Taylor, 2007) are excited at shorter wavelength; thus, the lower bound d decreases. The interaction of highly focused OVs with large band-gap semiconductors is worth exploring.

An alternative is near-field optics. Little work has been done thus far, but the experimental report by Arikawa, Morimoto, and Tanaka (2017) shows that the radius of the ring exhibiting the maximum intensity of the OV can be decreased by a factor of $n \simeq 4$ (Sec. V.C); considering Eq. (88), the relative interaction strength would increase by a factor of n^{ℓ} in QDs. More enthusiastic theoretical estimates promise an enhancement of the interaction by orders of magnitude (Heeres and Zwiller, 2014).

Another route for overcoming weak excitation is to consider more extended quantum systems. A notable case central to this review is that of electronic excitations in bulk semiconductors, 1D and 2D nanostructures; nevertheless, real solids have defects and impurities that effectively reduce the span of the wave function (Takagahara, 1989; Martelli *et al.*, 1996; Leosson *et al.*, 2000), making the pursuit of more pure systems important. Yet, other quantum states of matter exhibit macroscopic wave functions : superconducting circuits, superfluids, condensates, etc. (Wan, 2006).

2. Experiments

Experimental work reveals unexpected effects, and confirms or disproves theoretical predictions. The experiments in bulk by Noyan and Kikkawa (2015) and Shigematsu *et al.* (2016) indeed confirmed the transfer of OAM to free carriers and excitons, while at the same time it showed the unexpectedly long lifetimes of OAM excitations.

There is an imbalance between theoretical and experimental work. While many theoretical predictions have been reported, only scarce experimental research was conducted, especially on elementary nanostructures. An exception is the field of microcavity exciton polaritons, where experimental and theoretical work seems to be well balanced.

Experiments with OVs and 0D nanostructures are indeed challenging. Two main obstacles hinder their realization. First, many experiments rely on ensemble measurements, which are easy to carry out but troublesome to interpret. Often the growth process (such as self-assembly) forms nanostructures of slightly different sizes and shapes, resulting in large inhomogeneous broadening on closely spaced (few meV) energy levels, which causes difficulties in the extraction of information from experiments with homogeneous light. For excitations by OVs, an additional difficulty arises from the fact that the majority of nanostructures will be located off the optical axis, which causes on them multiple optical transitions, as explained in Sec. IV.A.3.b, and spoils many of the clear signatures of OV excitation seen in the ideal centered case. Second, single-nanostructure measurements require more sophisticated techniques that, though available with current technology, face additional challenges when it comes to the excitation by OVs; these include the tight focusing and precise positioning of the beam to irradiate a single nanostructure out of an ensemble and align the singularity of the beam with the structure, and the readout of low signals obtained from nanostructures positioned close to the singularity.

3. Analytical models and numerical simulations

From a theoretician's point of view, common sense dictates that a new field should be explored from basic phenomena, which can be addressed by relatively simple analytical and numerical models. We have now reached a good understanding of particular systems, namely, bulk semiconductors, quantum rings, quantum dots, and microcavities; in other systems, our theoretical understanding is rudimentary. Many important ingredients that would render a more complete picture of the system under scrutiny are still to be incorporated. Sophisticated analytical and numerical models are necessary to guide experimental work and propose future applications.

Essential elements of material systems that have been considered in only a few cases are (i) the electron-electron interaction responsible for the formation of excitons and thus exciton polaritons, but also higher excitonic complexes such as biexcitons and trions; (ii) the electron-phonon interaction that drives relaxation and dephasing of electron populations and coherences but also creates new and efficient ways of excitation of nanostructures, such as by employing phonon-assisted transitions; (iii) phenomena related to impurities and crystal defects, which cause a loss of spatial coherence and a localization of electronic states but also provide new functionalities like single-photon emission; and (iv) the influence of temperature, which plays a key role in applications.

Specific to nanostructures, we are in need of a description beyond the envelope-function approximation. An assumption that underlies all our treatment is that of constant light field within the crystal unit cell [Eqs. (69a) and (69b)], an assumption supported by the order of magnitude difference in length scales of unit cell and far-field optical wavelengths. However, in Sec. VI.B.1 we argued that the phase singularity is an unavoidable inhomogeneity at all scales. Therefore, one wonders what would result from lifting the restriction imposed by Eqs. (69a) and (69b). This is indeed a search worth pursuing, although one not devoid of difficulties. The main one is the fact that the envelope-function approximation is an assumption of a similar sort: the so-called envelope part of the wave function is a constant within the unit cell. An additional complication is that the variation of fields on the subnanometer scales would render the basic assumption of macroscopic electromagnetic fields in media invalid (Jackson, 1999). Thus, a reexamination of the validity of Eqs. (69a) and (69b) requires a concomitant reexamination of the envelope-function approximation and macroscopic fields in the media.

Another possible improvement concerns a better description of the nanostructure geometry by including interfaces. The external OV driving field goes through layers of different geometries and compounds that perturb it to some extent before it reaches the active region, where the optical excitation of interest takes place. In addition to possibly unimportant

attenuation by other partially active layers, reflection and refraction of OVs result in distortion and displacement of the field by complex mechanisms such as the Goos-Hänchen and Imbert-Fedorov shifts (Novitsky and Barkovsky, 2008; Okuda and Sasada, 2008; Bliokh, Shadrivov, and Kivshar, 2009; Lusk, Siemens, and Quinteiro, 2019).

One can also improve the description of the driving field. This includes replacing the ideal Bessel beams with Bessel-Gaussian beams (Gori, Guattari, and Padovani, 1987; Li, Lee, and Wolf, 2004), accounting for the imperfections introduced by the experimental generation of beams [such as producing beams with unintended multiple-singularity components (Heckenberg *et al.*, 1992; Karimi *et al.*, 2007; Bekshaev and Karamoch, 2008)] or the use of multiple pulses. The addition of the interaction with the bath modes in the weak- and strong-coupling regimes reflects not only relaxation processes in matter (radiative recombination) but also the leakage of relevant modes outside cavities, etc.

The physics of optical vortices in microcavities treats fully quantum mechanically matter and light on an equal footing (Sec. IV.B). Somewhat similarly but in a semiclassical fashion, excitations in metal-dielectric interfaces solves the coupled dynamics of matter and electromagnetic fields (Sec. IV.C). For other systems, an extension to a description of the self-consistent problem of the mutual light-matter interaction is in order in systems embedded in cavities under the strong-coupling regime. In addition, a quantum mechanical description of light is also desirable, such as in situations with low fluence (a few photon case).

4. Structured light beyond Laguerre-Gauss and Bessel beams

Little is known about the interaction of condensed-matter systems with multiple-singularity OVs, and more general structured beams. Holtkemper *et al.* (2020) demonstrated theoretically that structured light can unveil details of the exciton wave function in QDs (Sec. IV.A.3.b). This work shows that new physics and applications can be expected out of the simplest case of single-singularity OVs. In particular, we expect that interesting research could arise from the study of Mathieu beams (Sec. II.D). We recall that these are the solutions of the Helmholtz equation in elliptical coordinates; Bessel beams are in a sense a particular case in which the ellipse collapses to a circle. Mathieu beams exhibit one or several singularities, whose location, number, and topological charge can be manipulated by adjusting the beam's parameters; see Fig. 3.

All these examples show that the topic of OV–condensed-matter interactions is open in many directions and a variety of interesting results can be expected from future experimental and theoretical work in the field.

ACKNOWLEDGMENTS

G. F. Q. R. thanks the U.S. agency Office of Naval Research Global for financial support through Grant No. N62909-18-1-2090, and the Argentine agency Agencia Nacional de Promoción Científica y Tecnológica for financial support through Grant No. PICT2016-1056. P. I. T. gratefully acknowledges the financial support through Project No. UBACyT 2018 20020170100711BA from the Universidad de Buenos Aires.

REFERENCES

Abbe, E., 1874, *Neue Apparate zur Bestimmung des Brechungs-und Zerstreuungsvermögens Fester und Flüssiger Körper* (Mauke's Verlag, Jena, Germany).
Abdalla, A. S., B. Zou, Y. Ren, T. Liu, and Y. Zhang, 2018, Opt. Express **26**, 22273.
Ablez, A., K. Toyoda, K. Miyamoto, and T. Omatsu, 2020, Appl. Phys. Express **13**, 062006.
Abrikosov, A. A., 1957, Zh. Eksp. Teor. Fiz. **32**, 1442 Sov. Phys. JETP **5**, 1174 (1957), http://www.jetp.ras.ru/cgi-bin/dn/e_005_06_1174.pdf].
Abrikosov, A. A., L. P. Gorkov, and I. E. Dzyaloshinski, 2012, *Methods of Quantum Field Theory in Statistical Physics* (Courier Corporation, North Chelmsford, MA).
Afanasev, A., C. E. Carlson, C. T. Schmiegelow, J. Schulz, F. Schmidt-Kaler, and M. Solyanik, 2018, New J. Phys. **20**, 023032.
Ahn, E. C., 2020, npj 2D Mater. Appl. **4**, 17.
Al-Amri, M. D., D. L. Andrews, and M. Babiker, 2021, in *Structured Light for Optical Communication*, Nanophotonics (Elsevier, New York), pp. v–x.
Albrecht, S., L. Reining, R. Del Sole, and G. Onida, 1998, Phys. Rev. Lett. **80**, 4510.
Allen, L., M. Babiker, W. K. Lai, and V. E. Lembessis, 1996, Phys. Rev. A **54**, 4259.
Allen, L., S. M. Barnett, and M. J. Padgett, 2003, *Optical Angular Momentum* (CRC Press, Boca Raton).
Allen, L., M. W. Beijersbergen, R. J. C. Spreeuw, and J. P. Woerdman, 1992, Phys. Rev. A **45**, 8185.
Allen, L., M. J. Padgett, and M. Babiker, 1999, Prog. Opt. **39**, 291.
Alperin, S. N., R. D. Niederriter, J. T. Gopinath, and M. E. Siemens, 2016, Opt. Lett. **41**, 5019.
Alpmann, C., R. Bowman, M. Woerdemann, M. Padgett, and C. Denz, 2010, Opt. Express **18**, 26084.
Ambrosio, A., L. Marrucci, F. Borbone, A. Roviello, and P. Maddalena, 2012, Nat. Commun. **3**, 989.
Anderson, N., and A. M. Arthurs, 1990, Int. J. Electron. **69**, 575.
Andreev, A. D., and E. P. O'Reilly, 2000, Phys. Rev. B **62**, 15851.
Andrews, D. L., 2008, *Structured Light and Its Applications: An Introduction to Phase-Structured Beams and Nanoscale Optical Forces* (Academic Press, New York).
Andrews, D. L., and M. Babiker, 2012, *The Angular Momentum of Light* (Cambridge University Press, Cambridge, England).
Andrews, D. L., L. C. Dávila Romero, and M. Babiker, 2004, Opt. Commun. **237**, 133.
Anoop, K. K., R. Fittipaldi, A. Rubano, X. Wang, D. Paparo, A. Vecchione, L. Marrucci, R. Bruzzese, and S. Amoruso, 2014, J. Appl. Phys. **116**, 113102.
Arakawa, Y., and S. Kako, 2006, Phys. Status Solidi A **203**, 3512.
Araoka, F., T. Verbiest, K. Clays, and A. Persoons, 2005, Phys. Rev. A **71**, 055401.
Arfken, G. B., and H. J. Weber, 2005, *Mathematical Methods for Physicists*, 6th ed. (Academic Press, New York).
Arikawa, T., S. Morimoto, and K. Tanaka, 2017, Opt. Express **25**, 13728.
Arlt, J., and K. Dholakia, 2000, Opt. Commun. **177**, 297.
Arnaut, H. H., and G. A. Barbosa, 2000, Phys. Rev. Lett. **85**, 286.
Arroyo-Camejo, S., M.-P. Adam, M. Besbes, J.-P. Hugonin, V. Jacques, J.-J. Greffet, J.-F. Roch, S. W. Hell, and F. Treussart, 2013, ACS Nano **7**, 10912.

Ashcroft, N. W., and N. D. Mermin, 1976, *Solid State Physics*, 1st ed. (Brooks/Cole, Pacific Grove, CA), p. 29.
Axt, V. M., and T. Kuhn, 2004, Rep. Prog. Phys. **67**, 433.
Babiker, M., D. L. Andrews, and V. E. Lembessis, 2019, J. Opt. **21**, 013001.
Babiker, M., C. R. Bennett, D. L. Andrews, and L. C. Dávila Romero, 2002, Phys. Rev. Lett. **89**, 143601.
Baibich, M. N., J. M. Broto, A. Fert, F. Nguyen Van Dau, F. Petroff, P. Etienne, G. Creuzet, A. Friederich, and J. Chazelas, 1988, Phys. Rev. Lett. **61**, 2472.
Ballentine, L. E., 2014, *Quantum Mechanics: A Modern Development* (World Scientific, Singapore).
Balzer, K., and M. Bonitz, 2013, *Nonequilibrium Green's Functions Approach to Inhomogeneous Systems* (Springer, Berlin).
Baranova, N. B., B. Ya. Zel'dovich, A. V. Mamaev, N. F. Pilipetsky, and V. V. Shkukov, 1981, Pis'ma Zh. Eksp. Teor. Fiz. **33**, 206 [JETP Lett. **33**, 195 (1981)].
Barnett, S. M., and L. Allen, 1994, Opt. Commun. **110**, 670.
Barnett, S. M., M. Babiker, and M. J. Padgett, 2017, Phil. Trans. R. Soc. A **375**, 20150444.
Barrigón, E., M. Heurlin, Z. Bi, B. Monemar, and L. Samuelson, 2019, Chem. Rev. **119**, 9170.
Basdevant, J.-L., and J. Rich, 2005, *Fundamentals in Nuclear Physics: From Nuclear Structure to Cosmology* (Springer Science+Business Media, New York).
Bassani, F., J. J. Forney, and A. Quattropani, 1977, Phys. Rev. Lett. **39**, 1070.
Bastard, G., 1988, *Wave Mechanics Applied to Semiconductor Heterostructures* (Les Éditions de Physique, Les Ulis, France).
Bekshaev, A. Y., and A. Karamoch, 2008, Opt. Commun. **281**, 1366.
Berkelbach, T. C., and D. R. Reichman, 2018, Annu. Rev. Condens. Matter Phys. **9**, 379.
Berkhout, G. C. G., and M. W. Beijersbergen, 2008, Phys. Rev. Lett. **101**, 100801.
Berkhout, G. C. G., M. P. J. Lavery, J. Courtial, M. W. Beijersbergen, and M. J. Padgett, 2010, Phys. Rev. Lett. **105**, 153601.
Berry, M. V., 2004, J. Opt. A **6**, 289.
Berry, M. V., M. R. Jeffrey, and M. Mansuripur, 2005, J. Opt. A **7**, 685.
Beth, R. A., 1936, Phys. Rev. **50**, 115.
Bhowmik, A., P. K. Mondal, S. Majumder, and B. Deb, 2016, Phys. Rev. A **93**, 063852.
Biasiol, G., and S. Heun, 2011, Phys. Rep. **500**, 117.
Binasch, G., P. Grünberg, F. Saurenbach, and W. Zinn, 1989, Phys. Rev. B **39**, 4828.
Bliokh, K. Y., M. A. Alonso, E. A. Ostrovskaya, and A. Aiello, 2010, Phys. Rev. A **82**, 063825.
Bliokh, K. Y., and F. Nori, 2015, Phys. Rep. **592**, 1.
Bliokh, K. Y., I. V. Shadrivov, and Y. S. Kivshar, 2009, Opt. Lett. **34**, 389.
Bloch, F., 1929, Z. Phys. **52**, 555.
Bluhm, H., N. C. Koshnick, J. A. Bert, M. E. Huber, and K. A. Moler, 2009, Phys. Rev. Lett. **102**, 136802.
Bock, M., J. Jahns, and R. Grunwald, 2012, Opt. Lett. **37**, 3804.
Bohm, D., and D. Pines, 1953, Phys. Rev. **92**, 609.
Borgh, M. O., G. Franchetti, J. Keeling, and N. G. Berloff, 2012, Phys. Rev. B **86**, 035307.
Boriskina, S., and N. I. Zheludev, 2014, *Singular and Chiral Nanoplasmonics* (CRC Press, Boca Raton).
Born, M., and E. Wolf, 2013, *Principles of Optics: Electromagnetic Theory of Propagation, Interference and Diffraction of Light* (Elsevier, New York).
Boulier, T., E. Cancellieri, N. D. Sangouard, Q. Glorieux, A. V. Kavokin, D. M. Whittaker, E. Giacobino, and A. Bramati, 2016, Phys. Rev. Lett. **116**, 116402.
Boyd, R. W., 2020, *Nonlinear Optics* (Academic Press, New York).
Boyle, R., 1661, *The Sceptical Chymist* (J. Calwell, London).
Bozinovic, N., Y. Yue, Y. Ren, M. Tur, P. Kristensen, H. Huang, A. E. Willner, and S. Ramachandran, 2013, Science **340**, 1545.
Bragg, W. H., and W. L. Bragg, 1913, Proc. R. Soc. A **88**, 428.
Breuer, H.-P., and F. Petruccione, 2002, *The Theory of Open Quantum Systems* (Oxford University Press, New York).
Brullot, W., M. K. Vanbel, T. Swusten, and T. Verbiest, 2016, Sci. Adv. **2**, e1501349.
Cai, X., J. Wang, M. J. Strain, B. Johnson-Morris, J. Zhu, M. Sorel, J. L. O'Brien, M. G. Thompson, and S. Yu, 2012, Science **338**, 363.
Cajori, F., 1899, *A History of Physics in Its Elementary Branches: Including the Evolution of Physical Laboratories* (MacMillan, London).
Cameron, K., A. F. Gibson, J. Giles, C. B. Hatch, M. F. Kimmitt, and S. Shafik, 1975, J. Phys. C **8**, 3137.
Cao, B., T. Grass, G. Solomon, and M. Hafezi, 2021, Phys. Rev. B **103**, L241301.
Cao, Y., Y. Fu, J.-H. Jiang, L. Gao, and Y. Xu, 2021, ACS Photonics **8**, 2027.
Carpentier, A. V., H. Michinel, J. R. Salgueiro, and D. Olivieri, 2008, Am. J. Phys. **76**, 916.
Castro Neto, A. H., F. Guinea, N. M. R. Peres, K. S. Novoselov, and A. K. Geim, 2009, Rev. Mod. Phys. **81**, 109.
Chang, S.-H., S. K. Gray, and G. C. Schatz, 2005, Opt. Express **13**, 3150.
Chatterjee, R., I. M. Pavlovetc, K. Aleshire, and M. Kuno, 2018, J. Phys. Chem. C **122**, 16443.
Chen, B., Y. Wei, T. Zhao, S. Liu, R. Su, B. Yao, Y. Yu, J. Liu, and X. Wang, 2021, Nat. Nanotechnol. **16**, 302.
Chen, R., H. Zhou, M. Moretti, X. Wang, and J. Li, 2020, IEEE Commun. Surv. Tutor. **22**, 840.
Chen, W. T., A. Y. Zhu, M. Khorasaninejad, Z. Shi, V. Sanjeev, and F. Capasso, 2017, Nano Lett. **17**, 3188.
Chen, X., C. Zou, Z. Gong, C. Dong, G. Guo, and F. Sun, 2015, Light Sci. Appl. **4**, e230.
Chen, Y., J. Gao, Z.-Q. Jiao, K. Sun, W.-G. Shen, L.-F. Qiao, H. Tang, X.-F. Lin, and X.-M. Jin, 2018, Phys. Rev. Lett. **121**, 233602.
Chow, W. W., and S. W. Koch, 1999, *Semiconductor-Laser Fundamentals: Physics of the Gain Materials* (Springer Science+Business Media, New York).
Citrin, D. S., 1994, IEEE J. Quantum Electron. **30**, 997.
Ciuti, C., P. Schwendimann, and A. Quattropani, 2001, Phys. Rev. B **63**, 041303.
Clayburn, N. B., J. L. McCarter, J. M. Dreiling, M. Poelker, D. M. Ryan, and T. J. Gay, 2013, Phys. Rev. B **87**, 035204.
Cohen, M. L., and J. R. Chelikowsky, 2012, *Electronic Structure and Optical Properties of Semiconductors*, Vol. 75 (Springer Science +Business Media, New York).
Cohen-Tannoudji, C., J. Dupont-Roc, and G. Grynberg, 1989, *Photons and Atoms: Introduction to Quantum Electrodynamics* (Wiley, New York).
Cohen-Tannoudji, C., J. Dupont-Roc, and G. Grynberg, 1998, *Atom-Photon Interactions: Basic Processes and Applications* (Wiley, New York).
Coullet, P., L. Gil, and F. Rocca, 1989, Opt. Commun. **73**, 403.
Courtial, J., K. Dholakia, L. Allen, and M. J. Padgett, 1997, Phys. Rev. A **56**, 4193.
Cundiff, S. T., 2008, Opt. Express **16**, 4639.
Cundiff, S. T., and S. Mukamel, 2013, Phys. Today **66**, No. 7, 44.

Cygorek, M., P. I. Tamborenea, and V. M. Axt, 2015, Phys. Rev. B **92**, 115301.
Dalgarno, A., and J. T. Lewis, 1956, Proc. Phys. Soc. London Sect. A **69**, 285.
Dalton, J., 1808, *A New System of Chemical Philosophy*, Vol. 1 (Bickerstaff, London).
Das, S., A. Bhowmik, K. Mukherjee, and S. Majumder, 2020, J. Phys. B **53**, 025302.
Das, S., J. A. Robinson, M. Dubey, H. Terrones, and M. Terrones, 2015, Annu. Rev. Mater. Res. **45**, 1.
Dávila Romero, L. C., D. L. Andrews, and M. Babiker, 2002, J. Opt. B **4**, S66.
De Morveau, G., A. L. Lavoisier, C. Berthollet, A. D. Fourcroy, and J. H. Hassenfratz, 1787, *Méthode de Nomenclature Chimique* (Chez Cuchet Libraire, Paris).
Deng, H., H. Haug, and Y. Yamamoto, 2010, Rev. Mod. Phys. **82**, 1489.
Deng, H., G. Weihs, D. Snoke, J. Bloch, and Y. Yamamoto, 2003, Proc. Natl. Acad. Sci. U.S.A. **100**, 15318.
Dennis, M. R., R. P. King, B. Jack, K. O'Holleran, and M. J. Padgett, 2010, Nat. Phys. **6**, 118.
Dennis, M. R., K. O'Holleran, and M. J. Padgett, 2009, Prog. Opt. **53**, 293.
Dexter, D. L., and R. S. Knox, 1965, *Excitons* (Interscience Publishers, New York).
Dirac, P. A. M., 1927, Proc. R. Soc. A **114**, 243, https://royalsocietypublishing.org/doi/pdf/10.1098/rspa.1927.0039?download=true.
DiVincenzo, D. P., 2000, Fortschr. Phys. **48**, 771.
Dominici, L., *et al.*, 2015, Sci. Adv. **1**, e1500807.
Dominici, L., *et al.*, 2018, Nat. Commun. **9**, 1467.
Dresselhaus, M., 2001, *Solid State Physics, Part II: Optical Properties of Solids*, Lecture Notes Vol. 17 (MIT Press, Cambridge, MA).
Drude, P., 1900, Ann. Phys. (Berlin) **306**, 566.
Drueppel, M., T. Deilmann, J. Noky, P. Marauhn, P. Krueger, and M. Rohlfing, 2018, Phys. Rev. B **98**, 155433.
Duc, H. T., T. Meier, and S. W. Koch, 2005, Phys. Rev. Lett. **95**, 086606.
Durnin, J., J. J. Miceli, Jr., and J. H. Eberly, 1987, Phys. Rev. Lett. **58**, 1499.
Dusanowski, L., S.-H. Kwon, C. Schneider, and S. Höfling, 2019, Phys. Rev. Lett. **122**, 173602.
Einstein, A., 1905, Ann. Phys. (Berlin) **322**, 132.
Elliott, R. J., 1957, Phys. Rev. **108**, 1384.
Farias, M. B., G. F. Quinteiro, and P. I. Tamborenea, 2013, Eur. Phys. J. B **86**, 432.
Fermi, E., 1950, *Nuclear Physics: A Course Given by Enrico Fermi at the University of Chicago* (University of Chicago Press, Chicago).
Fetter, A. L., and J. D. Walecka, 2012, *Quantum Theory of Many-Particle Systems* (Courier Corporation, North Chelmsford, MA).
Feynman, R., 1955, in *Progress in Low Temperature Physics*, Vol. 1, edited by C. J. Gorter (Elsevier, New York), pp. 17–53.
Feynman, R. P., 1982, Int. J. Theor. Phys. **21**, 467.
Fiori, G., F. Bonaccorso, G. Iannaccone, T. Palacios, D. Neumaier, A. Seabaugh, S. K. Banerjee, and L. Colombo, 2014, Nat. Nanotechnol. **9**, 768.
Florian, M., C. Gies, F. Jahnke, H. A. M. Leymann, and J. Wiersig, 2013, Phys. Rev. B **87**, 165306.
Fomin, V. M., 2014, Ed., *Physics of Quantum Rings*, NanoScience and Technology (Springer, New York).
Fong, C. F., Y. Ota, S. Iwamoto, and Y. Arakawa, 2018, Opt. Express **26**, 21219.
Foo, G., D. M. Palacios, and G. A. Swartzlander, 2005, Opt. Lett. **30**, 3308.
Forbes, A., 2017, Phil. Trans. R. Soc. A **375**, 20150436.
Forbes, K. A., and D. L. Andrews, 2018a, in *Complex Light and Optical Forces XII*, edited by E. J. Galvez, D. L. Andrews, and J. Glückstad, SPIE Proceedings Vol. 10549 (SPIE—International Society for Optics and Photonics, Bellingham, WA), p. 1054915.
Forbes, K. A., and D. L. Andrews, 2018b, Opt. Lett. **43**, 435.
Franke-Arnold, S., 2017, Phil. Trans. R. Soc. A **375**, 20150435.
Franke-Arnold, S., S. M. Barnett, M. J. Padgett, and L. Allen, 2002, Phys. Rev. A **65**, 033823.
Franz, W., 1958, Z. Naturforsch. **13A**, 484.
Frenkel, J., 1931, Phys. Rev. **37**, 17.
Fried, Z., 1973, Phys. Rev. A **8**, 2835.
Fujita, H., and M. Sato, 2017, Phys. Rev. B **95**, 054421.
Galindo, A., and M. A. Martin-Delgado, 2002, Rev. Mod. Phys. **74**, 347.
Garoli, D., P. Zilio, Y. Gorodetski, F. Tantussi, and F. De Angelis, 2016, Sci. Rep. **6**, 29547.
Ge, L., 2020, Science **368**, 707.
Ghosh Dastidar, M., S. Das, K. Mukherjee, and S. Majumder, 2022, Phys. Lett. A **421**, 127776.
Giammanco, F., A. Perona, P. Marsili, F. Conti, F. Fidecaro, S. Gozzini, and A. Lucchesini, 2017, Opt. Lett. **42**, 219.
Gibson, A. F., M. F. Kimmitt, and A. C. Walker, 1970, Appl. Phys. Lett. **17**, 75.
Gibson, A. F., and A. C. Walker, 1971, J. Phys. C **4**, 2209.
Gippius, N. A., I. A. Shelykh, D. D. Solnyshkov, S. S. Gavrilov, Y. G. Rubo, A. V. Kavokin, S. G. Tikhodeev, and G. Malpuech, 2007, Phys. Rev. Lett. **98**, 236401.
Gisin, N., and R. Thew, 2007, Nat. Photonics **1**, 165.
Glauber, R. J., 1963, Phys. Rev. **130**, 2529.
Golde, D., T. Meier, and S. W. Koch, 2008, Phys. Rev. B **77**, 075330.
Goldstein, H., 1980, *Classical Mechanics*, 2nd ed. (Addison-Wesley, Reading, MA).
Göppert-Mayer, M., 1931, Ann. Phys. (Berlin) **401**, 273.
Gori, F., G. Guattari, and C. Padovani, 1987, Opt. Commun. **64**, 491.
Gorodetski, Y., A. Niv, V. Kleiner, and E. Hasman, 2008, Phys. Rev. Lett. **101**, 043903.
Grier, D. G., 2003, Nature (London) **424**, 810.
Grinberg, A. A., 1970, Zh. Eksp. Teor. Fiz. **58**, 989 [J. Exp. Theor. Phys. **31**, 531 (1970), https://www.researchgate.net/publication/253592623_Theory_of_the_Photoelectric_and_Photomagnetic_Effect_Produce_by_Light_Pressure].
Guo, W.-P., *et al.*, 2020, Nano Lett. **20**, 2857.
Guo, Z., Z. Li, J. Zhang, K. Guo, F. Shen, Q. Zhou, and H. Zhou, 2017, Nanomaterials **7**, 405.
Gutiérrez-Vega, J. C., M. D. Iturbe-Castillo, and S. Chávez-Cerda, 2000, Opt. Lett. **25**, 1493.
Gutiérrez-Vega, J. C., R. M. Rodriguez-Dagnino, M. D. I. Castillo, and S. Chavez-Cerda, 2001, in *Optical Pulse and Beam Propagation III*, edited by Y. B. Band, SPIE Proceedings Vol. 4271 (SPIE—International Society for Optics and Photonics, Bellingham, WA), pp. 73–80.
Haken, H., 1976, *Quantum Field Theory of Solids. An Introduction* (North-Holland, Amsterdam).
Hamazaki, J., R. Morita, K. Chujo, Y. Kobayashi, S. Tanda, and T. Omatsu, 2010, Opt. Express **18**, 2144.
Hamilton, W. R., 1831, Trans. R. Ir. Acad., **17**, 1, https://www.jstor.org/stable/30078785?seq=1#metadata_info_tab_contents.
Haug, H., and A.-P. Jauho, 2008, *Quantum Kinetics in Transport and Optics of Semiconductors*, Vol. 2 (Springer, New York).

Haug, H., and S. W. Koch, 2009, *Quantum Theory of the Optical and Electronic Properties of Semiconductors*, 5th ed. (World Scientific, Singapore).
He, J., X. Wang, D. Hu, J. Ye, S. Feng, Q. Kan, and Y. Zhang, 2013, Opt. Express **21**, 20230.
Hecht, B., H. Bielefeldt, L. Novotny, Y. Inouye, and D. W. Pohl, 1996, Phys. Rev. Lett. **77**, 1889.
Heckenberg, N. R., R. McDuff, C. P. Smith, H. Rubinsztein-Dunlop, and M. J. Wegener, 1992, Opt. Quantum Electron. **24**, S951.
Heeres, R. W., and V. Zwiller, 2014, Nano Lett. **14**, 4598.
Henzler, P., *et al.*, 2021, Phys. Rev. Lett. **126**, 067402.
Herbst, M., M. Glanemann, V. M. Axt, and T. Kuhn, 2003, Phys. Rev. B **67**, 195305.
Hernández-García, C., J. Vieira, J. T. Mendonça, L. Rego, J. San Román, L. Plaja, P. R. Ribic, D. Gauthier, and A. Picón, 2017, Photonics **4**, 28.
Hernández-Hernández, R. J., R. A. Terborg, I. Ricardez-Vargas, and K. Volke-Sepúlveda, 2010, Appl. Opt. **49**, 6903.
Hess, O., and T. Kuhn, 1996, Phys. Rev. A **54**, 3347.
Hirohata, A., K. Yamada, Y. Nakatani, I.-L. Prejbeanu, B. Diény, P. Pirro, and B. Hillebrands, 2020, J. Magn. Magn. Mater. **509**, 166711.
Hohenberg, P., and W. Kohn, 1964, Phys. Rev. **136**, B864.
Holtkemper, M., G. F. Quinteiro, D. E. Reiter, and T. Kuhn, 2020, Phys. Rev. B **102**, 165315.
Holtkemper, M., G. F. Quinteiro, D. E. Reiter, and T. Kuhn, 2021, Phys. Rev. Research **3**, 013024.
Honold, A., L. Schultheis, J. Kuhl, and C. W. Tu, 1988, Appl. Phys. Lett. **52**, 2105.
Hopfield, J. J., 1958, Phys. Rev. **112**, 1555.
Hoshina, M., N. Yokoshi, and H. Ishihara, 2020, Opt. Express **28**, 14980.
Huang, K., 1963, *Statistical Mechanics* (Wiley, New York).
Huygens, C., 1690, *Oeuvres Completes XIX*, p. 1737.
Ibach, H., and H. Lüth, 2013, *Solid-State Physics: An Introduction to Principles of Materials Science* (Springer Science+Business Media, New York).
Ihn, T., 2010, *Semiconductor Nanostructures: Quantum States and Electronic Transport* (Oxford University Press, New York).
Inglot, M., V. K. Dugaev, J. Berakdar, E. Y. Sherman, and J. Barnaś, 2018, Appl. Phys. Lett. **112**, 231102.
Jacak, L., P. Hawrylak, and A. Wojs, 2013, *Quantum Dots* (Springer Science+Business Media, New York).
Jackson, J. D., 1999, *Classical Electrodynamics* (Wiley, New York).
Jarjour, A. F., R. A. Oliver, and R. A. Taylor, 2007, Philos. Mag. **87**, 2077.
Jaroszewicz, Z., A. Burvall, and A. T. Friberg, 2005, Opt. Photonics News **16**, 34.
Jauho, A. P., and K. Johnsen, 1996, Phys. Rev. Lett. **76**, 4576.
Jáuregui, R., 2004, Phys. Rev. A **70**, 033415.
Jeffries, G. D. M., J. S. Edgar, Y. Zhao, J. P. Shelby, C. Fong, and D. T. Chiu, 2007, Nano Lett. **7**, 415.
Jentschura, U. D., and V. G. Serbo, 2011, Phys. Rev. Lett. **106**, 013001.
Ji, Z., W. Liu, S. Krylyuk, X. Fan, Z. Zhang, A. Pan, L. Feng, A. Davydov, and R. Agarwal, 2020, Science **368**, 763.
Jiang, Y., Y. Cao, and X. Feng, 2020, J. Phys. D **53**, 303002.
Johnson, A., M. Siemens, G. Quinteiro, S. Sanguinetti, and S. Bietti, 2017, Bull. Am. Phys. Soc. **62**, G1.00048, http://meetings.aps.org/link/BAPS.2017.4CF.G1.48.
Jones, P. H., O. M. Marago, and G. Volpe, 2015, *Optical Tweezers: Principles and Applications* (Cambridge University Press, Cambridge, England).
Joschko, M., M. Woerner, T. Elsaesser, E. Binder, T. Kuhn, R. Hey, H. Kostial, and K. Ploog, 1997, Phys. Rev. Lett. **78**, 737.
Juman, G., M. Watabe, K. Miyamoto, and T. Omatsu, 2014, in *2014 Conference on Lasers and Electro-Optics (CLEO): Laser Science to Photonic Applications* (IEEE, New York), pp. 1–2.
Kadanoff, L. P., and G. Baym, 1962, *Quantum Statistical Mechanics: Green's Function Methods in Equilibrium and Nonequilibrium Problems* (Benjamin-Cummings Publishing, San Francisco).
Kaiser, T., D. Flamm, S. Schröter, and M. Duparré, 2009, Opt. Express **17**, 9347.
Kako, S., K. Hoshino, S. Iwamoto, S. Ishida, and Y. Arakawa, 2004, Appl. Phys. Lett. **85**, 64.
Kalt, H., and C. F. Klingshirn, 2019, *Semiconductor Optics 1: Linear Optical Properties of Semiconductors* (Springer, Berlin).
Karimi, E., G. Zito, B. Piccirillo, L. Marrucci, and E. Santamato, 2007, Opt. Lett. **32**, 3053.
Kasprzak, J., *et al.*, 2006, Nature (London) **443**, 409.
Kavokin, A., J. J. Baumberg, G. Malpuech, and F. P. Laussy, 2017, *Microcavities* (Oxford University Press, New York).
Kawata, S., M. Ohtsu, and M. Irie, 2001, *Near-Field Optics and Surface Plasmon Polaritons*, Vol. 81 (Springer Science+Business Media, New York).
Kazak, N. S., N. A. Khilo, and A. A. Ryzhevich, 1999, Quantum Electron. **29**, 1020.
Kazimierczuk, T., D. Fröhlich, S. Scheel, H. Stolz, and M. Bayer, 2014, Nature (London) **514**, 343.
Keldysh, L. V., 1958, Zh. Eksp. Teor. Fiz. **34**, 1138 [Sov. Phys. JETP **7**, 788 (1958), http://www.jetp.ras.ru/cgi-bin/dn/e_007_05_0788.pdf].
Keldysh, L. V., 1964, Zh. Eksp. Teor. Fiz. **47**, 1515 [Sov. Phys. JETP **20**, 1018 (1965), http://jetp.ras.ru/cgi-bin/dn/e_020_04_1018.pdf].
Keller, J., A. Schönle, and S. W. Hell, 2007, Opt. Express **15**, 3361.
Kelly, M. J., and R. J. Nicholas, 1985, Rep. Prog. Phys. **48**, 1699.
Kerber, R. M., J. M. Fitzgerald, X. Xiao, S. S. Oh, S. A. Maier, V. Giannini, and D. E. Reiter, 2018, New J. Phys. **20**, 095005.
Kerridge-Johns, W. R., 2018, "Diode-pumped Alexandrite laser development and vortex mode generation," Ph.D. thesis (Imperial College London).
Khitrova, G., H. M. Gibbs, F. Jahnke, M. Kira, and S. W. Koch, 1999, Rev. Mod. Phys. **71**, 1591.
Kikkawa, J., and D. Awschalom, 1999, Nature (London) **397**, 139.
Kim, H., J. Park, S.-W. Cho, S.-Y. Lee, M. Kang, and B. Lee, 2010, Nano Lett. **10**, 529.
Kira, M., F. Jahnke, W. Hoyer, and S. W. Koch, 1999, Prog. Quantum Electron. **23**, 189.
Kittel, C., 1987, *Quantum Theory of Solids*, 2nd ed. (John Wiley & Sons, New York).
Kleemans, N. A. J. M., *et al.*, 2007, Phys. Rev. Lett. **99**, 146808.
Kobayashi, S., C. Jiang, T. Kawazu, and H. Sakaki, 2004, Jpn. J. Appl. Phys. **43**, L662.
Kobe, D. H., 1978, Phys. Rev. Lett. **40**, 538.
Koch, M., D. Weber, J. Feldmann, E. O. Göbel, T. Meier, A. Schulze, P. Thomas, S. Schmitt-Rink, and K. Ploog, 1993, Phys. Rev. B **47**, 1532.
Koch, S. W., N. Peyghambarian, and M. Lindberg, 1988, J. Phys. C **21**, 5229.
Kohn, W., and L. J. Sham, 1965, Phys. Rev. **140**, A1133.
Koksal, K., V. E. Lembessis, J. Yuan, and M. Babiker, 2020, J. Opt. Soc. Am. B **37**, 2570.
Koksal, K., V. E. Lembessis, J. Yuan, and M. Babiker, 2019, J. Opt. **21**, 104002.
Köksal, K., and J. Berakdar, 2012, Phys. Rev. A **86**, 063812.
Köksal, K., and F. Koç, 2017a, Comput. Theor. Chem. **1099**, 203.
Köksal, K., and F. Koç, 2017b, Comput. Theor. Chem. **1105**, 27.

Konzelmann, A. M., S. O. Krüger, and H. Giessen, 2019, Phys. Rev. B **100**, 115308.
Korenev, B. G., 2002, *Bessel Functions and Their Applications* (CRC Press, Boca Raton).
Kotlyar, V. V., A. A. Almazov, S. N. Khonina, V. A. Soifer, H. Elfstrom, and J. Turunen, 2005, J. Opt. Soc. Am. A **22**, 849.
Krasnok, A., S. Lepeshov, and A. Alú, 2018, Opt. Express **26**, 15972.
Kraus, M., J. Wätzel, and J. Berakdar, 2018, Opt. Commun. **427**, 390.
Krenn, M., M. Malik, M. Erhard, and A. Zeilinger, 2017, Phil. Trans. R. Soc. A **375**, 20150442.
Kroutvar, M., Y. Ducommun, D. Heiss, M. Bichler, D. Schuh, G. Abstreiter, and J. J. Finley, 2004, Nature (London) **432**, 81.
Krügel, A., A. Vagov, V. M. Axt, and T. Kuhn, 2007, Phys. Rev. B **76**, 195302.
Kugler, M., *et al.*, 2011, Phys. Rev. B **84**, 085327.
Kuhn, T., D. E. Reiter, and G. F. Quinteiro, 2015, J. Phys. Conf. Ser. **647**, 012012.
Kwon, M.-S., B. Y. Oh, S.-H. Gong, J.-H. Kim, H. K. Kang, S. Kang, J. D. Song, H. Choi, and Y.-H. Cho, 2019, Phys. Rev. Lett. **122**, 045302.
Lagoudakis, K. G., T. Ostatnický, A. V. Kavokin, Y. G. Rubo, R. André, and B. Deveaud-Plédran, 2009, Science **326**, 974.
Lagoudakis, K. G., M. Wouters, M. Richard, A. Baas, I. Carusotto, R. André, L. S. Dang, and B. Deveaud-Plédran, 2008, Nat. Phys. **4**, 706.
Lamb, Jr., W. E., R. R. Schlicher, and M. O. Scully, 1987, Phys. Rev. A **36**, 2763.
Lavery, M. P. J., F. C. Speirits, S. M. Barnett, and M. J. Padgett, 2013, Science **341**, 537.
Lavoisier, A., 1793, *Traité Élémentaire de Chimie, 1* (Chez Cuchet Libraire, Paris).
Lax, M., W. H. Louisell, and W. B. McKnight, 1975, Phys. Rev. A **11**, 1365.
Lee, H.-I., and J. Mok, 2016, Pac. J. Math. Ind. **8**, 4.
Lee, J., Y. Arita, S. Toyoshima, K. Miyamoto, P. Panagiotopoulos, E. M. Wright, K. Dholakia, and T. Omatsu, 2018, ACS Photonics **5**, 4156.
Leosson, K., J. R. Jensen, W. Langbein, and J. M. Hvam, 2000, Phys. Rev. B **61**, 10322.
Lerario, G., *et al.*, 2017, Nat. Phys. **13**, 837.
Li, C.-F., 2009, Phys. Rev. A **80**, 063814.
Li, H., D. B. Phillips, X. Wang, Y.-L. D. Ho, L. Chen, X. Zhou, J. Zhu, S. Yu, and X. Cai, 2015, Optica **2**, 547.
Li, Y., H. Lee, and E. Wolf, 2004, J. Opt. Soc. Am. A **21**, 640.
Li, Z., Y. Li, T. Han, X. Wang, Y. Yu, B. Tay, Z. Liu, and Z. Fang, 2017, ACS Nano **11**, 1165.
Liao, S.-K., *et al.*, 2018, Phys. Rev. Lett. **120**, 030501.
Liew, T. C. H., and I. A. Shelykh, 2009, Phys. Rev. B **80**, 161303.
Lindberg, M., R. Binder, and S. Koch, 1992, Phys. Rev. A **45**, 1865.
Lindberg, M., and S. W. Koch, 1988, Phys. Rev. B **38**, 3342.
Lindblad, G., 1976, Commun. Math. Phys. **48**, 119.
Liu, G., D. W. Snoke, A. Daley, L. N. Pfeiffer, and K. West, 2015, Proc. Natl. Acad. Sci. U.S.A. **112**, 2676.
Liu, K., N. Maccaferri, Y. Shen, X. Li, R. P. Zaccaria, X. Zhang, Y. Gorodetski, and D. Garoli, 2020, Opt. Lett. **45**, 823.
Liu, Z., J. M. Steele, W. Srituravanich, Y. Pikus, C. Sun, and X. Zhang, 2005, Nano Lett. **5**, 1726.
Lloyd, H., 1833, London Edinburgh Dublin Philos. Mag. J. Sci. **2**, 112.
Löffler, W., D. J. Broer, and J. P. Woerdman, 2011, Phys. Rev. A **83**, 065801.
Loudon, R., 2003, Phys. Rev. A **68**, 013806.
Lu, W., and Y. Fu, 2018, *Spectroscopy of Semiconductors* (Springer, Berlin).
Lusk, M. T., M. Siemens, and G. F. Quinteiro, 2019, J. Opt. **21**, 015601.
Ma, X., B. Berger, M. Aßmann, R. Driben, T. Meier, C. Schneider, S. Höfling, and S. Schumacher, 2020, Nat. Commun. **11**, 897.
Maier, S. A., 2007, *Plasmonics: Fundamentals and Applications* (Springer Science+Business Media, New York).
Maiman, T. H., 1960, Nature (London) **187**, 493.
Mair, A., A. Vaziri, G. Weihs, and A. Zeilinger, 2001, Nature (London) **412**, 313.
Mak, K. F., C. Lee, J. Hone, J. Shan, and T. F. Heinz, 2010, Phys. Rev. Lett. **105**, 136805.
Mandel, L., 1958, Proc. Phys. Soc. London **72**, 1037.
Maragò, O. M., P. H. Jones, P. G. Gucciardi, G. Volpe, and A. C. Ferrari, 2013, Nat. Nanotechnol. **8**, 807.
Martelli, F., A. Polimeni, A. Patanè, M. Capizzi, P. Borri, M. Gurioli, M. Colocci, A. Bosacchi, and S. Franchi, 1996, Phys. Rev. B **53**, 7421.
Martin, J. D., 2019, Phys. Today **72**, No. 1, 30.
Masajada, J., and B. Dubik, 2001, Opt. Commun. **198**, 21.
Mathevet, R., B. V. de Lesegno, L. Pruvost, and G. L. J. A. Rikken, 2013, Opt. Express **21**, 3941.
Mathieu, É., 1868, J. Math. Pures Appl. **13**, 137, https://eudml.org/doc/234720.
Matthews, M. R., B. P. Anderson, P. C. Haljan, D. S. Hall, C. E. Wieman, and E. A. Cornell, 1999, Phys. Rev. Lett. **83**, 2498.
Matula, O., A. G. Hayrapetyan, V. G. Serbo, A. Surzhykov, and S. Fritzsche, 2013, J. Phys. B **46**, 205002.
Maxwell, J. C., 1865, Phil. Trans. R. Soc. London **155**, 459.
Meier, F., and B. P. Zakharchenya, 2012, *Optical Orientation* (Elsevier, New York).
Mendeleev, D., 1869, Z. Chem. **12**, 405.
Miao, P., Z. Zhang, J. Sun, W. Walasik, S. Longhi, N. M. Litchinitser, and L. Feng, 2016, Science **353**, 464.
Michler, P., A. Kiraz, C. Becher, W. V. Schoenfeld, P. M. Petroff, L. Zhang, E. Hu, and A. Imamoglu, 2000, Science **290**, 2282.
Mie, G., 1908, Ann. Phys. (Berlin) **330**, 377.
Mignaco, J. A., 2001, Braz. J. Phys. **31**, 235.
Mike, P., L. Z. Szabó, and P. Földi, 2018, J. Russ. Laser Res. **39**, 465.
Mills, M., 2011, IEEE Ann. Hist. Comput. **33**, 24.
Miró, P., M. Audiffred, and T. Heine, 2014, Chem. Soc. Rev. **43**, 6537.
Mohammadi, S. M., L. K. S. Daldorff, K. Forozesh, B. Thidé, J. E. S. Bergman, B. Isham, R. Karlsson, and T. D. Carozzi, 2010, Radio Sci. **45**, RS4007.
Mondal, P. K., B. Deb, and S. Majumder, 2014, Phys. Rev. A **89**, 063418.
Monteiro, P. B., P. A. M. Neto, and H. M. Nussenzveig, 2009, Phys. Rev. A **79**, 033830.
Moriarty, P., 2001, Rep. Prog. Phys. **64**, 297.
Mukherjee, K., S. Majumder, P. K. Mondal, and B. Deb, 2018, J. Phys. B **51**, 015004.
Nechayev, S., J. S. Eismann, G. Leuchs, and P. Banzer, 2019, Phys. Rev. B **99**, 075155.
Nerkararyan, S., K. Nerkararyan, N. Janunts, and T. Pertsch, 2010, Phys. Rev. B **82**, 245405.
Newton, I., 1672, Phil. Trans. R. Soc. London **6**, 3075.
Ni, J., C. Wang, C. Zhang, Y. Hu, L. Yang, Z. Lao, B. Xu, J. Li, D. Wu, and J. Chu, 2017, Light Sci. Appl. **6**, e17011.
Nikitine, S., 1969, in *Optical Properties of Solids*, edited by S. Nudelman and S. S. Mitra (Springer, Boston), p. 197.

Nivas, J. J. J., H. Shutong, K. K. Anoop, A. Rubano, R. Fittipaldi, A. Vecchione, D. Paparo, L. Marrucci, R. Bruzzese, and S. Amoruso, 2015, Opt. Lett. **40**, 4611.
Nobahar, D., K. Hajisharifi, and H. Mehdian, 2019, Opt. Laser Technol. **117**, 165.
Nolte, S., C. Momma, H. Jacobs, A. Tünnermann, B. N. Chichkov, B. Wellegehausen, and H. Welling, 1997, J. Opt. Soc. Am. B **14**, 2716.
Novitsky, A. V., and L. M. Barkovsky, 2008, J. Opt. A **10**, 075006.
Novoselov, K. S., 2011, Rev. Mod. Phys. **83**, 837.
Novoselov, K. S., A. K. Geim, S. V. Morozov, D. Jiang, Y. Zhang, S. V. Dubonos, I. V. Grigorieva, and A. A. Firsov, 2004, Science **306**, 666.
Novotny, L., and B. Hecht, 2006, *Principles of Nano-Optics* (Cambridge University Press, New York).
Noyan, M. A., and J. M. Kikkawa, 2015, Appl. Phys. Lett. **107**, 032406.
Nye, J. F., and M. V. Berry, 1974, Proc. R. Soc. A **336**, 165, https://www.jstor.org/stable/78498.
Ohno, T., and S. Miyanishi, 2006, Opt. Express **14**, 6285.
O'Holleran, K., M. J. Padgett, and M. R. Dennis, 2006, Opt. Express **14**, 3039.
Okuda, H., and H. Sasada, 2008, J. Opt. Soc. Am. A **25**, 881.
Omatsu, T., K. Chujo, K. Miyamoto, M. Okida, K. Nakamura, N. Aoki, and R. Morita, 2010, Opt. Express **18**, 17967.
Omatsu, T., K. Miyamoto, K. Toyoda, R. Morita, Y. Arita, and K. Dholakia, 2019, Adv. Opt. Mater. **7**, 1801672.
Onida, G., L. Reining, and A. Rubio, 2002, Rev. Mod. Phys. **74**, 601.
Oosterbeek, R. N., S. Ashforth, O. Bodley, and M. C. Simpson, 2018, Opt. Express **26**, 34558.
Otte, E., and C. Denz, 2020, Appl. Phys. Rev. **7**, 041308.
Pabon, D. O., S. A. Ledesma, G. F. Quinteiro, and M. G. Capeluto, 2017, Appl. Opt. **56**, 8048.
Padgett, M., J. Courtial, and L. Allen, 2004, Phys. Today **57**, No. 5, 35.
Padgett, M. J., and L. Allen, 2002, J. Opt. B **4**, S17.
Pan, J., Y. Shen, Z. Wan, X. Fu, H. Zhang, and Q. Liu, 2020, Phys. Rev. Applied **14**, 044048.
Parvez, K., 2019, in *Biomedical Applications of Graphene and 2D Nanomaterials* (Elsevier, New York), pp. 1–25.
Patton, B., W. Langbein, U. Woggon, L. Maingault, and H. Mariette, 2006, Phys. Rev. B **73**, 235354.
Persuy, D., M. Ziegler, O. Crégut, K. Kheng, M. Gallart, B. Hönerlage, and P. Gilliot, 2015, Phys. Rev. B **92**, 115312.
Peshkov, A. A., S. Fritzsche, and A. Surzhykov, 2015, Phys. Rev. A **92**, 043415.
Peshkov, A. A., D. Seipt, A. Surzhykov, and S. Fritzsche, 2017, Phys. Rev. A **96**, 023407.
Peshkov, A., A. Volotka, A. Surzhykov, and S. Fritzsche, 2018, Phys. Rev. A **97**, 023802.
Phelan, C. F., D. P. O'Dwyer, Y. P. Rakovich, J. F. Donegan, and J. G. Lunney, 2009, Opt. Express **17**, 12891.
Pigeon, S., I. Carusotto, and C. Ciuti, 2011, Phys. Rev. B **83**, 144513.
Planck, M., 1900, Verh. Dtsch. Phys. Ges. **2**, 202.
Portolan, S., O. Di Stefano, S. Savasta, F. Rossi, and R. Girlanda, 2008, Phys. Rev. B **77**, 195305.
Power, E. A., and S. Zienau, 1959, Phil. Trans. R. Soc. A **251**, 427.
Purcell, E. M., 1946, Proc. Am. Phys. Soc. **69**, 681.
Quinteiro, G. F., 2008, Phys. Rev. B **77**, 075301.
Quinteiro, G. F., 2010, Europhys. Lett. **91**, 27002.
Quinteiro, G. F., and J. Berakdar, 2009, Opt. Express **17**, 20465.
Quinteiro, G. F., P. Dmitruk, and A. A. Aligia, 2012, Phys. Rev. B **86**, 035329.
Quinteiro, G. F., J. Fernández-Rossier, and C. Piermarocchi, 2006, Phys. Rev. Lett. **97**, 097401.
Quinteiro, G. F., P. Grinberg, and C. T. Schmiegelow, 2019, in *Proceedings of the Conference on Lasers and Electro-Optics (CLEO), San Jose, 2019* (Optical Society of America, Washington, DC), p. JTu2A.19.
Quinteiro, G. F., and T. Kuhn, 2014, Phys. Rev. B **90**, 115401.
Quinteiro, G. F., and T. Kuhn, 2015, in *Proceedings of the Conference on Lasers and Electro-Optics (CLEO), San Jose, 2015* (Optical Society of America, Washington, DC), p. FW1E.8.
Quinteiro, G. F., A. O. Lucero, and P. I. Tamborenea, 2010, J. Phys. Condens. Matter **22**, 505802.
Quinteiro, G. F., and C. Piermarocchi, 2005, Phys. Rev. B **72**, 045334.
Quinteiro, G. F., D. E. Reiter, and T. Kuhn, 2015, Phys. Rev. A **91**, 033808.
Quinteiro, G. F., D. E. Reiter, and T. Kuhn, 2017a, J. Phys. Conf. Ser. **906**, 012014.
Quinteiro, G. F., D. E. Reiter, and T. Kuhn, 2017b, Phys. Rev. A **95**, 012106.
Quinteiro, G. F., F. Schmidt-Kaler, and C. T. Schmiegelow, 2017, Phys. Rev. Lett. **119**, 253203.
Quinteiro, G. F., C. T. Schmiegelow, D. E. Reiter, and T. Kuhn, 2019, Phys. Rev. A **99**, 023845.
Quinteiro, G. F., and P. I. Tamborenea, 2009a, in *Proceedings of the European Quantum Electronics Conference, Munich, 2009* (Optical Society of America, Washington, DC), p. JSIII2_5.
Quinteiro, G. F., and P. I. Tamborenea, 2009b, Phys. Rev. B **79**, 155450.
Quinteiro, G. F., and P. I. Tamborenea, 2009c, Europhys. Lett. **85**, 47001.
Quinteiro, G. F., and P. I. Tamborenea, 2010, Phys. Rev. B **82**, 125207.
Quinteiro, G. F., P. I. Tamborenea, and J. Berakdar, 2011, Opt. Express **19**, 26733.
Ranjan, V., G. Allan, C. Priester, and C. Delerue, 2003, Phys. Rev. B **68**, 115305.
Räsänen, E., A. Castro, J. Werschnik, A. Rubio, and E. K. U. Gross, 2007, Phys. Rev. Lett. **98**, 157404.
Reimann, S. M., and M. Manninen, 2002, Rev. Mod. Phys. **74**, 1283.
Reiter, D., M. Glanemann, V. M. Axt, and T. Kuhn, 2006, Phys. Rev. B **73**, 125334.
Reiter, D., M. Glanemann, V. M. Axt, and T. Kuhn, 2007, Phys. Rev. B **75**, 205327.
Ren, X., A. Liu, C. Zou, L. Wang, Y. Cai, F. Sun, G. Guo, and G. Guo, 2011, Appl. Phys. Lett. **98**, 201113.
Ritsch-Marte, M., 2017, Phil. Trans. R. Soc. A **375**, 20150437.
Rohlfing, M., and S. G. Louie, 1998, Phys. Rev. Lett. **81**, 2312.
Rosales Guzmán, C. G., 2015, "Photonic applications based on the use of structured light," Ph.D. thesis (Universitat Politècnica de Catalunya).
Rosati, R., R. C. Iotti, F. Dolcini, and F. Rossi, 2014, Phys. Rev. B **90**, 125140.
Rosencher, E., B. Vinter, and B. F. Levine, 2012, *Intersubband Transitions in Quantum Wells*, Vol. 288 (Springer Science+Business Media, New York).
Rossi, F., 2011, *Theory of Semiconductor Quantum Devices: Microscopic Modeling and Simulation Strategies* (Springer Science +Business Media, New York).
Rossi, F., and T. Kuhn, 2002, Rev. Mod. Phys. **74**, 895.
Rubano, A., F. Cardano, B. Piccirillo, and L. Marrucci, 2019, J. Opt. Soc. Am. B **36**, D70.
Rubo, Y. G., 2007, Phys. Rev. Lett. **99**, 106401.
Sakai, K., K. Nomura, T. Yamamoto, T. Omura, and K. Sasaki, 2016, Sci. Rep. **6**, 34967.

Salomaa, M. M., and G. E. Volovik, 1987, Rev. Mod. Phys. **59**, 533.
Samad, R. E., S. L. Baldochi, and N. D. Vieira, Jr., 2008, Appl. Opt. **47**, 920.
Sanvitto, D., *et al.*, 2011, Nat. Photonics **5**, 610.
Savona, V., C. Piermarocchi, A. Quattropani, P. Schwendimann, and F. Tassone, 1999, Phase Transitions **68**, 169.
Savona, V., C. Piermarocchi, A. Quattropani, F. Tassone, and P. Schwendimann, 1997, Phys. Rev. Lett. **78**, 4470.
Sbierski, B., G. F. Quinteiro, and P. I. Tamborenea, 2013, J. Phys. Condens. Matter **25**, 385301.
Scheuer, J., and M. Orenstein, 1999, Science **285**, 230.
Schiff, L. I., 1955, *Quantum Mechanics* (McGraw-Hill, New York).
Schilp, J., T. Kuhn, and G. Mahler, 1994, Phys. Rev. B **50**, 5435.
Schimpf, C., M. Reindl, D. Huber, B. Lehner, S. F. Covre Da Silva, S. Manna, M. Vyvlecka, P. Walther, and A. Rastelli, 2021, Sci. Adv. **7**, eabe8905.
Schmidt, O. A., C. Schulze, D. Flamm, R. Brüning, T. Kaiser, S. Schröter, and M. Duparré, 2011, Opt. Express **19**, 6741.
Schmiegelow, C. T., J. Schulz, H. Kaufmann, T. Ruster, U. G. Poschinger, and F. Schmidt-Kaler, 2016, Nat. Commun. **7**, 12998.
Schneider, C., *et al.*, 2013, Nature (London) **497**, 348.
Scholz-Marggraf, H. M., S. Fritzsche, V. G. Serbo, A. Afanasev, and A. Surzhykov, 2014, Phys. Rev. A **90**, 013425.
Schulze, D., A. Thakur, A. S. Moskalenko, and J. Berakdar, 2017, Ann. Phys. (Berlin) **529**, 1600379.
Schwiete, G., and Y. Oreg, 2009, Phys. Rev. Lett. **103**, 037001.
Scully, M. O., and M. S. Zubairy, 1997, *Quantum Optics* (Cambridge University Press, Cambridge, England).
Seghilani, M. S., M. Myara, M. Sellahi, L. Legratiet, I. Sagnes, G. Beaudoin, P. Lalanne, and A. Garnache, 2016, Sci. Rep. **6**, 38156.
Serabyn, E., D. Mawet, and R. Burruss, 2010, Nature (London) **464**, 1018.
Serbo, V. G., A. Surzhykov, and A. Volotka, 2022, Ann. Phys. (Berlin) **534**, 2100199.
Shah, J., 1999, *Ultrafast Spectroscopy of Semiconductors and Semiconductor Nanostructures* (Springer, Berlin).
Shalygin, V. A., *et al.*, 2007, JETP Lett. **84**, 570.
Shelykh, I. A., Y. G. Rubo, G. Malpuech, D. D. Solnyshkov, and A. Kavokin, 2006, Phys. Rev. Lett. **97**, 066402.
Shelykh, I. A., A. V. Kavokin, and G. Malpuech, 2005, Phys. Status Solidi B **242**, 2271.
Shelykh, I. A., A. V. Kavokin, Y. G. Rubo, T. Liew, and G. Malpuech, 2010, Semicond. Sci. Technol. **25**, 013001.
Shen, Y., X. Wang, Z. Xie, C. Min, X. Fu, Q. Liu, M. Gong, and X. Yuan, 2019, Light Sci. Appl. **8**, 90.
Shi, L., L. Lindwasser, W. Wang, R. Alfano, and A. Rodríguez-Contreras, 2017, J. Biophoton. **10**, 1756.
Shigematsu, K., K. Yamane, R. Morita, and Y. Toda, 2016, Phys. Rev. B **93**, 045205.
Shinde, P. V., and M. K. Singh, 2019, in *Fundamentals and Sensing Applications of 2D Materials* (Elsevier, New York), pp. 91–143.
Shintani, K., K. Taguchi, Y. Tanaka, and Y. Kawaguchi, 2016, Phys. Rev. B **93**, 195415.
Shree, S., I. Paradisanos, X. Marie, C. Robert, and B. Urbaszek, 2021, *Guide to Optical Spectroscopy of Layered Semiconductors*, Vol. 3 (Springer Nature, London).
Siegman, A. E., 1990, *Lasers* (University Science Books, Melville, NY).
Sigurdsson, H., O. A. Egorov, X. Ma, I. A. Shelykh, and T. C. H. Liew, 2014, Phys. Rev. B **90**, 014504.
Simbulan, K. B., *et al.*, 2021, ACS Nano **15**, 3481.
Solyanik-Gorgone, M., and A. Afanasev, 2019, Phys. Rev. B **99**, 035204.
Solyanik-Gorgone, M., A. Afanasev, C. E. Carlson, C. T. Schmiegelow, and F. Schmidt-Kaler, 2019, J. Opt. Soc. Am. B **36**, 565.
Sommerfeld, A., 1928, Z. Phys. **47**, 1.
Sordillo, L. A., S. Mamani, M. Sharonov, and R. R. Alfano, 2019, Appl. Phys. Lett. **114**, 041104.
Sotier, F., T. Thomay, T. Hanke, J. Korger, S. Mahapatra, A. Frey, K. Brunner, R. Bratschitsch, and A. Leitenstorfer, 2009, Nat. Phys. **5**, 352.
Spektor, G., *et al.*, 2017, Science **355**, 1187.
Splendiani, A., L. Sun, Y. Zhang, T. Li, J. Kim, C.-Y. Chim, G. Galli, and F. Wang, 2010, Nano Lett. **10**, 1271.
Steane, A., 1998, Rep. Prog. Phys. **61**, 117.
Stevenson, R. M., R. J. Young, P. Atkinson, K. Cooper, D. A. Ritchie, and A. J. Shields, 2006, Nature (London) **439**, 179.
Strinati, G., 1988, Riv. Nuovo Cimento Soc. Ital. Fis. **11**, 1.
Suárez, F., D. Granados, M. L. Dotor, and J. M. Garcia, 2004, Nanotechnology **15**, S126.
Sudarshan, E. C. G., 1963, Phys. Rev. Lett. **10**, 277.
Surzhykov, A., D. Seipt, V. G. Serbo, and S. Fritzsche, 2015, Phys. Rev. A **91**, 013403.
Syubaev, S., A. Zhizhchenko, A. Kuchmizhak, A. Porfirev, E. Pustovalov, O. Vitrik, Y. Kulchin, S. Khonina, and S. Kudryashov, 2017, Opt. Express **25**, 10214.
Syubaev, S., A. Zhizhchenko, O. Vitrik, A. Porfirev, S. Fomchenkov, S. Khonina, S. Kudryashov, and A. Kuchmizhak, 2019, Appl. Surf. Sci. **470**, 526.
Tabosa, J. W. R., and D. V. Petrov, 1999, Phys. Rev. Lett. **83**, 4967.
Takagahara, T., 1989, J. Lumin. **44**, 347.
Takahashi, H. T., I. Proskurin, and J.-i. Kishine, 2018, J. Phys. Soc. Jpn. **87**, 113703.
Takahashi, H. T., I. Proskurin, and J.-i. Kishine, 2019, arXiv:1904.03083.
Tamburini, F., B. Thidé, G. Molina-Terriza, and G. Anzolin, 2011, Nat. Phys. **7**, 195.
Thidé, B., F. Tamburini, H. Then, C. G. Someda, and R. A. Ravanelli, 2014, arXiv:1410.4268.
Thidé, B., H. Then, J. Sjöholm, K. Palmer, J. Bergman, T. D. Carozzi, Y. N. Istomin, N. H. Ibragimov, and R. Khamitova, 2007, Phys. Rev. Lett. **99**, 087701.
Tikhonova, O. V., and E. N. Voronina, 2022, J. Phys. Condens. Matter **34**, 065302.
Toledo-Solano, M., M. E. Mora-Ramos, A. Figueroa, and Y. G. Rubo, 2014, Phys. Rev. B **89**, 035308.
Tong, C., S. F. Yoon, and L. Wang, 2012, Nanoscale Res. Lett. **7**, 520.
Torres, J. P., and L. Torner, 2011, Eds., *Twisted Photons: Application of Light with Orbital Angular Momentum* (Wiley-VCH, Weinheim).
Toyoda, K., K. Miyamoto, N. Aoki, R. Morita, and T. Omatsu, 2012, Nano Lett. **12**, 3645.
Tsakiris, N., K. K. Anoop, G. Ausanio, M. Gill-Comeau, R. Bruzzese, S. Amoruso, and L. J. Lewis, 2014, J. Appl. Phys. **115**, 243301.
Tsesses, S., K. Cohen, E. Ostrovsky, B. Gjonaj, and G. Bartal, 2019, Nano Lett. **19**, 4010.
Tsintzos, S. I., N. T. Pelekanos, G. Konstantinidis, Z. Hatzopoulos, and P. G. Savvidis, 2008, Nature (London) **453**, 372.
Turpin, A., Y. V. Loiko, T. K. Kalkandjiev, and J. Mompart, 2016, Laser Photonics Rev. **10**, 750.
Ueno, Y., Y. Toda, S. Adachi, R. Morita, and T. Tawara, 2009, Opt. Express **17**, 20567.
Vagov, A., M. D. Croitoru, M. Glässl, V. M. Axt, and T. Kuhn, 2011, Phys. Rev. B **83**, 094303.

Van Enk, S., 1994, Quantum Opt. **6**, 445.
Vänskä, O., M. Kira, I. Tittonen, and S. W. Koch, 2011, Phys. Rev. B **84**, 165317.
Vasilieva, O. F., A. P. Zingan, and P. I. Khadzhi, 2018, Opt. Spectrosc. **125**, 439.
Volke-Sepulveda, K., V. Garcés-Chávez, S. Chávez-Cerda, J. Arlt, and K. Dholakia, 2002, J. Opt. B **4**, S82.
Volyar, A., M. Bretsko, Y. Akimova, and Y. Egorov, 2019, Appl. Opt. **58**, 5748.
Wan, K. K., 2006, *From Micro to Macro Quantum Systems: A Unified Formalism with Superselection Rules and Its Applications* (World Scientific, Singapore).
Wang, J., *et al.*, 2012, Nat. Photonics **6**, 488.
Wang, J. J., T. Wriedt, J. A. Lock, and L. Mädler, 2016, J. Quant. Spectrosc. Radiat. Transfer **184**, 218.
Wang, M., F. Tang, X. Pan, L. Yao, X. Wang, Y. Jing, J. Ma, G. Wang, and L. Mi, 2017, BBA Clin. **8**, 7.
Wannier, G. H., 1937, Phys. Rev. **52**, 191.
Wätzel, J., I. Barth, and J. Berakdar, 2017, J. Mod. Opt. **64**, 1088.
Wätzel, J., and J. Berakdar, 2016, Sci. Rep. **6**, 21475.
Wätzel, J., A. S. Moskalenko, and J. Berakdar, 2012, Opt. Express **20**, 27792.
Weber, E. R., R. K. Willardson, H. Liu, and F. Capasso, 1999, *Intersubband Transitions in Quantum Wells: Physics and Device Applications* (Academic Press, New York).
Weiner, J., and F. Nunes, 2017, *Light-Matter Interaction*, 2nd ed. (Oxford University Press, New York).
Weisbuch, C., M. Nishioka, A. Ishikawa, and Y. Arakawa, 1992, Phys. Rev. Lett. **69**, 3314.
Wertz, E., *et al.*, 2010, Nat. Phys. **6**, 860.
Whewell, W., 1836, Phil. Trans. R. Soc. London **126**, 289.
Wigger, D., V. Karakhanyan, C. Schneider, M. Kamp, S. Höfling, P. Machnikowski, T. Kuhn, and J. Kasprzak, 2020, Opt. Lett. **45**, 919.
Wolf, S. A., D. D. Awschalom, R. A. Buhrman, J. M. Daughton, S. von Molnár, M. L. Roukes, A. Y. Chtchelkanova, and D. M. Treger, 2001, Science **294**, 1488.
Woolley, R. G., 1971, Proc. R. Soc. A **321**, 557, https://www.jstor.org/stable/77814.
Woźniak, P., I. De Leon, K. Höflich, G. Leuchs, and P. Banzer, 2019, Optica **6**, 961.
Xie, Y.-Y., *et al.*, 2020, Nat. Nanotechnol. **15**, 125.
Yamamoto, Y., F. Tassone, and H. Cao, 2000, *Semiconductor Cavity Quantum Electrodynamics* (Springer Science+Business Media, New York).
Yang, K.-H., 1976, Ann. Phys. (N.Y.) **101**, 62.
Yang, S., W. Chen, R. L. Nelson, and Q. Zhan, 2009, Opt. Lett. **34**, 3047.
Ye, L., J. R. Rouxel, S. Asban, B. Roesner, and S. Mukamel, 2019, J. Chem. Theory Comput. **15**, 4180.
Yin, J., W. Gao, and Y. Zhu, 2003, Prog. Opt. **45**, 119.
Yin, L., V. K. Vlasko-Vlasov, A. Rydh, J. Pearson, U. Welp, S.-H. Chang, S. K. Gray, G. C. Schatz, D. B. Brown, and C. W. Kimball, 2004, Appl. Phys. Lett. **85**, 467.
Yu, L. W., K. J. Chen, J. Song, J. Xu, W. Li, X. F. Li, J. M. Wang, and X. F. Huang, 2007, Phys. Rev. Lett. **98**, 166102.
Zang, X., and M. T. Lusk, 2017, Phys. Rev. A **96**, 013819.
Zeng, S., Z. Tang, C. Liu, and P. Zhou, 2021, Nano Res. **14**, 1752.
Zhang, H., *et al.*, 2017, Nat. Commun. **8**, 16025.
Zhang, K., Y. Wang, Y. Yuan, and S. N. Burokur, 2020, Appl. Sci. **10**, 1015.
Zhang, K., Y. Yuan, D. Zhang, X. Ding, B. Ratni, S. N. Burokur, M. Lu, K. Tang, and Q. Wu, 2018, Opt. Express **26**, 1351.
Zhang, L., B. Shen, Z. Bu, X. Zhang, L. Ji, S. Huang, M. Xiriai, Z. Xu, C. Liu, and Z. Xu, 2021, Phys. Rev. Applied **16**, 014065.
Zhang, Z., H. Zhao, D. G. Pires, X. Qiao, Z. Gao, J. M. Jornet, S. Longhi, N. M. Litchinitser, and L. Feng, 2020, Light Sci. Appl. **9**, 179.
Zhang, Z., *et al.*, 2020, Science **368**, 760.
Zhao, Y., J. S. Edgar, G. D. Jeffries, D. McGloin, and D. T. Chiu, 2007, Phys. Rev. Lett. **99**, 073901.
Zhu, J., X. Cai, Y. Chen, and S. Yu, 2013, Opt. Lett. **38**, 1343.